2013

Determining the Mechanical Properties of Lattice Block Structures

Nathan Wilmoth
Cleveland State University

DETERMINING THE MECHANICAL PROPERTIES OF LATTICE BLOCK STRUCTURES

NATHAN WILMOTH

Bachelor of Science in Mechanical Engineering

The University of Akron

May 2010

submitted in partial fulfillment of requirements for the degree

MASTER OF SCIENCE IN MECHANICAL ENGINEERING

at the

CLEVELAND STATE UNIVERSITY

May 2013

This thesis has been approved
for the Department of Mechanical Engineering
and the College of Graduate Studies by

_____

Advisor/ Committee Chairperson, Stephen F. Duffy, PhD, PE, F. ASCE

_____

Department/Date

_____

Jerzy T. Sawicki, PhD, PE, F. ASME

_____

Department/Date

_____

Surendra Tewari, PhD

_____

Department/Date

ACKNOWLEDGEMENTS

I would first like to thank my advisor and committee chair, Dr. Stephen Duffy, for all of his insight and the immense amount of time spent editing this thesis. I would also like to thank my other committee members, Dr. Jerzy Sawicki and Dr. Surendra Tewari, for taking the time to be a part of this thesis.

I would like to extend my gratitude to the many engineers at the NASA Glenn Research Center for all of their input, ideas, and help to complete this thesis. More specifically, Dr. Mike Nathal for allowing me to join this project, Dr. Brad Lerch for his helpful revisions, and the shape memory alloy group for teaching me about shape memory alloys.

I also must thank the technicians and machinists who helped to put everything together for the testing. Without your help, I never would have been able to complete this project. Special thanks to Chris Burke for helping to setup the test frame and eliminate gremlins. In addition, I cannot go without thanking Joe Lavelle for working with me and expeditiously cutting and preparing specimens whenever I ran to the machine shop in a panic. Thanks also go to Tim Ubienski and Csongor Hollohazy for machining all of the fixtures required for this project.

Most importantly, I must thank my family for all of the moral support they have given me in over the years which has made me the person that I am today. I know I can be difficult, but your love have never wavered.

Lastly, thank you “mama” Joy for all of your encouragement and for being a sounding board for all of my disgruntled conversations…we did it!

DETERMINING THE MECHANICAL PROPERTIES OF LATTICE BLOCK STRUCTURES

NATHAN WILMOTH

ABSTRACT

Lattice block structures and shape memory alloys possess several traits ideal for solving intriguing new engineering problems in industries such as aerospace, military, and transportation. Recent testing at the NASA Glenn Research Center has investigated the material properties of lattice block structures cast from a conventional aerospace titanium alloy as well as lattice block structures cast from nickel-titanium shape memory alloy. The lattice block structures for both materials were sectioned into smaller subelements for tension and compression testing. The results from the cast conventional titanium material showed that the expected mechanical properties were maintained. The shape memory alloy material was found to be extremely brittle from the casting process and only compression testing was completed. Future shape memory alloy lattice block structures will utilize an adjusted material composition that will provide a better quality casting. The testing effort resulted in baseline mechanical property data from the conventional titanium material for comparison to shape memory alloy materials once suitable castings are available.

TABLE OF CONTENTS

Page

LIST OF TABLES X

LIST OF FIGURES XI

CHAPTER I: LATTICE BLOCK STRUCTURES 1

1.1 Introduction 1

1.2 Advantages, Challenges, and Definitions 4

1.3 Fabrication Methods 10

1.4 Previous Studies on Mechanical Strength 12

1.5 Objective 15

CHAPTER II: NICKEL-TITANIUM SHAPE MEMORY ALLOYS 17

2.1 Introduction 17

2.2 Phase Transformations 18

2.3 Bulk Mechanical Properties 26

CHAPTER III: TEST SPECIMENS, EQUIPMENT, AND PROTOCOLS 29

3.1 Introduction 29

3.2 Preparation of Specimens Obtained from the Facesheet 30

3.3 Preparation of Samples Obtained from the Internal Lattice 33

3.4 Test Fixtures 34

3.5 Test Frame and Heating Chamber 46

3.6 Extensometry 49

3.7 Mode Control 53

3.8 Test Standards 54

CHAPTER IV: BASELINE TESTING: Ti-6-4 55

4.1 Introduction 55

4.2 Ti-6-4 Tensile Testing 57

4.3 Ti-6-4 Compression Testing 72

4.4 Comparisons of Ti-6-4 Using Tension and Compression Data 82

4.5 Metallographic Evaluation of Ti-6-4 84

CHAPTER V: COMPARISION TESTING: NiTi SHAPE MEMORY ALLOY 87

5.1 Introduction 87

5.2 NiTi Tensile Tests 90

5.3 NiTi Compression Tests 90

5.4 Metallographic Evaluation of NiTi 102

CHAPTER VI: SUMMARY, DISCUSSION, AND CONCLUDING REMARKS 108

6.1 Summary 108

6.2 Remarks on Ti-6-4 Tension Testing 111

6.3 Ti-6-4 Compression Testing 117

6.4 Remarks on NiTi Tension Test 121

6.5 NiTi Compression Testing 123

6.6 Conclusions and Future Efforts 123

BIBLIOGRAPHY 125

APPENDIX A: EXTENDED DEFINITIONS 132

A.1 Hot Isostatic Pressing 132

A.2 Rapid Prototyping 132

A.3 Injection Molding 133

A.4 Hitchiner Counter Gravity Casting Method 133

A.5 Alumina 133

A.6 Scanning Electron Microscope 134

A.7 Auxetic Structure 134

APPENDIX B: FIXTURE DRAWINGS 135

B.1 Extensometer Step-Down Adapter 135

B.2 One Half of Clamshell Fixture for Transverse Specimens 136

B.3 Second Half of Clamshell Fixture for Transverse Specimens 136

B.4 Insert Restraint Fixture for Transverse Specimens 137

B.5 One Half of Clamshell Fixture for Vertical Specimens 137

B.6 Second Half of Clamshell Fixture for Vertical Specimens 138

B.7 Insert Restraint Fixture for Vertical Specimens 138

B.8 Clevis Fixture 139

B.9 Clevis Pull Rods 139

B.10 Compression Rods 140

APPENDIX C: DEFECT MAPS 141

C.1 Ti-6-4 Lattice Block Panel #1 Defect Map 141

C.2 Ti-6-4 Lattice Block Panel #2 Defect Map 142

C.3 Ti-6-4 Lattice Block Panel #3 Defect Map 142

C.4 Ti-6-4 Lattice Block Panel #4 Defect Map 143

APPENDIX D: EXTENDED DATA TABLES 144

D.1 Ti-6-4 Properties for Comparison 144

D.2 Ti-6-4 Tension Test data 145

D.3 Ti-6-4 Compression Test Data 147

D.4 NiTi Compression Test Data 148

LIST OF TABLES

Table **Page**

Table I: Ti-6-4 Lattice Block Structure Panel Designation 56

Table II: Ti-6-4 Strength Data 60

Table III: Ti-6-4 Deformation Properties 61

Table IV: Ti-6-4 Compression Average Test Results 74

Table V: Ti-6-4 Chemical Analysis Results 86

Table VI: NiTi Lattice Block Structure Panel Designation 88

Table VII: Averaged Mechanical Properties from NiTi Compression Tests 98

Table VIII: NiTi Chemical Analysis Results 107

Table IX: Ti-6-4 Material Properties for Comparison 144

Table X: Ti-6-4 VL Test Specimen Data 145

Table XI: Ti-6-4 VS Test Specimen Data 145

Table XII: Ti-6-4 TL Test Specimen Data 146

Table XIII: Ti-6-4 TS Test Specimen Data 146

Table XIV: Ti-6-4 Compression Test Specimen Data 147

Table XV: NiTi Compression Test Specimen Data 148

LIST OF FIGURES

Figure **Page**

Figure 1.1: Proposed loading conditions for LBS 2

Figure 1.2: Ti-6-4 Lattice Block Panel 5

Figure 1.3: Lattice Block Structure with Facesheets Removed 5

Figure 1.4: Hip Sink 7

Figure 1.5: Open Pore 8

Figure 1.6: Incomplete Casting Fill 8

Figure 1.7: Hot Tearing 8

Figure 1.8: Etched and polished cross-section of a strut 9

Figure 2.1: Stress, Strain, Temperature plot of a typical NiTi specimen 19

Figure 2.2: Transformation Temperatures of NiTi 21

Figure 2.3: Micrographs of Equiatomic NiTi 22

Figure 2.4: Illustration of the Shape Memory Effect on NiTi 23

Figure 2.5: Isobaric "training" of NiTi shape memory alloy 24

Figure 2.6: Aspects of pseudoelasticity in NiTi 25

Figure 3.1: Typical Marked Panel for Cutting of Facesheet Specimens 31

Figure 3.2: Specimen Geometries for Tensile Testing of Ti-6-4 33

Figure 3.3: Typical Compression Specimen 34

Figure 3.4: Tabbed Specimen with Cracked Epoxy 35

Figure 3.5: Crushed Potted Specimens 36

Figure 3.6: Epoxy Failures 36

Figure 3.7: Transverse Specimen "arm" 37

Figure 3.8: 3D Exploded Model of Transverse Specimen Fixture 37

Figure 3.9: von Mises Stress of Transverse Fixture 39

Figure 3.10: Rapid Prototype of Transverse Specimen Fixture 40

Figure 3.11: Machined and Heat Treated Transverse Specimen Fixture 40

Figure 3.12: Vertical Specimen “arm” 41

Figure 3.13: 3D Exploded Model of Vertical Specimen Fixture 41

Figure 3.14: von Mises Stress of Vertical Fixture 42

Figure 3.15: Rapid Prototype of Vertical Specimen Fixture 43

Figure 3.16: Machined and Heat Treated Vertical Specimen Fixture 43

Figure 3.17: Clevis-pin Assembly 45

Figure 3.18: Assembled Fixture with Specimen Mounted in Test Frame 45

Figure 3.19: Compression Testing Rods with Alumina Platens 46

Figure 3.20: 22kip Servohydraulic Test Frame 47

Figure 3.21: Hydraulic collet grip 47

Figure 3.22: Quartz Paneled Furnace 49

Figure 3.23: High Temperature Extensometer with Step-down Adapters 50

Figure 3.24: Computer with Stereo Cameras Mounted for Testing 51

Figure 3.25: Typical Calibration Panel 52

Figure 3.26: Typical Painted Tension Specimen 53

Figure 4.1: Axial Surface Strains for a Tensile Specimen Containing No Node 62

Figure 4.2: Axial Surface Strains for a Tensile Specimen with a Node 63

Figure 4.3: Stress-Strain Curves for Ti-6-4 Tensile Tests at Room Temp 64

Figure 4.4: Stress-Strain Curves for Ti-6-4 Tensile Tests at 165 °C 64

Figure 4.5: Stress-Strain Curves for Ti-6-4 Tensile Tests at 200 °C 65

Figure 4.6: Tensile Failure in the Gage Section 65

Figure 4.7: Tensile Failure at Surface Imperfection 66

Figure 4.8: Tensile Failure by Pullout in the Grip 66

Figure 4.9: Tensile Failure at a Node 66

Figure 4.10: Ti-6-4 Tensile Elastic Modulus 69

Figure 4.11: Ti-6-4 Tensile Yield Stress 69

Figure 4.12: Ti-6-4 Tensile Ultimate Strength 70

Figure 4.13: Ti-6-4 Tensile Poisson's Ratio 70

Figure 4.14: Ti-6-4 Tensile Percent Elongation 71

Figure 4.15: Ti-6-4 Tensile Percent Area Reduction 71

Figure 4.16: Axial Surface Strains for a Ti-6-4 Compression Specimen 76

Figure 4.17: Stress-Strain Curves for Ti-6-4 Compression Tests at Room Temp 77

Figure 4.18: Stress-Strain Curves for Ti-6-4 Compression Tests at 165 °C 78

Figure 4.19: Stress-Strain Curves for Ti-6-4 Compression Tests at 200 °C 78

Figure 4.20: Failure Modes of Ti-6-4 Compression Specimens 79

Figure 4.21: Ti-6-4 Compressive Elastic Modulus 80

Figure 4.22: Ti-6-4 Compressive Yield Stress 81

Figure 4.23: Ti-6-4 Compressive Poisson's Ratio 81

Figure 4.24: Comparison of the Elastic Modulus for Ti-6-4 82

Figure 4.25: Comparison of the Yield Stress for Ti-6-4 83

Figure 4.26: Comparison of the Poisson's Ratio for Ti-6-4 83

Figure 4.27: Ti-6-4 Etched Metallographic Specimens 85

Figure 4.28: Typical Microstructure of Cast Ti-6-4 Specimens 85

Figure 5.1: Typical NiTi Lattice Block Structure node cracks 89

Figure 5.2: Internal void and cracks at node 90

Figure 5.3: Generic NiTi Compression Stress-Strain Curve Below the Austenite Finish Temperature 92

Figure 5.4: Generic NiTi Compression Stress-Strain Curve Above the Austenite Finish Temperature 93

Figure 5.5: Axial Surface Strains for a Typical NiTi Compression Specimen 94

Figure 5.6: Stress-Strain Curves for NiTi Compression Tests at Room Temperature 95

Figure 5.7: Stress-Strain Curves for NiTi Compression Tests at 165 °C 96

Figure 5.8: Stress-Strain Curves for NiTi Compression Tests at 200 °C 96

Figure 5.9: Room Temperature Stress-Strain Curves for Current and Previous NASA NiTi Compression Tests 98

Figure 5.10: Failure Modes of NiTi Compression Specimens 99

Figure 5.11: NiTi Compressive Apparent Elastic Modulus 100

Figure 5.12: NiTi Compressive Apparent Reorientation Start Stress 100

Figure 5.13: NiTi Compressive Apparent Reorientation Finish Stress 101

Figure 5.14: NiTi Poisson's Ratio 101

Figure 5.15: Unetched Metallographic NiTi Specimens 103

Figure 5.16: Optical Image of Etched NiTi Node Specimen 104

Figure 5.17: Cross Section of Etched As-Extruded NiTi 104

Figure 5.18: Optical Image of Etched NiTi End Cross Sectional View 104

Figure 5.19: Optical Image of Etched NiTi Horizontal Cross Sectional View 105

Figure 5.20: SEM Image of a Typical NiTi Test Specimen 106

Figure 5.21: SEM Image of a Typical NiTi Test Specimen with a Crack at the Grain Boundary 106

Figure 6.1: Tensile Specimen with Machining Nick 113

Figure 6.2: Transverse and Vertical Specimens in Fixture 114

Figure 6.3: Transverse Specimen Before Final Trimming 114

Figure 6.4: Vertical Specimen Before Final Trimming 114

Figure 6.5: Vertical Specimen Ideal Load Condition 116

Figure 6.6: Vertical Specimen after “Pullout” Failure 116

Figure 6.7: Transverse Specimen Ideal and Actual Load Condition 116

Figure 6.8: Typical Surface Texturing of As-Cast Ti-6-4 Compression Specimens 118

Figure 6.9: Comparison of Axial Surface Strain for Well-Machined Tool Steel and As-Cast Ti-6-4 Specimens 120

Figure 6.10: NiTi Phase Diagram 122

Figure 6.11: Typical Surface Texture of As-Cast NiTi Compression Specimens 123

Figure B.1: Step-down Adapter to Reduce 0.5 inch Gage Length Extensometer to 0.25 inch Gage Length 135

Figure B.2: Transverse Specimen Fixture Half without Upper Threaded Holes 136

Figure B.3: Transverse Specimen Fixture Half with Upper Threaded Holes..... 136

Figure B.4: Fixture Insert for the Transverse Specimens..... 137

Figure B.5: Vertical Specimen Fixture Half without Upper Threaded Holes 137

Figure B.6: Vertical Specimen Fixture Half with Upper Threaded Holes..... 138

Figure B.7: Fixture Insert for the Vertical Specimens..... 138

Figure B.8: Clevis for Mounting the Clamshell Fixtures into the Test Frame 139

Figure B.9: Clevis Pull Rods 139

Figure B.10: Compression Rods 140

Figure C.1: Defect Map for Ti-6-4 Lattice Block Panel #1 141

Figure C.2: Defect Map for Ti-6-4 Lattice Block Panel #2 142

Figure C.3: Defect Map for Ti-6-4 Lattice Block Panel #3 142

Figure C.4: Defect Map for Ti-6-4 Lattice Block Panel #4 143

CHAPTER I

LATTICE BLOCK STRUCTURES- AN OVERVIEW

1.1 Introduction

Advanced materials will continue to play a strategic role in the national economy. The materials research community must look for ways to manufacture engineered products that are lighter, less expensive, more fuel efficient, and safer. Lattice block (i.e., open cell) structures and shape memory materials, the focus of this thesis, can and will contribute to these advantages. Creating a lattice block structure from a shape memory material introduces intriguing new engineering possibilities. Use of lattice block structures are finding their way into a host of aerospace, military, and transportation applications.

A lattice block structure can be fabricated in a variety of geometries and from any castable material. Components fabricated using a lattice block structure are very damage tolerant and impact resistant. Current technology allows these structures to be

cast with integral bolting flanges, feed-throughs, and other attachments (1). Lattice block structures can be used as cooling channels where coolant can flow with little restriction through the middle of a panel (2). In the aerospace industry, projected uses for lattice block structures include engine cases, shrouds, exhaust components, actuators, and as other structural components. This hybrid material system will find applications in transportation vehicles producing lighter weight vehicles with excellent crashworthiness properties due to the high energy absorption inherent to both lattice block structures and shape memory alloys. In general, load cases being considered for lattice block structures are shown in Figure 1.1.

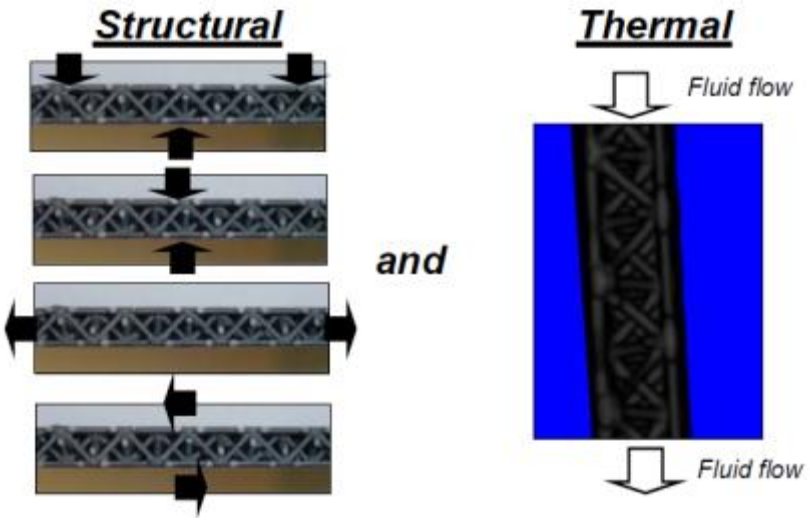

Figure 1.1: Proposed loading conditions for LBS (1)

There are a number of synergies obtained by utilizing shape memory alloys within a lattice block structure. In general, incorporating shape memory alloys in lattice block structures allows for innovative designs in aircraft structures (3) and other cutting edge technologies. By casting lattice block structures from shape memory alloys

structural components can return to their original geometry after incurring deformation. Lattice block structures fabricated from shape memory alloys can be designed such that heating or cooling causes a beneficial torsion, contraction, expansion, or any combination of deformations.

In this thesis shape memory alloys are discussed relative to lattice block structures. However, it must be pointed out that shape memory alloys are being used in a number of novel applications. For example, this material is being proposed for use in shape optimizing aircraft wing components. Research engineers at NASA are looking at replacing the flap motor assembly on an aircraft wing with a shape memory linear actuator rod. This arrangement would increase reliability while decreasing cost and weight by replacing several components (i.e., motor, gearbox, hydraulic lines) with fewer lighter weight components, some of which will be fabricated from a shape memory alloy. This aircraft wing application allows for a 41 to 1 weight reduction (4). A recent NASA application is on the Mars Pathfinder rover where a dust cover for a solar panel was operated by a shape memory actuator (5). An application for shape memory alloys used in rotorcraft utilizes a torque tube fabricated from a shape memory alloy to optimize performance by twisting the rotor blade about the shaft centerline. Twisting adjusts the blade pitch when hovering or during directional flight (5). Shape memory alloys have been proposed for use in damping and vibration control as well. Chen et al. (6) investigated using nickel-titanium (NiTi) shape memory alloy wires as a damper in structures to reduce structural forces during earthquakes. Chen et al. (6) demonstrate reductions in vibration amplitude of 89.5% and 38.8% for medium and large

earthquakes, respectively, on simulated structures. Another possible application for shape memory alloy is applying NiTi wires to space structures for vibration damping (7).

1.2 Advantages, Challenges, and Definitions

Lattice block structures are light weight and provide cost effective alternatives to solid cast metal alloys as well as some composite structures. The primary purpose of this thesis is reporting strength data for subcomponents of lattice block structures. To facilitate this, several common lattice block structure terms and definitions are introduced here. Figure 1.2 shows a 3.75 inch x 3.75 inch x 1 inch (95.25 mm x 95.25 mm x 25.4 mm) lattice block with an open facesheet design typical of the material tested in this effort, with labeling to indicate the location of some key features. A lattice block is usually comprised of two facesheets. A *facesheet* serves as an impact or loading surface, and/or a fascia that encloses the internal structure. The facesheet may be solid, or open, but can be of any design that can be incorporated into a casting mold. Between the facesheets are the internal structural supports of the lattice block defined here as *struts,* which are oriented in different directions. Figure 1.3 is the same panel depicted in Figure 1.2 but with the facesheets removed to better show the internal structure of the lattice block panel. The struts are connected internally at points called *nodes,* and these nodes act to join the internal structure to the facesheets.

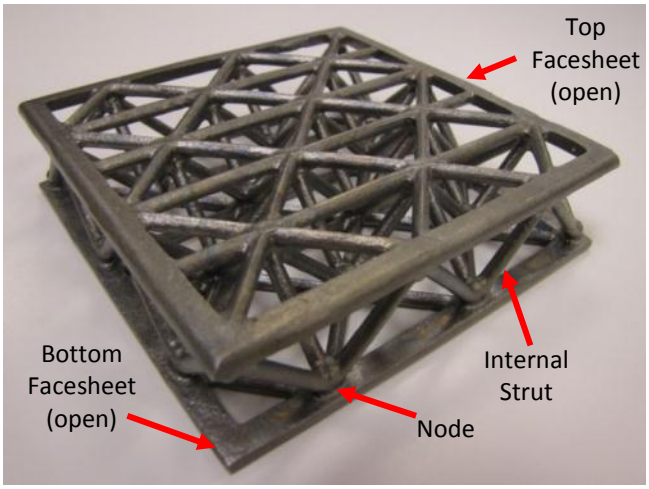

Figure 1.2: Ti-6-4 Lattice Block Panel

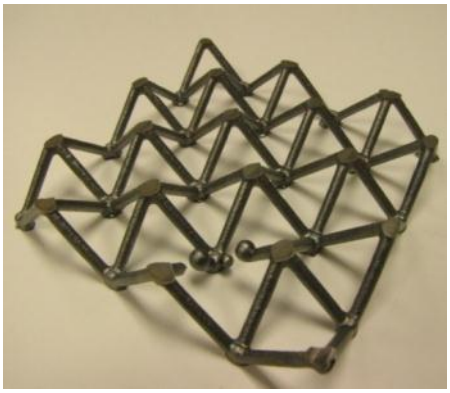

Figure 1.3: Lattice Block Structure with Facesheets Removed

Depending on the use of the lattice block structures, the lattice structure can be optimized relative to size and geometry to accommodate applied loads or other boundary conditions. Optimizing the open truss structure adds strength and stiffness to the assembly while minimizing weight. For example, the geometry of the lattice block structure in this study contains only 13% material by weight compared to a similar solid structure with the same overall dimensions. The weight comparison is made using the

density of commercial Ti-6Al-4V (8) and the weight and dimensions of the lattice block structure in Figure 1.2.

The internal construction of the lattice block structure is designed with multiple load paths. This helps in redistributing load in the event of a single strut failure (9). The ability to redistribute load from a failed strut to others in the near vicinity of the failed strut provides considerable internal redundancy. The result is a very damage and defect tolerant structural panel. It has been shown that by randomly removing 10% of ligaments within a lattice block structure results in a stiffness, yield, and ultimate strength decrease of at most 20% for each. Contrast this with an aluminum honeycomb sandwich panel which experiences a decrease in strength of 65% with a comparable amount of material removed (10). The versatility of lattice block structures is further demonstrated by the fact that they can be directly cast into complex shapes like curves or twists, limited only by the casting mold and materials (10).

Not only are lattice block structures designed to be lightweight with high strength and stiffness (11), but they are also suitable for use at high service temperatures depending on the cast material used. Lattice block structures fabricated from aluminum alloys are acceptable for service temperatures below 200 °F (93 °C), whereas lattice block structures fabricated from conventional titanium alloys give satisfactory results up to 1000 °F (538 °C). Temperature requirements above 1000 °F necessitate the use of superalloys (1). The lattice block panels can also function as thermal sinks when cooling channels are integrated, as conduit for piping and wiring, or insulation can be added for sound or thermal management (10).

While there are many advantages to lattice block structures, there are notable disadvantages. Because the panels are complex cast products, they are prone to manufacturing defects. Manufacturers have recently improved fabrication processes, but four defects remain common. The first defect is referred to as a "sink" (Figure 1.4), which is the result of internal pores closing during hot isostatic pressing.[1] Second, open pores (Figure 1.5) in the material are the result of surface bubbles on the casting that the hot isostatic pressing treatment cannot close. Another defect is an unfilled mold area which is identified in Figure 1.6. Hot tearing (Figure 1.7), occurs when the material is overstressed during cooling in the casting and leads to cracks.

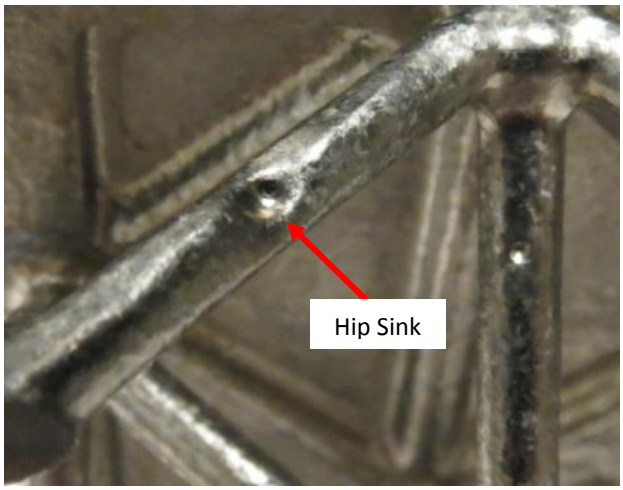

Figure 1.4: Hip Sink

[1] See Appendix A.1 for more information on Hot Isostatic Pressing

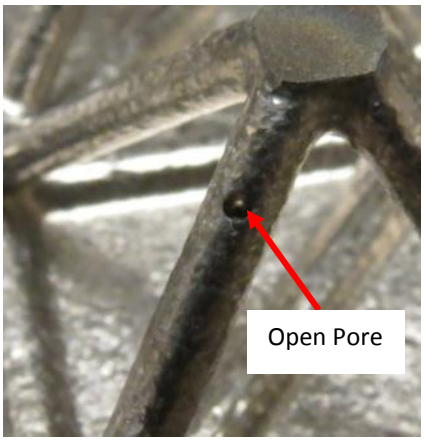

Figure 1.5: Open Pore

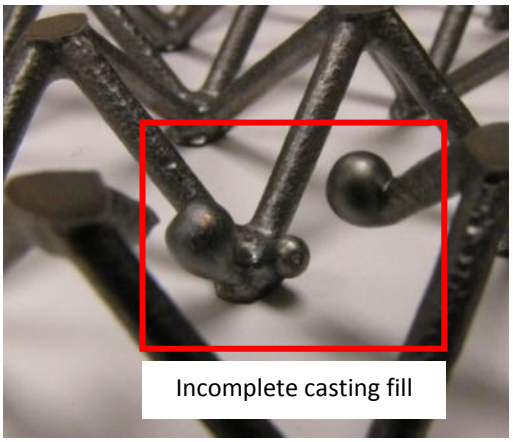

Figure 1.6: Incomplete Casting Fill

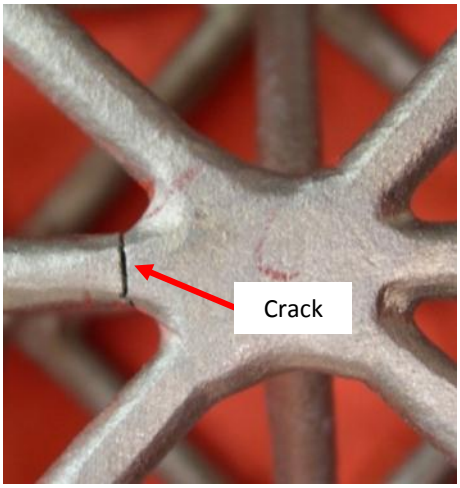

Figure 1.7: Hot Tearing

These defects are macro-level defects that can be identified through visual examination. Even if a lattice block panel is visually free of defects, micro-level porosity defects due to shrinkage can be present (10). Identifying these defects requires either destructive metallographic analysis (Figure 1.8) or non-destructive evaluation methods. Non-destructive evaluation techniques are especially difficult to perform on lattice block structures because of the complex nature of the panel geometry. Having facesheets on either side of the panel and inner structural struts oriented in three dimensions does not permit conventional non-destructive evaluation methods to "look" for defects with satisfactory results. The best results have been obtained by employing a combination of X-ray (1), pulse echo ultrasound (1), and thermal imaging techniques (12).

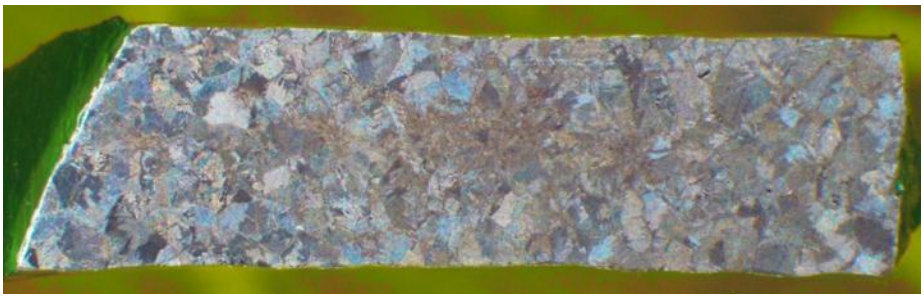

Figure 1.8: Etched and polished cross-section of a strut

A study by Ott (1) in conjunction with the NASA Glenn Research Center and General Electric's Aviation Division looked into the feasibility of producing investment cast lattice block structures from superalloys for gas turbine engine applications. Ott's (1) work found that several casting defects were present and limitations in the use of current non-destructive evaluation techniques relative to lattice block structures were noted.

1.3 Fabrication Methods

Lattice block structures can be fabricated from wire (13) and sheet material (1), or the lattice block can be fabricated using investment casting. Investment casting was the method used for the panels tested here. Investment casting uses expendable patterns made from wax or low melting temperature plastic. Manufacturing casting patterns are achieved using rapid prototyping[2] or injection molding.[3] Once the pattern has been manufactured, the wax or plastic is "invested" by dipping the assembly in a thick slurry. For low temperature investment casting, a mixture of plaster of Paris and powdered silica can be used as the investment slurry (8). High melting temperature materials require the use of a ceramic slurry (14). If multiple parts are being cast, all of the individual castings can be attached to a "tree" (8) so they can be slurry dipped as an assembly instead of individually. The tree, also called a cluster assembly, can contain anywhere from a few dozen parts to upwards of several hundred individual pieces (15). The wax or plastic patterns on the assembly are dipped in the slurry of particles until a sufficiently thick shell has formed. A baking process discussed next, hardens the shell and removes all of the wax or plastic pattern from the shell.

Ensuring that the shell is properly and fully cured has a significant impact on the quality of the part. When the mold is heated to liquefy the pattern, the pattern material will rapidly expand and will tend to cause high internal stresses in the mold leading to failure. To avoid a mold failure, the outside of the mold is quickly heated so the surface

[2] See Appendix A.2 for more information on rapid prototyping.
[3] See Appendix A.3 for more information on injection molding.

layer of the pattern material will liquefy and run out of the mold. This allows the remaining pattern material to expand as the temperature of the mold assembly equilibrates (15). Once the pattern material has been evacuated, the mold assembly is filled with an inert gas. This is done in a vacuum chamber or in a centrifuge if the casting material does not flow readily (8). The mold is then filled with molten material. Once the casting has solidified, the investment material can be removed in a number of ways depending on the complexity of the part. For simple parts, breaking off the investment material with pneumatic or hand tools and abrasive blasting produce satisfactory results. For complex castings, a combination of pneumatic and hand tools, water and abrasive blasting, cutoff wheels, band saws, and chemical bathing are employed to achieve complete removal of the investment material (15). The lattice block panels contained in this thesis were removed from their molds by either abrasive blasting or chemical milling. Once the mold material is removed, the cast part is then subjected to hot isostatic pressing (HIP) to reduce porosity.

The process used to fabricate the lattice block structures have evolved in recent years from the point where panels frequently contained several visual defects and voids to where they are now relatively defect free castings. With a consistent casting process, lattice block structures are simple and cost effective to manufacture. As a general rule of thumb, investment casting is an efficient method for manufacturing parts ranging from an ounce (28.3 g) (8) to 250 lbf (113.4 kg) (16). In contrast, aluminum honeycomb sandwich panels with weights similar to lattice block structure panels are significantly more complicated to manufacture.

1.4 Previous Studies on Mechanical Strength

As noted at the onset of this chapter, recent studies have investigated possible uses of lattice block structures. These same reports have also focused on better understanding and optimizing their thermo-mechanical properties. Some studies have focused on modeling of the structures, and more recent efforts have begun to blend experimental testing data with proposed analytical models. Reliable and accurate models that predict the mechanical properties of lattice block structures would tend to minimize costly laboratory testing if the constituent properties of a lattice block structure are known. Overall, there has been an incremental but steady evolution in the design of lattice block structures. The following paragraphs will give a brief background of relevant studies that predict and/ or report the mechanical properties of lattice block structures.

Past efforts that have focused on the design of lattice block structures will be reviewed first. Evans (17) published an overview on different designs of lattice block structures. A fundamental finding from this study was that a lattice block structure will exhibit failure at the nodes if the lattice is fabricated from a material with less than 20% ductility. The study indicated that designs can accommodate significant material defects with little reduction in theoretical load carrying capability of the panel. This is a direct result of the lattice block structure's ability to redistribute load to non-failed subcomponents. The Evans (17) research also noted that there is a strong correlation to structural performance and the design of the nodes. If a "gap" design is utilized where

the centerlines of the internal struts intersect in the middle of the facesheet, then the panel performs in a manner comparable to theory. If a design requires that the strut intersection is on the inside of the facesheet, then failure most commonly takes place by shearing at the nodes. Evans et al. (18) investigated the attributes of foam core, honeycomb core, and truss core structures. Their investigation found that the metal truss core structures, a type of lattice block, are efficient for secondary heat transfer uses. The study also found that the open structures are comparable in bending and superior in edge-loaded strength when compared to sandwich and honeycomb panels. A final conclusion from the study was that open cell structures can be optimized by adding material at critical locations depending on how the structure is loaded.

A study by Hebsur (19) investigated the aspects of fabricating lattice block structures from Inconel® 718 superalloy. This lattice block structure was the first attempt to use cast nickel based superalloy with a goal of producing lightweight nozzles for aircraft engines. The study concluded that good quality panels can be made from Inconel® 718 when high strength, low thermal expansion wax is used for the lost-wax pattern fabrication. In addition, the study indicated that good results were obtained from investment castings using a method referred to as the Hitchiner counter gravity casting method.[4] Sypeck et al. (20) focused on the comparison of open truss lattice block structures with aluminum honeycomb composite sandwich panels. The study found that the lattice blocks performed very well in compression and shear in comparison to aluminum honeycomb panels. Sypeck et al. (20) noted that the lattice

[4] See Appendix A.4 for more information on the Hitchiner counter gravity casting method

block structures can be fabricated into complex curved structures, whereas aluminum sandwich panels cannot.

A study by Nathal et al. (10) reported on the mechanical properties of Inconel® 718 and Mar-M-247® investment cast superalloy lattice block structures. Specifically, this study used lattice block structures produced by JAMCORP Incorporated (Billerica, Massachusetts) and detailed the material properties obtained from various specimen orientations conducted in tension and bending. Tensile tests conducted in this study showed significantly lower ductility in the lattice block structure test specimens compared to commercially available data on cast and heat treated alloys. This is most likely due to material defects in the specimens obtained from the lattice block structures. Strength values aligned well with published values for the bulk material. Bend tests conducted on sections of lattice block structures showed considerable load carrying capacity in the presence of a significant number of failed internal struts.

Wallach and Gibson (9) investigated the load carrying capacity of lattice block structures when random ligaments were removed. Test specimens with randomly removed ligaments were compared with an open cell foam structure where a similar amount of ligaments were removed. The study found that the stiffness of lattice block structures decreased linearly as ligaments are removed, while the stiffness of open cell foam structures decreased almost exponentially as additional material is removed. The linear nature of the strength degradation of the truss structure indicated that lattice block structures are more defect tolerant.

Reports on lattice block structures fabricated from a series of titanium alloys are available. A study by Li et al. (21) provides mechanical properties of lattice block structures fabricated from titanium (Ti-6Al-4V) using investment casting. Their study conducted tests on individual panel struts in tension and compression, conducted full panel compression and impact tests, and three point bend tests on partial panels. Tests were conducted on panels with two strut diameters, i.e., 0.126 inch and 0.063 inch (3.2 mm and 1.6 mm). Li et al. (21) found that the castings had defects but that the tension and compression properties of the castings aligned very well with published data.

1.5 Objective

The objective of this project was the investigation of the mechanical properties of the structural subcomponents of lattice block structures fabricated from NiTi shape memory alloys. The intent was to compare the mechanical properties determined for this constituent material system to baseline data for lattice block structures fabricated from Ti-6Al-4V. Testing of structural subelement properties for lattice block structures fabricated from shape memory alloys has not been reported on in the open literature. However, complications in the fabrication of the shape memory alloy material processing for the panels tested in this project lead to extremely brittle test specimens. Because of this, only a partial test matrix could be completed on the shape memory

alloy specimens. The data that was acquired, as well as the fabrication complications, are discussed in later chapters.

This thesis was supported by the "Three Dimensional Cellular Structures Enhanced by Shape Memory Alloys" program. All the testing that produced the data reported on here was conducted at facilities located at the NASA Glenn Research at Lewis Field (Cleveland, Ohio). The materials tested under this study were provided under a federal SBIR (Small Business Innovation Research) contract awarded to Transition 45 Incorporated (Orange, California). The lattice block structures described throughout are cast specimens either of commercially available Ti-6Al-4V (Ti-6-4) or of equiatomic nickel-titanium shape memory alloy (NiTi).

In review, Chapter 1 gives the reader the necessary background information to understand what a lattice block structure is and some previous work completed on this type of structure. Looking forward, Chapter 2 will discuss nickel-titanium shape memory alloys. Chapter 3 will focus on the process of readying specimens, fixtures, and equipment for testing. Chapter 4 will provide strength data for Ti-6-4 testing. Chapter 5 provides strength data from NiTi shape memory alloy testing. Chapter 6 provides a technical discussion explaining the data observed with concluding remarks.

CHAPTER II

NICKEL-TITANIUM SHAPE MEMORY ALLOYS

2.1 Introduction

The shape memory effect exhibited by NiTi was first observed in the early 1960's at the U.S. Naval Ordinance Laboratory and the material has been comprehensively studied since. NiTi is popular because of its biocompatibility, corrosion resistance, and the fact that it can be readily fabricated into thin wire, sheets, and tubes (22). This chapter begins by describing the characteristics of NiTi. The chapter then reviews earlier studies on NiTi and transitions to more recent ones to document the development of NiTi. Many studies have focused on equiatomic NiTi, which is the material composition used here. The descriptor equiatomic signifies that the material composition contains an equal atomic weight percent of nickel and titanium.

2.2 Phase Transformations

Shape memory alloys, in general, are materials that have the unique ability to return to their original shape after incurring what appears to be nonlinear plastic deformation. A thermal or mechanical load application is used to restore a component made from shape memory alloy from its deformed configuration back to the original geometry. The ability of shape memory alloys to recover to their original geometry enables the material to perform mechanical work during the recovery process. For example, a shape memory alloy wire can be connected to a small hanging weight. The tensile load of the weight will cause the wire to stretch, but when heat is applied to the wire the shape memory alloy will contract toward its original geometry and lift the weight some distance. This is a simplistic example and will only occur if the wire is properly conditioned and sized for the weight. However, the example illustrates that work can be extracted from a shape memory alloy material. Similarly, if a test specimen fabricated from a shape memory alloy is compressed, heating will cause the specimen to expand as a result of both the phase transformation and thermal expansion.

From a thermodynamic standpoint, shape memory alloys possess two equilibrium phase states: austenitic and martensitic. The austenitic phase is considered the high temperature “parent” phase where the material is in its base physical geometry. When the material is in the martensitic phase it is considered either twinned or detwinned. The martensitic phase is the material low temperature state. Reducing to the martensitic phase involves atomic shear deformation of the microstructure from

the parent austenitic phase (23). An idealized illustration depicting the stress-strain-temperature relation of a shape memory alloy is shown as path A→B→C→D→E→F in Figure 2.1 (5). The graph represents a nickel-titanium material beginning in the austenitic phase (point A in the graph) under no load and cooled to the twinned martensitic phase (point B). Stress was then applied under constant temperature to detwin the material (point C). The deformed specimen was unloaded (point D) leaving behind a residual strain from the detwinned martensitic phase. With no load applied, the material was heated through the detwinned martensitic phase (point E), recovering all detwinned deformation in the specimen and returning to its original stress-strain state (point F).

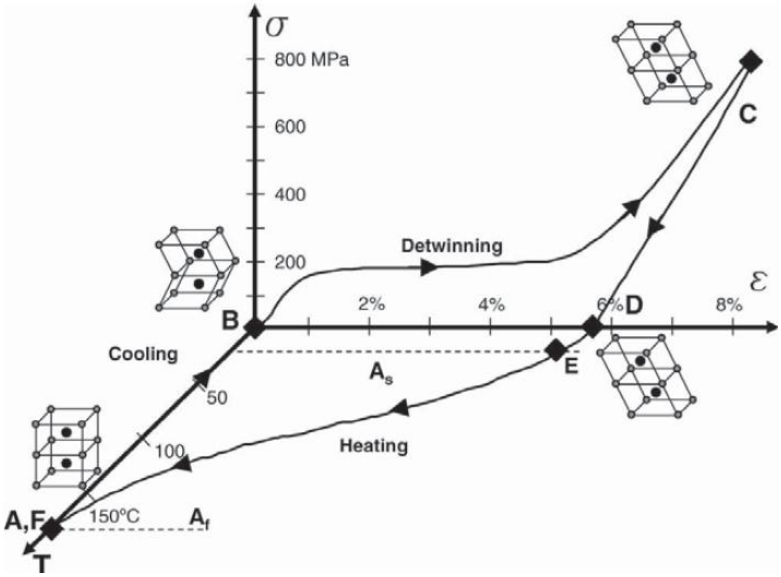

Figure 2.1: Stress, Strain, Temperature plot of a typical NiTi specimen (5)

As the graph in Figure 2.1 indicates, shape memory alloys will enter the twinned martensitic phase under isobaric conditions (constant stress with a decrease in

temperature), and the detwinned phase under isothermal conditions (constant temperature with an increase in stress). Once a shape memory material is transformed into the detwinned martensitic phase, it is semi-permanently deformed and will not return to its original shape until it goes through a heat cycle (5).

There are four important temperatures for shape memory alloys, i.e., the austenitic start and finish temperatures, as well as the martensitic start and finish temperatures. Figure 2.2 is a strain-temperature diagram showing these four transformation temperatures for a nickel-titanium test specimen. The curve shown in the figure is valid for one stress level only and the strain-temperature path of interest is identified as A → M_s → M_f → B → A_s → A_f → A. Note that different stress values will produce a different strain-temperature curve. The values of the start and finish temperatures are individually stipulated with a range since they depend on material composition. The austenitic start (finish) temperature denotes the temperature at which the transformation from martensite to austenite begins (finishes) as the material is heated (24). These temperatures are shown as points A_s (austenite start) and A_f (austenite finish) in Figure 2.2. The martensitic start (finish) temperature denotes the temperatures at which the transformation from austenite to martensite begins (finishes) as the material is cooled (24). These temperatures are shown as points M_s (martensite start) and M_f (martensite finish) in Figure 2.2. The finish temperature of the austenitic phase will always be higher than the finish temperature of the martensitic phase of the material. Transformation temperatures vary greatly depending on the material composition and typically range from -9.4 °F (-23 °C) for the martensitic finish

temperatures to above 441 °F (227 °C) for the austenitic finish temperature (22). When a shape memory material is deformed at some temperature below the austenitic start temperature, it will deform in a nonlinear fashion. This can be recovered under zero stress conditions by increasing the temperature of the material above the austenitic finish temperature. With the material in its original geometry, the process of cooling and stressing the structure can be repeated.

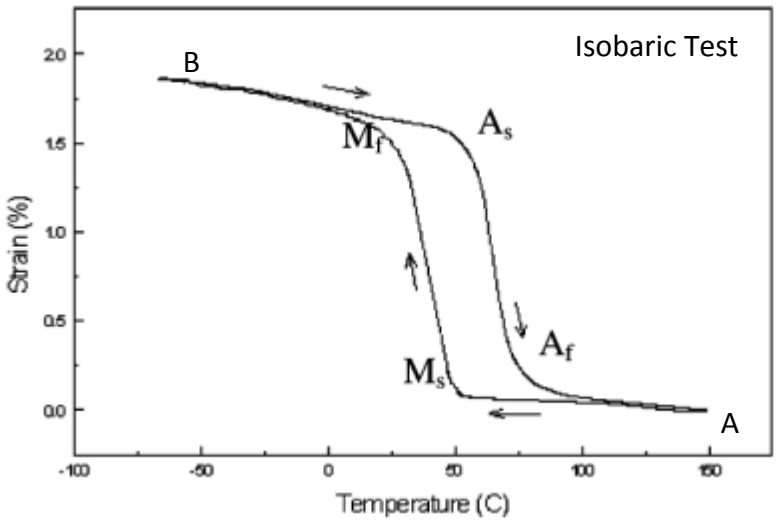

Figure 2.2: Transformation Temperatures of NiTi (25)

Figure 2.3 shows a transmission electron microscopy micrograph of a room temperature twinned martensite phase of equiatomic nickel-titanium on the left, and the same location on the specimen at 329 °F (165 °C) and 446 °F (230 °C) in the middle and right images, respectively.[5] As the specimen is heated under no load, the twinned martensite phase begins to disappear and has completely disappeared before the austenite finish temperature of approximately 105 °C.

[5] Images courtesy of Anita Garg, NASA GRC

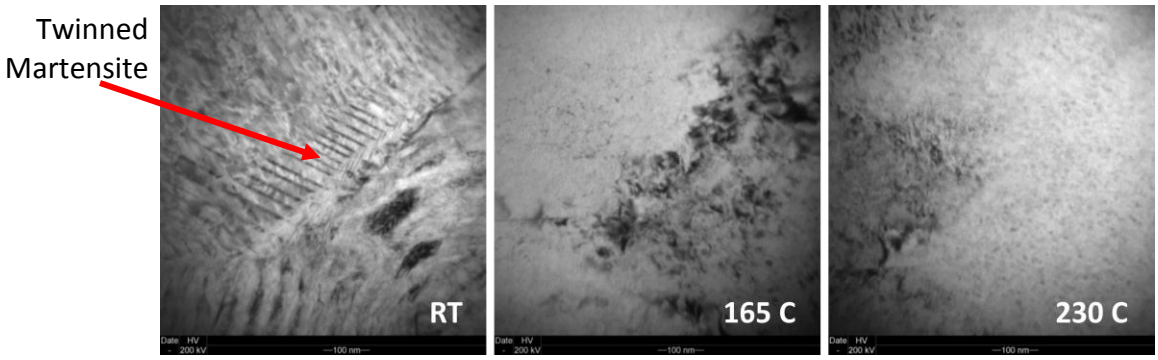

Figure 2.3: Micrographs of Equiatomic NiTi at room temperature (RT), 165° C, and 230° C (26)

The shape memory effect described above permits the extraction of work. This concept is shown in Figure 2.4 (5) where a strain-temperature plane from Figure 2.1 is obtained by stipulating a constant value for stress. Consider the cases where a constant stress is applied at 75 °C (point A) and the material is then cooled into the detwinned martensitic phase (point B). Subsequently, the material is then heated back into the austenitic phase (point C). The difference in the peak strain and the final strain is denoted $\Delta\varepsilon^{act}$ and this change in strain at constant stress provides work. Note that a small residual strain is accrued over this transformation cycle. Some of the residual strain can be recovered.

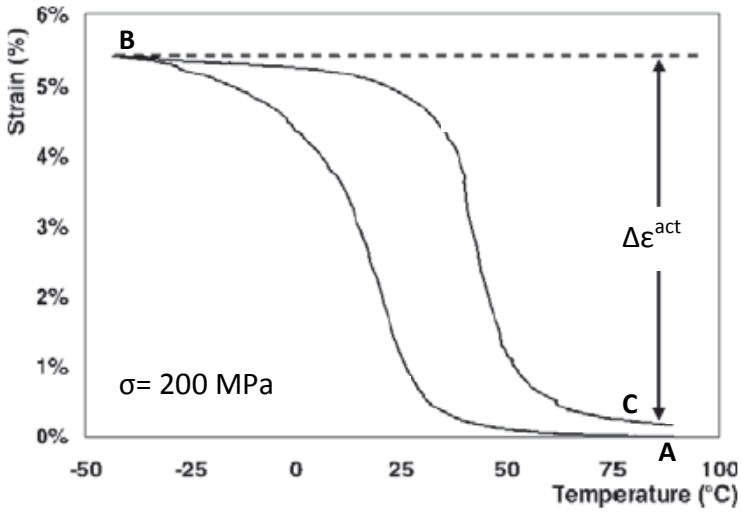

Figure 2.4: Illustration of the Shape Memory Effect on NiTi (5)

For cyclic transformation applications, the non-recoverable plastic strain can be removed, or reduced, by "training" the material. Training of the material can be accomplished through several methods. The two most common are cycling the material isothermally or isobarically for a sufficient number of cycles such that a stable hysteresis loop is obtained. This allows the material to recover with no applied stress and is referred to as the "two-way" shape memory effect (5) in the literature. The two-way shape memory effect is illustrated in Figure 2.5. The hysteresis lines show the material shifting to a stable response under isobaric conditions.

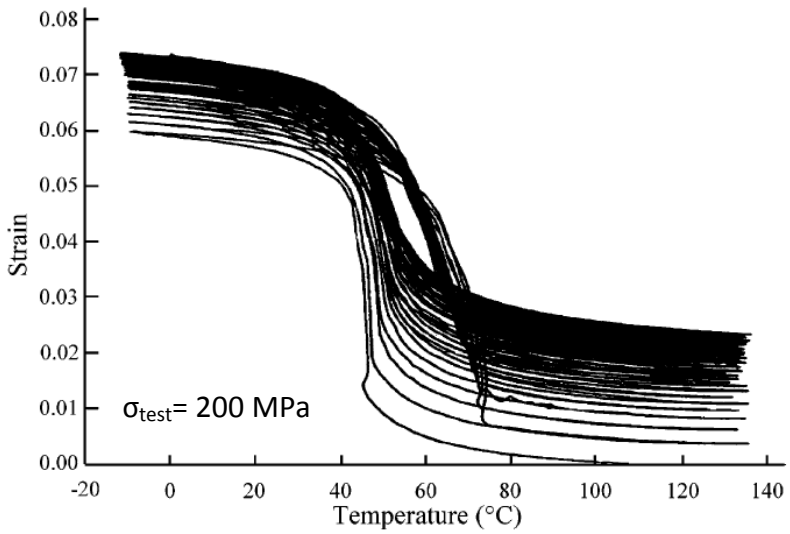

Figure 2.5: Isobaric "training" of NiTi shape memory alloy (22)

Another characteristic of shape memory materials is the pseudoelastic effect. With pseudoelasticity, stress instead of temperature causes the material microstructure to reorient itself. This characteristic is termed “stress induced martensite”. Stress is applied to the material causing the austenite to the martensite phase transformation. Upon unloading, the martensite returns to the austenite phase (5). Figure 2.6 shows the pseudoelastic response of a nickel-titanium shape memory alloy under isothermal conditions (5). The plot demonstrates an elastic response from points 1 to 2, with point 1 being in the parent austenitic phase and point 2 being the start of the martensitic phase transformation. From point 2 to point 3, the martensitic phase forms and at point 3 the material is in a fully martensitic state. Continued loading from point 3 results in an elastic response in a martensite phase with a different Young’s modulus than the initial elastic response of the austenite phase. When the load is removed, the material will

transform back into the austenitic phase along the load path between points 4 and 5. Note that point 5 is not necessarily below point 2 in all situations. When unloaded to zero stress, all of the elastic strain (ε^{el}- see horizontal axis in Figure 2.6) and strain from the material transforming from martensitic back to austenitic (ε^{trans}- see horizontal axis in Figure 2.6) will be recovered. Any non-recovered permanent deformation, i.e., plastic deformation, is designated as ε^{pl} in Figure 2.6. A hysteresis loop is obtained and the area inside the loop is equal to the energy dissipated (6).

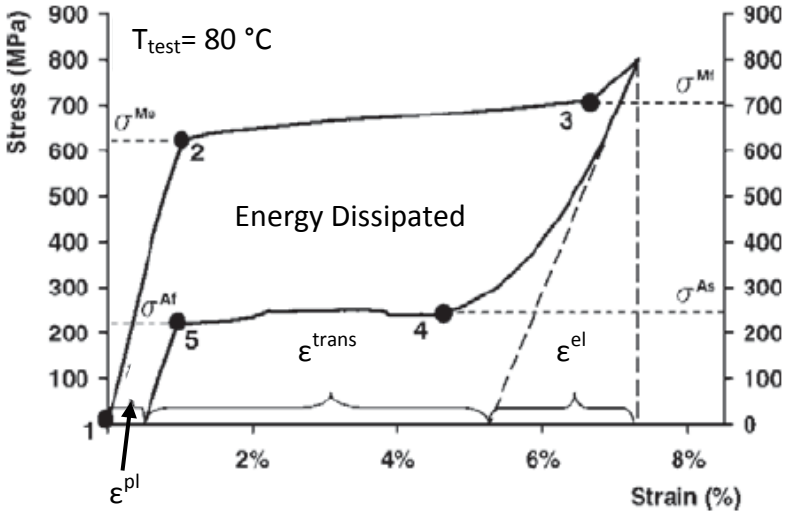

Figure 2.6: Aspects of pseudoelasticity in NiTi (5)

In summary, shape memory alloys present several interesting deformation behaviors that can be utilized in high-end engineering applications. A few of these behavioral aspects were presented above. The unique behavior of this material along with its use in the lattice framework of lattice block structures provides sufficient motivation to develop a database of mechanical properties for this material. A review

of property data for equiatomic NiTi available in the open literature is provided in the next section.

2.3 Bulk Mechanical Properties

The transformation temperatures of NiTi are highly dependent on processing and the metallurgy, which can be adjusted with different concentrations of alloy materials (27). For example, adding a higher concentration of nickel will decrease transformation temperatures while a titanium rich concentration will increase the transformation temperature (28). Published literature from Patoor et al. (22) has shown that martensitic finish temperatures (M_f) can be in the range of 60 ± 104 °F (15 ± 40 °C) while austenitic finish temperatures (A_f) can range from 192 ± 176 °F (89 ± 80 °C).

Fatigue data for shape memory alloys show cyclic lives of 10^5 cycles at 2% strain and 10^7 cycles at 0.5% strain (23). However, the maximum number of cycles to failure can vary greatly depending on the service temperature, stress and strain, and the material heat treatment process. In addition, shape memory alloys have a limited actuation frequency of approximately 30Hz. This frequency limitation is a function of the maximum heating and cooling rate of the material (5).

Funakubo (23) gives a brief but clear overview of the findings relating how temperature affects the stress-strain curves of equiatomic NiTi. In this study, tensile tests were conducted over the temperature range of -321 °F to 1292 °F (-196 °C to 700

°C). The data indicates that below 158 °F (70 °C) discontinuous yielding along with high strain hardening occurs in the 4%-7% strain range. In the 212 °F to 752 °F (100 °C to 400 °C) range the data shows that work hardening decreased and continuous yielding occurs. In the temperature regime above 752 °F (400 °C) large elongations occur with very minimal work hardening. These results indicate that the minimum yield strength of the material occurs near room temperature.

A study by Buehler and Wang (29) noted that equiatomic NiTi was ductile, demonstrated good damping qualities, and possessed above average fatigue properties. They found that the martensitic phase existed below the start of the austenitic phase, as shown previously in Figure 2.2, and that atomic shearing of the material occurred in the martensite region. Heating above the austenitic transformation temperature returned the material to its original geometry. The Buehler and Wang (29) study also reported dramatic changes in the damping properties based on the use temperature of the material. Studying the transition temperatures of various shape memory alloys, Buehler and Wang (29) found that the transition temperatures can vary from -396 °F to 331 °F (-238 °C to 166 °C) based on material compositions. Buehler and Wang (29) also reported on aspects of the production of NiTi. They found that NiTi can be produced by both arc and induction melting. Their study noted that the material could be readily hot or cold worked and the material was easily spot welded or brazed. However, machining was found to be difficult, requiring carbide tools used at slow speeds with light feeds.

A study published by Jackson et al. (30) focused on the chemical, mechanical, metallurgy, physical, and processing properties of NiTi. The study evaluated previous

work on equiatomic shape memory alloys to determine equilibrium phase diagrams and the corresponding crystal structure. Jackson et al. (30) found large discrepancies in the crystal structure among published papers and concluded that poor material characterization and labeling of the exact shape memory alloy composition used in previous studies were the likely cause of inconsistencies. Jackson et al. (30) were not able to determine the equilibrium structure of equiatomic NiTi with the available data. Recommendations in their report included further fatigue and impact testing above the transition temperature as well as determining if material properties degrade with time, i.e., does the material "damage."

A discussion of the testing and protocols is presented in the next chapter. In addition, temperature dependent mechanical data obtained from tests conducted on samples taken from lattice block structures fabricated from Ti-6-4 (the baseline material) is presented in Chapter 4. The thesis returns to the topic of equiatomic NiTi material in Chapter 5 where the results from testing of structural subelements taken from lattice block structures are presented.

CHAPTER III

TEST SPECIMENS, EQUIPMENT, AND PROTOCOLS

3.1 Introduction

Novel material systems require novel test protocols in order to develop an appropriate database of engineering design properties. These protocols include specimen design, test fixtures, and analysis of the data obtained. The strength testing effort reported on here uses three basic specimen geometries, i.e., ligaments, legs, and struts. Conceptually one should be able to evaluate the strength of a lattice block facesheet (Figure 1.2) by testing ligaments and legs. *Ligaments* are defined as a subelement that does not contain a node in the gage section, but does contain a node at each end. *Legs* are comprised of two ligaments with a centrally located node in the gage section. Specimens removed from the internal lattice (not the facesheet) will be defined as struts. Tension tests were completed on specimens removed from the facesheet while compression tests were completed on specimens removed from the

internal lattice block structure. The compressive strength is the critical design parameter for the internal lattice portion of the structure. Bend tests were not conducted as part of this test program. The preparation of test specimens used to characterize strength from these various structural subelements is described in detail later in this chapter. In addition, the components that comprise the test system are thoroughly discussed. Finally, the test protocols adopted for this work are presented.

3.2 Preparation of Specimens Obtained from the Facesheet

Unlike common mechanical testing where the goal is nearly pristine specimens obtained by machining, the specimens for this project are tested as-cast. A conscious effort was made to obtain test specimens free of visual defects. After samples were obtained from the facesheets, irregularities inherent to the specimens were left in place. However, extracting tensile test specimens from the facesheet of a lattice block structure proved problematic. It was not a surprise that cutting the facesheet using hand held cut-off wheels, high/low speed diamond wheels, and/ or a hacksaw yielded poor quality specimens. Specimens were frequently nicked and damaged in the gage section using these methods. In addition, this type of extraction introduced local regions of high temperature in the Ti-6-4 specimens because of a lack of coolant during cutting. Since shape memory alloys (NiTi) are very temperature sensitive, this extraction method would lead to the formation of residual stresses. As a result of these

difficulties, a two-step process for cutting of ligaments and legs from the facesheet was developed with shape memory alloys in mind. First, the lattice block structures being tested had both of the open facesheets removed by electrical discharge machining (EDM). Subelement tensile test specimens were marked and labeled on each facesheet (Figure 3.1). The specimens were subsequently cut from the facesheet using EDM because of its precision and because very little heat is transferred into the specimen during cutting.

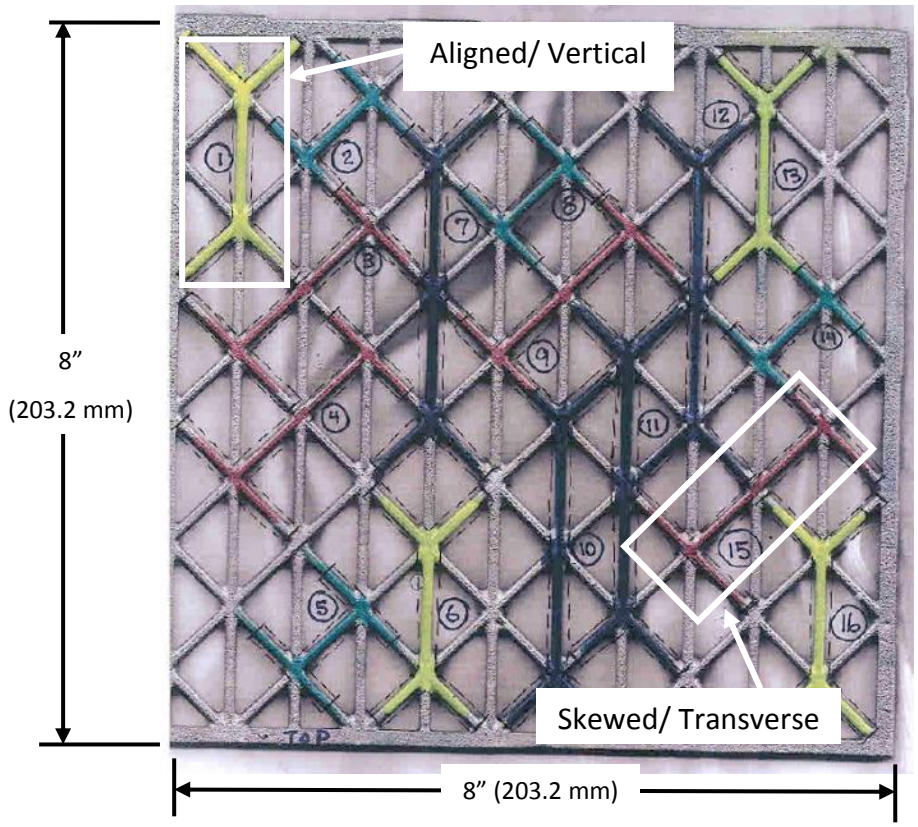

Figure 3.1: Typical Marked Panel for Cutting of Facesheet Specimens

Two specimen orientations, identified in Figure 3.1 as aligned/ vertical and skewed/ transverse, were adopted in the test protocol. The specimens were cut in different orientations so that directional property variations, if any, could be

determined. Each facesheet specimen orientation allowed for test specimens of two lengths, i.e. ligaments and legs, discussed earlier. The purpose of this was to determine how the stiffness and strength of the subelement is affected when a node is present in the gage section of the test specimen. Thus, four different facesheet tensile test specimen geometries (Figure 3.2) were extracted for testing. The specimen design was also chosen to make gripping the specimens more convenient (described later). Specimens that are aligned vertically as pictured in Figure 3.1 are denoted very simply as "vertical" specimens. Specimens that are skewed 45° as pictured in Figure 3.1 are denoted as "transverse" specimens. The naming convention is straightforward when observing the finished specimens in Figure 3.2. Vertical specimens appear with a "V" on both ends, and transverse specimens appear as a "T" shaped specimen. Pictured from left to right in Figure 3.2 are a vertical ligament, a vertical leg, a transverse ligament, and a transverse leg. As discussed earlier, a ligament contains no central node and a leg contains a central node. The extraneous material around nodes and at the specimen ends were mistakenly ground off during specimen prep and are not pictured in Figure 3.2. This process caused some premature failures at machining nicks and will be discussed with the test results. Several specimens were prepared from a single panel, and their location in the panels were randomized to establish within-panel variability.

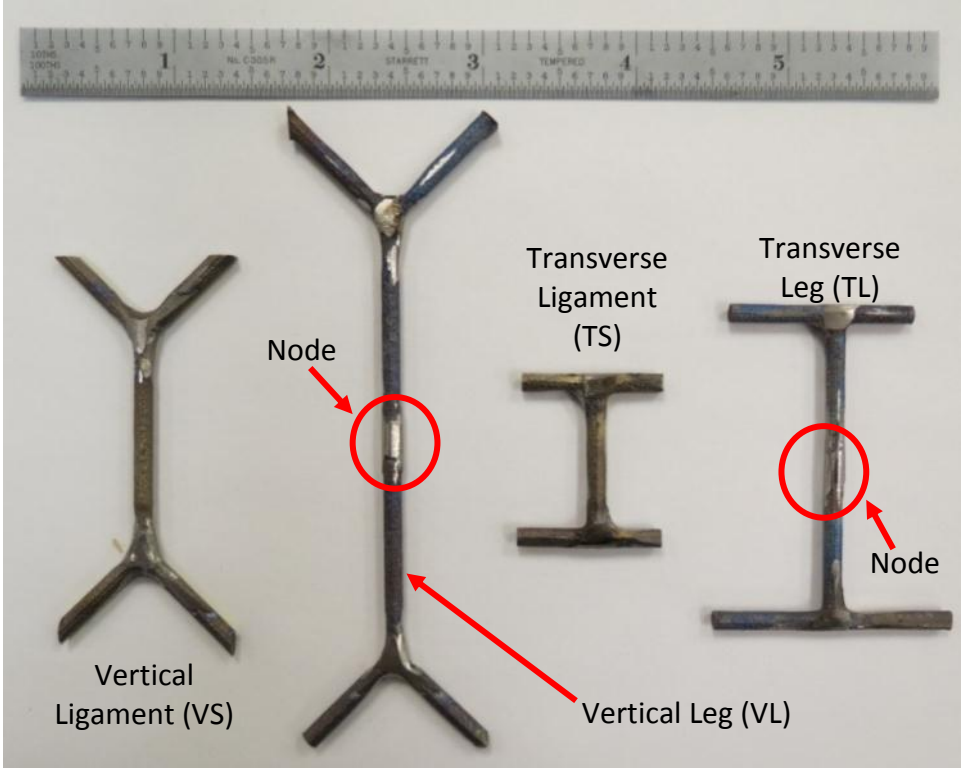

Figure 3.2: Specimen Geometries for Tensile Testing of Ti-6-4

3.3 Preparation of Samples Obtained from the Internal Lattice

Struts for compression test specimens (Figure 3.3) were cut at random from the internal lattice using EDM. The cross sections at the end of the specimens were ground parallel to each other, and perpendicular to the specimen sides. Note that, again, obvious casting flaws were avoided. The specimens were cut initially with a height to diameter ratio of 2:1, which is consistent with American Society for Testing and Materials (ASTM) E9-09 (31) and previous testing (21). Local bending issues arose during testing and the specimen height to diameter ratio was reduced to 1.5:1 for the

Ti-6-4 specimens and to 1.15:1 for the NiTi specimen. This is discussed in the final chapter in more detail.

Figure 3.3: Typical Compression Specimen

3.4 Test Fixtures[6]

After tensile specimens were obtained from the facesheet, a gripping mechanism had to be devised. Potting tensile test specimens was tried initially due to the simplicity of the process. Potting means simply encasing the ends of a test specimen in an epoxy resin so the specimen can be easily inserted and gripped in a test frame. At first, flat metal tabs with dimensions 0.625 inch x 0.75 inch x 0.03 inch (15.88 mm x 19.05 mm x 0.76 mm) were glued with epoxy to the ends of specimens. For the tabbed specimens, the epoxy tended to crack and allowed the tabs to fall off the specimens (Figure 3.4) under load. This failed approach to potting specimens was followed by a procedure where 1.0 inch x 0.5 inch x 1.0 inch (25.40 mm x 12.70 mm x 25.40 mm)

[6] All fixture drawings can be found in Appendix B

channels were filled with epoxy that encased the ends of the specimens. For the filled specimens, the potting material was crushed if the grip pressure was too high (Figure 3.5). Crushing of the specimens could be avoided by lowering the grip pressure, but then the specimens slipped as uniaxial load was applied. A third approach to fabricating potted specimens involved filling copper tubes with a nominal diameter of 0.625 inch and a length of 1.5 inch (Ø15.88 mm x 38.10 mm) with epoxy resin. However, this system failed as well. The most significant problem with potted specimens was that the epoxy potting was not strong enough and the samples would simply pull themselves out during testing (Figure 3.6). The primary cause of this failure was that there was not enough area of potting in the cross section around the specimen. Larger tabs, larger channels, or larger tubes may have been more beneficial. However, limited clearance in the wedge and collet grips on the test frame could not accommodate specimens with larger ends. Given these challenges, a mechanical gripping mechanism was designed.

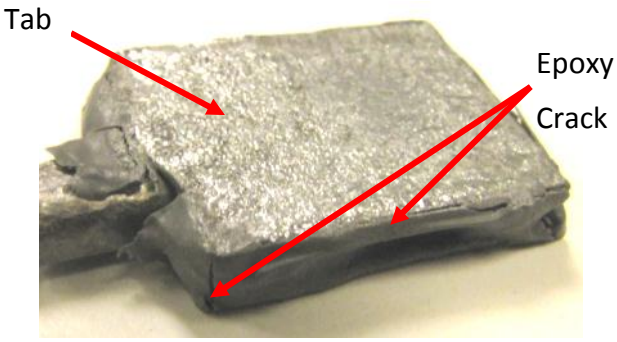

Figure 3.4: Tabbed Specimen with Cracked Epoxy

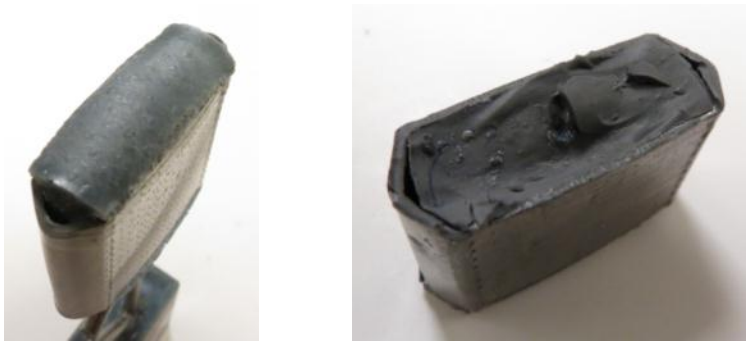

Figure 3.5: Crushed Potted Specimens

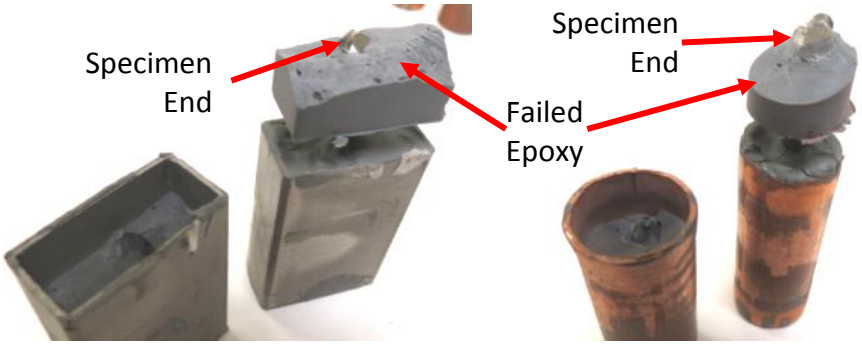

Figure 3.6: Epoxy Failures

Designing a mechanical gripping fixture for the transverse specimens posed the severest design challenge. The test specimens were consistent from one specimen to another. However, slight offsets at the nodes within a test specimen made it difficult to assure that the fixtures would not impart bending during a test. A clamshell design was selected which consists of two halves that are mirror images of one another. A third piece is an insert that restrains the specimen from the bottom to keep the specimen "arm" (Figure 3.7) from bending during a test. Figure 3.8 is an exploded model view of the test fixture and depicts a series of threaded and through holes that allows the fixture to be screwed together for rapid sample changes. The fixture is pin loaded

through the slotted hole located at the fixture center. All fixtures used in this testing effort were machined from high strength AerMet®-100 alloy.

Figure 3.7: Transverse Specimen "arm"

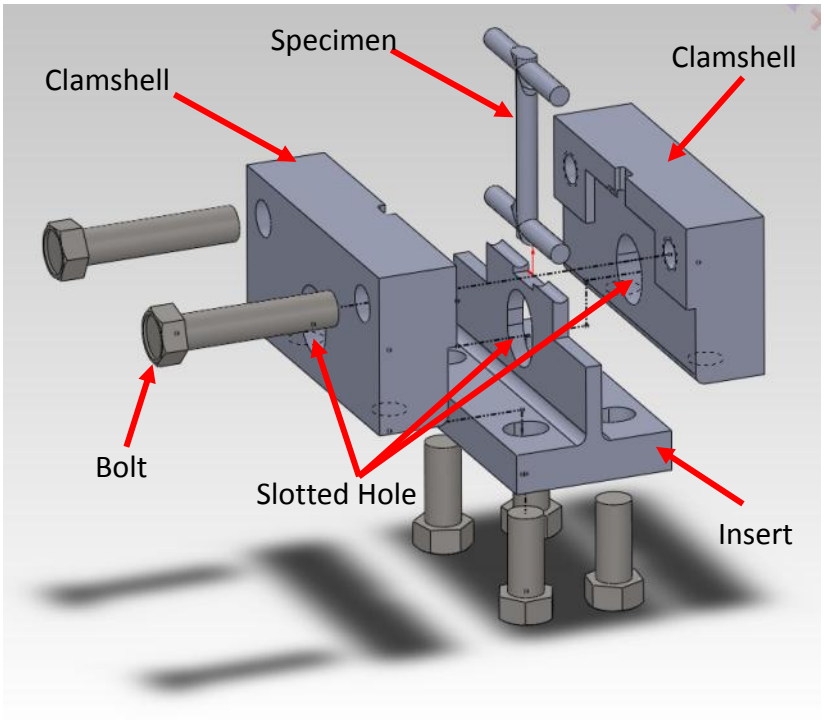

Figure 3.8: 3D Exploded Model of Transverse Specimen Fixture

Tensile properties from previous studies on titanium lattice block material indicated a test specimen ultimate strength of 134 ksi (924 MPa) (21). Applying a safety factor of 1.5 resulted in a required fixture yield strength of at least 201 ksi (1386 MPa).

The estimated force the fixture would be subjected to during a test was calculated simply by

$$F = \sigma A \tag{3.1}$$

where σ = 201 ksi and the nominal cross sectional area of the test specimen is A = 0.012 in^2. Using this strength value and the cross sectional area of the specimen results in a force at failure of approximately 2.41 kips (10.7 kN). No load from the test is passed to the insert because of an oversized slotted hole in the center where the load pin passes (Figure 3.8). Small compressive loads on the top surface of the insert where the specimen "arm" is located during testing are possible but considered negligible. Because of this, the load was estimated to be evenly divided between the two clamshells. This results in a load of 1.21 kips (5.37 kN) per clamshell half.

A stress analysis was conducted on one clamshell of the fixture. The boundary conditions for the clamshell analysis consisted of fixing the load pin location in the slotted hole with a subsequent application of a vertical force on the curved load surface. The small bolt holes in the fixture were constrained from translating forward and back with respect to the large flat face of the clamshell. Figure 3.9 shows an exaggerated deformation state with overlaid stress distribution and annotated boundary conditions for one half of the transverse test specimen fixture. The highest von Mises stress in the fixture for the final design was 127 ksi. This value is roughly 49% less than the 250 ksi (1724 MPa) yield strength of the fixture material. The analysis shows that fixture failure is unlikely.

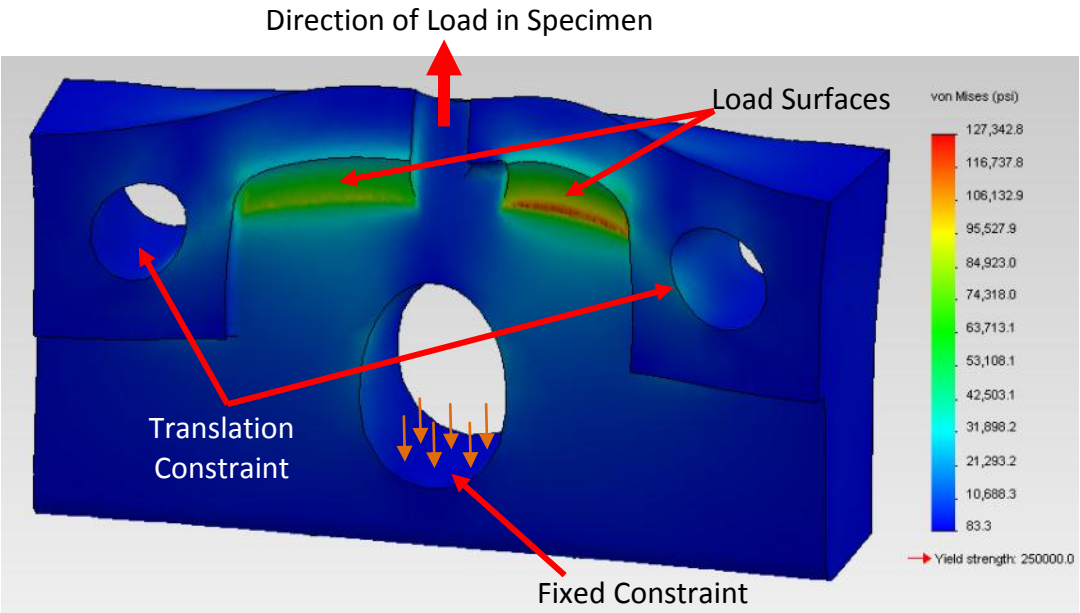

Figure 3.9: von Mises Stress of Transverse Fixture

The primary design constraint was keeping the overall size of the fixture as small as possible and to achieve this, the design was modified in an iterative fashion. Once the model was optimized, a rapid prototype of the fixture was fabricated from ABS plastic to test specimen tolerances. The rapid prototype is shown in Figure 3.10. With the tolerances verified, the final specimens were machined from the Aer-Met®-100 alloy and heat treated. Figure 3.11 depicts the finished fixture.

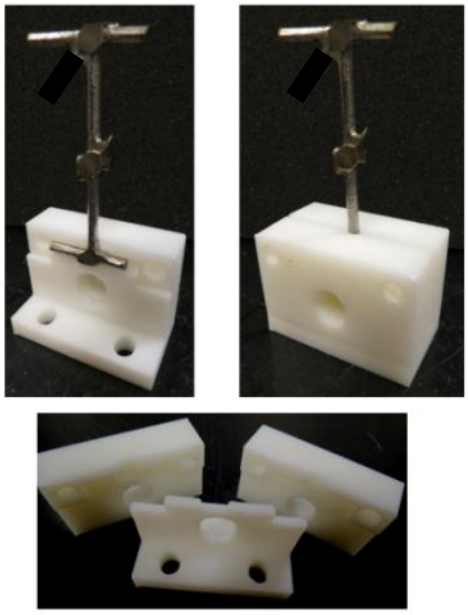

Figure 3.10: Rapid Prototype of Transverse Specimen Fixture

Figure 3.11: Machined and Heat Treated Transverse Specimen Fixture

A similar fixture was designed for the vertical test specimens (Figure 3.12). An exploded model view of the test fixture is shown in Figure 3.13. It again, incorporates a two-piece mirrored clamshell with an insert. Through and threaded holes are machined into in the upper corners of the clamshells and into the bottom to allow the fixture to be

securely fastened together. Load is transmitted to the fixture clamshells through a central slotted hole. An insert acts as a restraint to keep the specimen "arms" (Figure 3.12) from bending during the tensile test which would permit the test specimen to pull out of the fixture. Consistent with the transverse fixture insert, the slotted hole is oversized so very little load is passed to the insert during a test.

Figure 3.12: Vertical Specimen "arm"

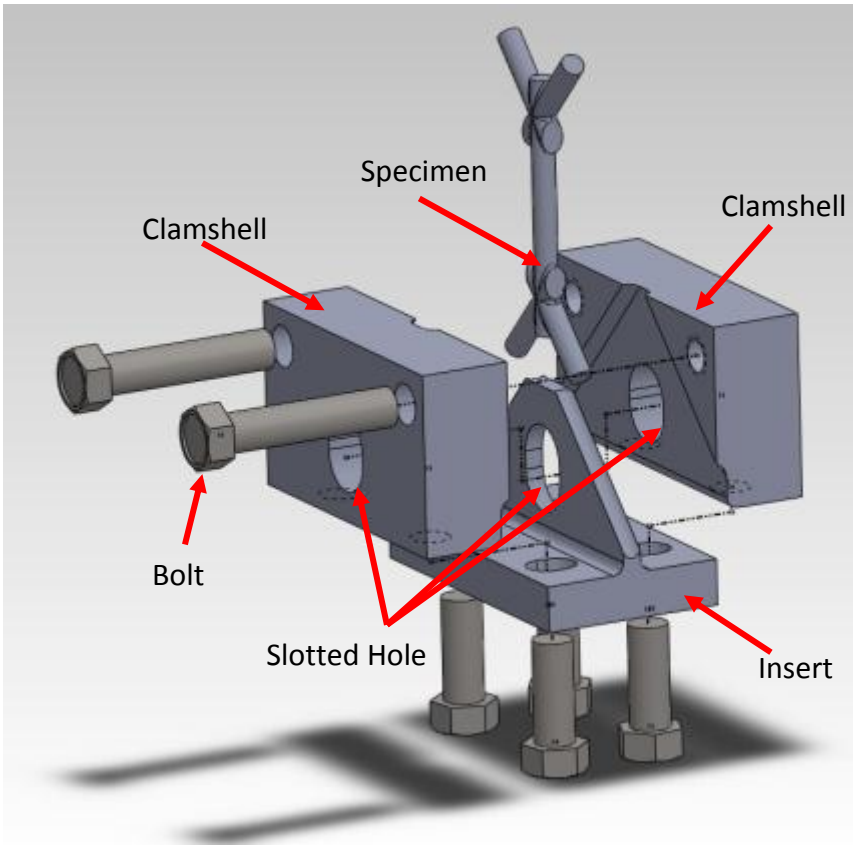

Figure 3.13: 3D Exploded Model of Vertical Specimen Fixture

A finite element analysis was conducted on this test fixture as well. Load was applied vertically on the angled curved surfaces as shown in Figure 3.14. Boundary conditions consistent with the transverse clamshell fixture were employed for the vertical clamshell fixture. Figure 3.14 depicts the boundary conditions and the exaggerated deformation state of the fixture at maximum load with the von Mises stress depicted. This figure shows that the maximum von Mises stress is approximately 40% below the yield strength of the fixture material. This indicates that the fixture will not fail under normal test conditions. After the design of the fixture was optimized, rapid prototypes were fabricated and are shown in Figure 3.15. A vertical test specimen was used to successfully check the fit of the fixture and machine drawings were executed. The test fixtures were then machined and heat treated. The final test fixture is depicted in Figure 3.16.

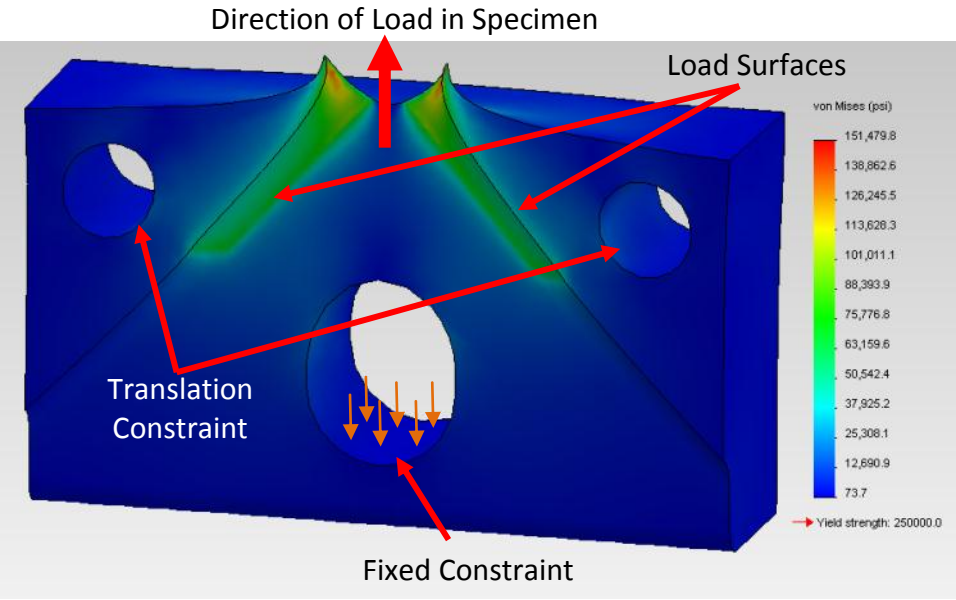

Figure 3.14: von Mises Stress of Vertical Fixture

Figure 3.15: Rapid Prototype of Vertical Specimen Fixture

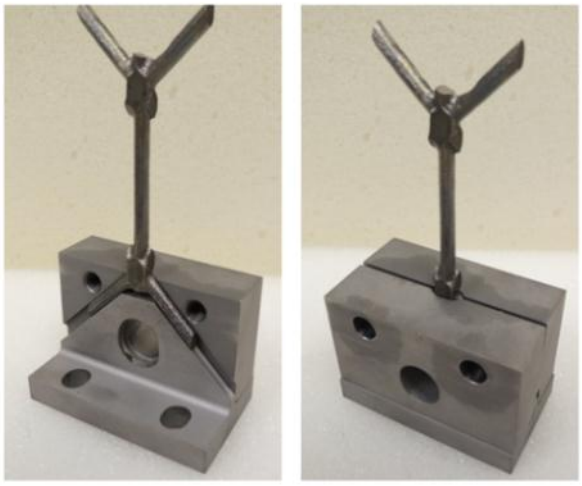

Figure 3.16: Machined and Heat Treated Vertical Specimen Fixture

An attachment fixture that allowed for efficient mounting of the facesheet specimen fixtures to the test frame was required. A simple "C" clevis assembly (Figure 3.17 and Figure 3.18) was designed to mount and attach test specimens in the fixture. This design was optimized to allow for screw clearance of the facesheet fixtures and incorporated a pin for transferring load. The design of the clevis-pin assembly allows

the test fixture to pivot about the pin to accommodate specimen misalignment. The clevis is connected to the collet grip of the test frame via a shaft that sits in a recess at the bottom of the clevis and allows for the rotations depicted in Figure 3.17. To ensure the pin could withstand test loads, simple hand calculations were performed using equations found in Budynas (32). These calculations lead to a shear stress in the pin of

$$\tau_{max} = \frac{4V}{3A} = 15.8\ ksi \tag{3.2}$$

with V = 1205 lbf (5360 N). The shear force, V, represents half of the maximum estimated load the test specimen will incur. The cross sectional area of the pin is A = 0.102 in^2 (65.8 mm^2). The maximum estimated shear stress on the pin is considerably less than the 175 ksi (1207 MPa) maximum shear strength of the pin material (33). Bending stresses on the pin are

$$\sigma_{max} = \frac{Mc}{I} = \frac{32VD}{\pi d^3} = 32.9\ ksi \tag{3.3}$$

with a pin diameter of d = 0.36 inch (9.1 mm). D = 0.125 inch (3.18 mm) is the bending moment arm, which is the distance between the inside of the clevis and the outside of the fixture block. The maximum bending stress is almost double the shear stress, but it is still considerably lower than the pin material yield point of 250 ksi (1793 MPa). Due to the simplicity of the design and the availability of simple hand calculations, finite element analyses were not performed on the clevis assembly. Similarly, rapid prototypes of the clevis-pin assembly were not required because of the simplicity of the

design. The complete test fixture with a mounted specimen installed in the test frame is shown in Figure 3.18.

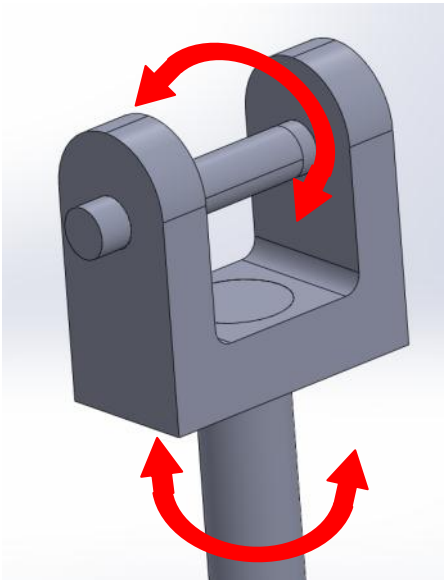

Figure 3.17: Clevis-pin Assembly

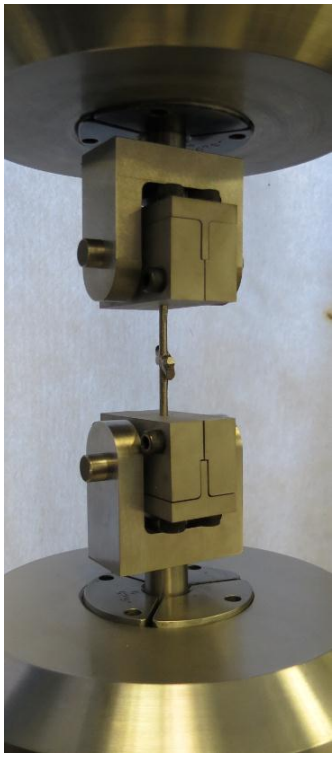

Figure 3.18: Assembled Fixture with Specimen Mounted in Test Frame

The final fixture required for testing is the compression fixture (Figure 3.19). It is simply a 0.625 inch (15.9 mm) round bar of 6 inches (152.4 mm) or 8 inches (203.2 mm) in length for the top and bottom grips in the test frame, respectively. The end surfaces are ground flat to ensure a flat mounting surface. Because high local stresses from the compression specimens will dent the pushrods, ground and polished alumina[7] platens were placed on top of the push rods for testing. Stress analysis was not completed on these fixtures.

Figure 3.19: Compression Testing Rods with Alumina Platens

3.5 Test Frame and Heating Chamber

All mechanical testing for this project was completed on a servo hydraulic uniaxial test frame (Figure 3.20) with a force capacity of ±22 kips (±980 kN). For all tests, the test frame's data acquisition system acquired load and crosshead displacement data. A metal cabinet with a hinged, impact resistant plastic front door surrounds the test frame. The metal cabinet and plastic door prevent failed specimens from being ejected from the test frame when specimens explosively fail. During testing, the upper

[7] See Appendix A.5 for more information on alumina

crosshead remains fixed, while the lower hydraulic ram travels up or down. Test fixtures were mounted into hydraulically actuated collet grips (Figure 3.21).

Figure 3.20: 22kip Servohydraulic Test Frame

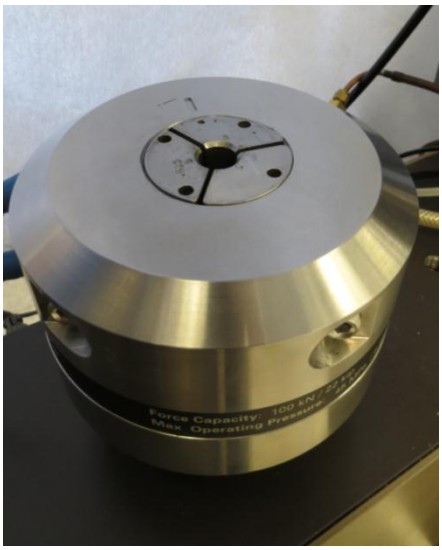

Figure 3.21: Hydraulic collet grip

The test frame and load cell were calibrated to NASA internal standards. Following calibration, the machine was aligned to NASA specifications. Proper alignment is important so that a tensile or compression test is loaded uniaxially and bending moments are not imparted to the test specimen from the load train.

Strength tests were conducted at temperature and the maximum test temperature was 392 °F (200 °C). A chamber was modified that provided a line-of-sight view for optical strain measurement and to allow the use of mechanical extensometry (both described in the next section). The furnace (Figure 3.22) originally included in-house manufactured items, i.e., a heater control box, a stand to mount the furnace on the test frame, a four sided quartz windowed chamber, and a lid for the chamber. In addition, a heat pipe for warming shop air that is piped into the chamber was purchased commercially. Furnace chamber modifications were required to achieve the desired test temperatures. Two of the thin side panels were replaced with 0.125 inch (3.18 mm) stainless steel sheet stock, with one of the replacement panels containing an opening to allow for an extensometer. In addition, the front window panel of the furnace was replaced with a removable door and a smaller quartz window. Next, two additional 400 watt in-line heat pipes were added outside the furnace along with a 1200 watt electric grid heater affixed to a wall inside the furnace. Finally, the entire furnace was heavily insulated and wrapped in aluminum sheeting. The rear quartz window was left intact for the optical strain measurement cameras. Figure 3.22 shows the modified furnace from the front (left image) and from the rear (right image). Prior to testing it was

confirmed that the temperature gradient of the furnace for elevated temperature testing was consistent with the specifications outlined by Lerch (34).

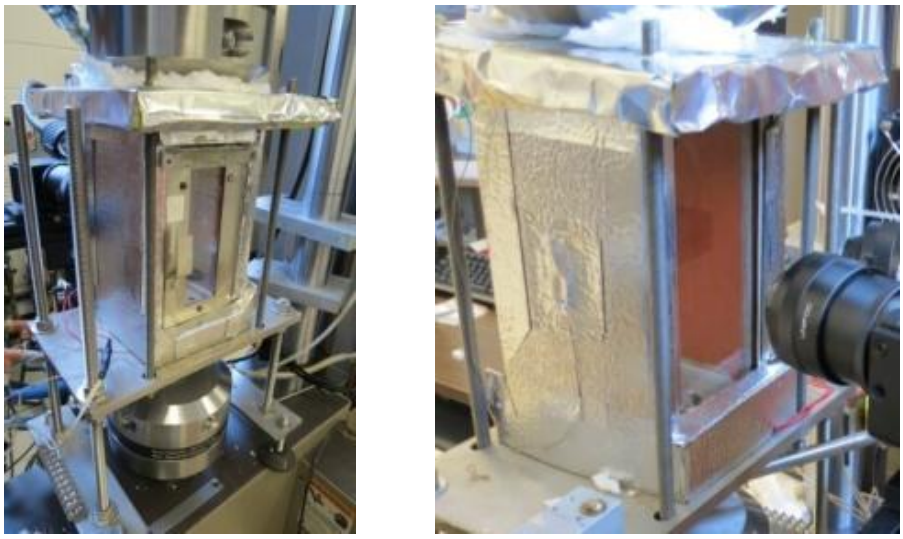

Figure 3.22: Quartz Paneled Furnace Front (Left) and Rear (Right)

3.6 Extensometry

A light contact extensometer with high temperature alumina probes was originally planned for use in all applications requiring strain control. This type of extensometer is widely used for tension testing. The extensometer has a 0.5 inch (12.7 mm) gage length with a travel of -0.08 inch to +0.1 inch (-2.03 mm to +2.54 mm). The 0.5 inch gage of the extensometer proved to be too large to fit between the fixture of the smaller tensile specimens. The extensometer was modified with step-down adapters to reduce the gage from 0.5 inch to 0.25 inch (6.35 mm). This adaptation is shown in Figure 3.23. The step-down adapters also extended the length of the probes. The extensometer was calibrated before use with the adapters attached.

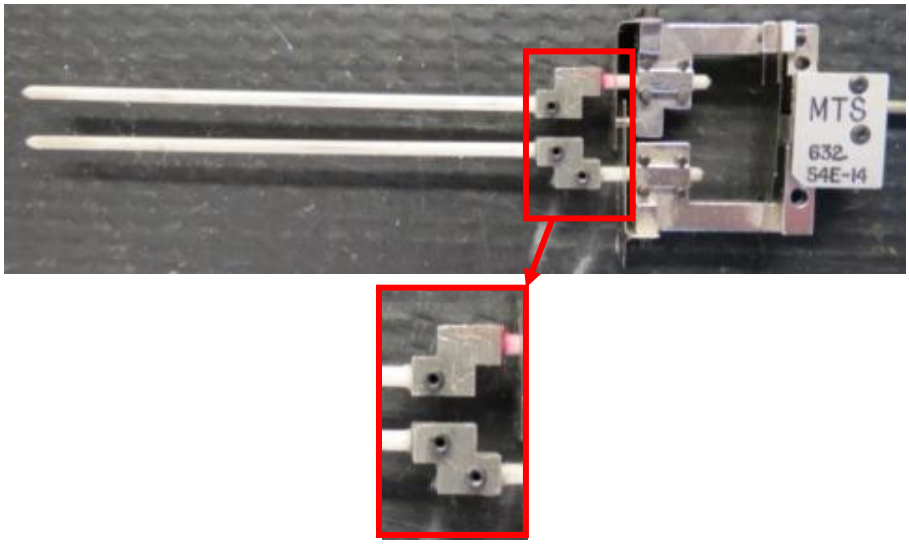

Figure 3.23: High Temperature Extensometer with Step-down Adapters

When the modified extensometer was used in tensile tests problems were encountered maintaining contact between the test specimen and the modified extensometer. The reason for this is that the specimen surfaces are rough in texture (as-cast) and are not machined. This caused the extensometer to sit unevenly on the specimen surface and to slip during testing, causing machine stability problems when attempting to run tests in strain control. Gluing the probes in place helped, but high temperature testing tended to burn the glue off. In addition, the clevis and specimen fixtures, discussed previously, were designed with a bit of slack to facilitate easier installation of the specimens into the test frame and for removing bending in the specimens. This "play" in the system caused the extensometer to lose feedback control near zero loads. After several failed attempts at conducting tensile tests under strain control, it was decided that tensile tests would be conducted in displacement and load control.

Since mechanical extensometry was not a viable option for measuring strain, a non-contact optical strain measuring device was utilized. Optical extensometry is very useful for unusual specimen geometries that do not allow for the application of strain gages or the use of extensometers. The device consists of dual five mega-pixel cameras, a computer, and a trigger box. Figure 3.24 shows a typical test configuration with the optical measuring device. For testing at elevated temperatures, lenses were mounted on the cameras that blocked ultraviolet light and reduced the glare on the specimen.

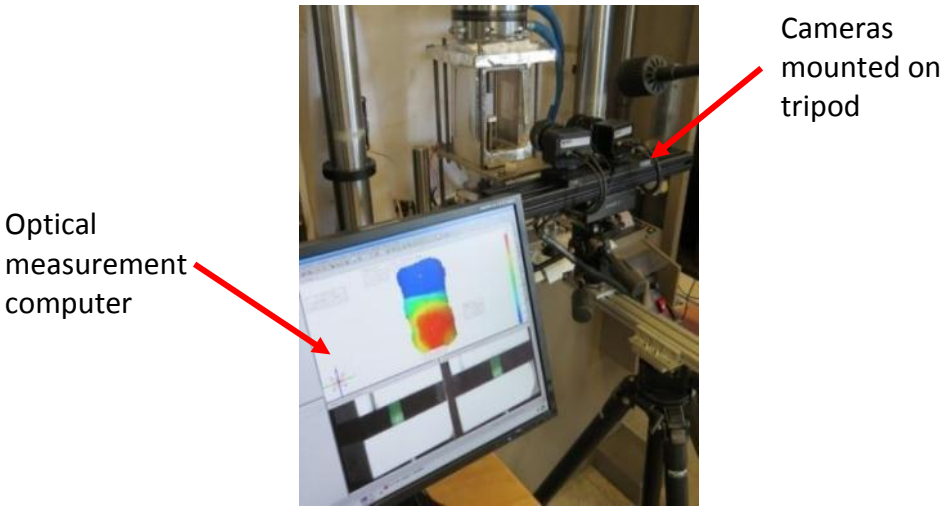

Figure 3.24: Computer with Stereo Cameras Mounted for Testing

A trigger box within the optical extensometry system signals the cameras to take pictures at a user specified rate. The acquisition system allows for up to eight external input channels (±10 volt) to be acquired during a test. These inputs can include displacement, load, strain gages, extensometers, or thermocouples. The image correlation system is calibrated before starting a series of tests and checked periodically to be sure it is still within minimums. For the optical system to operate, the system must be calibrated with a calibration panel (Figure 3.25). The optical strain measuring

device proved quite viable and was used throughout the study. The Linux based software processed the acquired images and calculated the three-dimensional displacement and three-dimensional surface strains. Through trial and error, an acquisition rate that collected 300 data points per test was adopted. The system is slow to process larger image files and this acquisition rate optimizes computation times simply by minimizing the amount of data to process. The software is efficient and accurate for test temperatures ranging from -148 °F to 2732 °F (-100 °C to +1500 °C) (35).

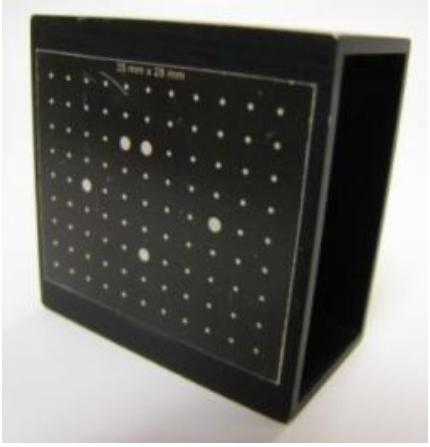

Figure 3.25: Typical Calibration Panel

Optical extensometry works by tracking the three dimensional movement of points that are painted on the surface of the test specimen. For this project, test specimens were first painted with a light coat of white spray paint and then "speckled" with a mist of black spray paint (Figure 3.26). Once a test is complete and the software has processed the image files, the user can view and rotate a three-dimensional rendering of the test specimen. The software is capable of exporting images and/ or

videos showing the deformations and strains from a test. Also, positional data associated with user defined points on the specimen can be exported in ASCII format to a spreadsheet.

Figure 3.26: Typical Painted Tension Specimen

3.7 Mode Control

Mechanical strength tests can be conducted by actively controlling the load rate, the displacement rate, or a combination of the two when complex test histories are required (i.e., interrupted stress tests). Deciding on a stable control mode to conduct the tests is challenging. The original plan for this project was to complete all testing in strain control. Problems discussed previously with the mechanical extensometer led to most testing on Ti-6-4 test specimens (discussed in the following chapter) being completed in displacement control. Displacement control is the most stable and simplest control mode to use. Strain rate sensitive materials can show large discrepancies between data obtained from strain controlled experiments and displacement controlled tests. Strain control is the preferred mode for uniaxial testing because the testing is performed at a constant deformation rate, however ASTM

standards allow displacement control as an acceptable method for conducting tensile or compression tests.

For materials with linear stress-strain curves in the elastic response regime, like Ti-6-4, there is no difference in mechanical properties between control modes of testing. A small number of Ti-6-4 tests were completed in load control to demonstrate no appreciable difference in material properties when tests were conducted in different control modes. All NiTi tests were completed in load control because that material has highly rate dependent material properties.

3.8 Test Standards

A literature search of test standards was conducted before any tests were completed. As a result, tensile tests in this study were conducted based on ASTM E8/E8M, Standard Test Methods for Tension Testing of Metallic Materials (36). ASTM E9-09 (31), Standard Test Methods of Compression Testing of Metallic Materials at Room Temperature, and ASTM E209-00 (37), Standard Practice for Compression Tests of Metallic Materials at Elevated Temperatures with Conventional or Rapid Heating Systems, were followed when compression tests were conducted. ASTM F2516-07 (38), Standard Test Method for Tension Testing of Nickel-Titanium Superelastic Materials was consulted when testing the shape memory alloy materials.

CHAPTER IV

BASELINE TESTING: Ti-6-4

4.1 Introduction

Ti-6-4 was selected as the comparative baseline material for this study of lattice block structures because castings from this material are high quality and because there is a wealth of available test data in the open literature. Transition 45 Incorporated produced multiple Ti-6-4 panels for this study. Table I contains a summary of pertinent information for the Ti-6-4 panels. This information includes the serial number assigned to each panel by the manufacturer which is helpful in cross referencing manufacturer data if necessary. The nominal size represents the overall dimension of each panel. Final processing information conveys how the manufacturer removed the investment casting medium from the panel. Finally, information as to what type of test was conducted on the specimens is provided.

Table I: Ti-6-4 Lattice Block Structure Panel Designation

Panel	Manufacturer Serial Number	Nominal Size (in)	Final Processing	Use
1	64, Ti-6-4	3x3	Chemically Milled	Frame Validation Specimens Chemical Evaluation
2	3, Ti-6-4	3x3	Chemically Milled	Frame Validation Specimens Metallographic Evaluation
3	6, Ti-6-4	8x8	Chemically Milled	Tension/ Compression Specimens
4	13, Ti-6-4	8x8	Abrasive Blast	Tension/ Compression Specimens Chemical Evaluation

All four panels were subjected to nondestructive evaluation (NDE). NDE provides defect maps of the panels.[8] Panel 1 contained a few node defects, all of which were repaired with welds. Panel 2 contained a few minor surface defects. Panel 3 (denoted as P6 in the test data) contained a small number of surface connected holes at the nodes. Panel 4 (denoted as P13 in the test data) contained a few open pores at the nodes from poor casting and contained a visual defect. When sectioning the panels to obtain test specimens, these minor defects were easily avoided.

[8] Full defect maps for Ti-6-4 Panels are provided in Appendix C

4.2 Ti-6-4 Tensile Testing

At each test temperature (room temperature, 165 °C, and 200 °C) all tension tests for VL, VS, and TL test specimens (Figure 3.2) were conducted at a displacement rate of 0.0014 in/s to approximate a strain rate of 10^{-4} in/in/s. For all elevated temperature testing, specimens were brought to temperature within 30 minutes and allowed to soak for 15 minutes at temperature before being tested.

Because of the limited number of test specimens, only one TS specimen was tested in load control at each test temperature. All other TS specimens were tested in displacement control at the rate specified above. Load controlled testing was completed at a load rate of 29 lbf/s to approximate a strain rate of 10^{-4} in/in/s, assuming a linear response. All tables and plots presented herein use "true" values as opposed to "engineering" values. True stress and true strain are calculated using the following relations from Ling (39).

$$\sigma_t = \sigma_e(1 + \epsilon_e) \tag{4.1}$$

and

$$\varepsilon_t = ln(1 + \epsilon_e) \tag{4.2}$$

Here σ_e is the engineering stress and ε_e is the engineering strain. The engineering stress is calculated by taking current force divided by the initial cross sectional area of the specimen. The engineering strain is calculated by taking current elongation divided by the initial specimen length.

Values of elastic modulus, yield stress, ultimate strength, Poisson's ratio, percent elongation, and percent area reduction were determined from the test data collected. Modulus values were calculated using a trendline fit to the linear portion of the stress-strain curve. The yield stress was determined using a 0.2% offset from the modulus trendline. The ultimate strength is the maximum true stress computed from the test data. Poisson's ratio is calculated from a trendline fit to a plot of the transverse strain versus the axial strain. The elongation is the percent strain at failure. The percent area reduction is the ratio of the starting nominal cross sectional area of the specimen to the cross sectional area of the specimen at the failure location. When specimens failed in the grips, only values of elastic modulus and Poisson's ratio were extracted from the test data.

For the three test temperatures (room temperature, 165 °C, and 200 °C) the data were averaged on a per panel basis to determine panel variability associated with processing. Then an overall average was computed of all data at a given test temperature.[9] Table II summarizes the strength related data for the Ti-6-4 tension tests. Also contained in Table II is the number of specimens tested from a given panel for a given temperature. Table III summarizes the deformation properties of the Ti-6-4 tension tests. Note that the panel averages do not equal the overall average at a given temperature, identified as "Average" in the tables. This is because data sets of the different specimen orientations do not contain equal numbers of specimens cut from panels P13 and P6. The material property average was weighted with respect to the

[9] Extended data tables are provided in Appendix D for all testing

number of P13 and P6 specimens in the data set. The data in Table II shows that panel P6 appears slightly stiffer and stronger than panel P13. However, because of a small sample size and the scatter present within the data indicated by the large standard deviations in the test data, no conclusion can be made as to whether a material property difference exists between the panels that could be attributed to final processing or control mode of testing. A comparison to published data is presented later in this section. Possible sources for scatter in the data are discussed in the final chapter.

Table II: Ti-6-4 Strength Data

Room Temp

	Tested Specimens	Modulus (psi)	Modulus (GPa)	Yield Stress (psi)	Yield Stress (MPa)	Ult Strength (psi)	Ult Strength (MPa)
P13 Avg	13	16,573,922	114.27	118,058.39	814.20	129,897.69	895.85
P13 St. Dev		664,536	4.58	9,397.09	64.81	16,613.73	114.58
P13 Coeff. Var.		0.04	0.04	0.08	0.08	0.13	0.13
P6 Avg	4	16,991,479	117.15	124,911.27	861.46	144,216.56	994.60
P6 St. Dev		2,793,104	19.26				
P6 Coeff. Var.		0.16	0.16				
Average	17	17,040,878	117.49	120,342.68	829.95	134,670.65	928.76
St. Dev		746,126	5.14	7,733.47	53.33	14,364.94	99.07
Coeff. Var.		0.04	0.04	0.06	0.06	0.11	0.11

165 C

	Tested Specimens	Modulus (psi)	Modulus (GPa)	Yield Stress (psi)	Yield Stress (Mpa)	Ult Strength (psi)	Ult Strength (MPa)
P13 Avg	5	14,353,745	98.97	89,269.46	615.65	106,186.31	732.32
P13 St. Dev		1,332,586	9.19	1,798.02	12.40	8,176.60	56.39
P13 Coeff. Var.		0.09	0.09	0.02	0.02	0.08	0.08
P6 Avg	7	15,448,406	106.51	87,976.07	606.73	109,595.80	755.83
P6 St. Dev		1,634,590	11.27	2,595.18	17.90	7,552.20	52.08
P6 Coeff. Var.		0.11	0.11	0.03	0.03	0.07	0.07
Average	12	15,190,989	104.74	88,731.38	611.94	107,723.59	742.92
St. Dev		782,664	5.40	2,146.80	14.81	7,444.90	51.34
Coeff. Var.		0.05	0.05	0.02	0.02	0.07	0.07

200 C

	Tested Specimens	Modulus (psi)	Modulus (GPa)	Yield Stress (psi)	Yield Stress (Mpa)	Ult Strength (psi)	Ult Strength (MPa)
P13 Avg	7	14,961,095	103.15	80,601.74	555.87	99,677.45	687.43
P13 St. Dev		1,586,429	10.94	4,512.70	31.12	4,717.14	32.53
P13 Coeff. Var.		0.11	0.11	0.06	0.06	0.05	0.05
P6 Avg	5	14,012,787	96.61	80,733.01	556.78	105,460.54	727.31
P6 St. Dev		1,260,948	8.69	6,354.15	43.82	1,442.11	9.95
P6 Coeff. Var.		0.09	0.09	0.08	0.08	0.01	0.01
Average	12	14,699,347	101.35	81,478.57	561.92	100,826.79	695.36
St. Dev		1,238,143	8.54	3,161.80	21.81	5,072.79	34.98
Coeff. Var.		0.08	0.08	0.04	0.04	0.05	0.05

Table III: Ti-6-4 Deformation Properties

Room Temp			
	Poisson's Ratio	% Elongation	% Area Red.
P13 Avg	0.292	4.36%	20.43%
P13 St. Dev	0.015	1.51%	3.00%
P13 Coeff. Var.	0.050	34.60%	14.70%
P6 Avg	0.326	5.74%	17.16%
P6 St. Dev	0.005		
P6 Coeff. Var.	0.014		
Average	0.301	4.82%	19.34%
St. Dev	0.022	1.33%	2.84%
Coeff. Var.	0.073	27.63%	14.69%
165 C			
	Poisson's Ratio	% Elongation	% Area Red.
P13 Avg	0.322	5.35%	27.74%
P13 St. Dev	0.046	2.89%	10.67%
P13 Coeff. Var.	0.142	53.99%	38.48%
P6 Avg	0.302	7.43%	31.45%
P6 St. Dev	0.019	2.35%	9.15%
P6 Coeff. Var.	0.061	31.68%	29.10%
Average	0.310	6.24%	27.25%
St. Dev	0.023	2.16%	11.03%
Coeff. Var.	0.073	34.57%	40.47%
200 C			
	Poisson's Ratio	% Elongation	% Area Red.
P13 Avg	0.294	6.86%	33.40%
P13 St. Dev	0.026	4.43%	6.87%
P13 Coeff. Var.	0.090	64.67%	20.56%
P6 Avg	0.336	8.85%	37.82%
P6 St. Dev	0.017	2.68%	5.32%
P6 Coeff. Var.	0.050	30.34%	14.08%
Average	0.311	6.92%	34.10%
St. Dev	0.018	4.03%	6.51%
Coeff. Var.	0.059	58.32%	19.09%

Figure 4.1 is series of images showing the full field axial surface strain for a tensile test conducted on a specimen that did not contain a node in the gage section. The images represent strain at four different stages of the test. Since this test was conducted under displacement control these stages were equally spaced from a temporal standpoint. A strain scale is shown using a color spectrum. Note that the load

direction is indicated in the images. From early in the test, high local strain begins to form in the gage section while the rest of the specimen contains relatively low strain. The specimen failed in the center of the gage with approximately 25% local strain while the global strain was between 2.5%-5.0%. Since the specimens are cast, the surface is non-uniform and the specimen failed at a local reduction of cross sectional area. The pattern of strain distribution shown is common to specimens that failed in the gage.

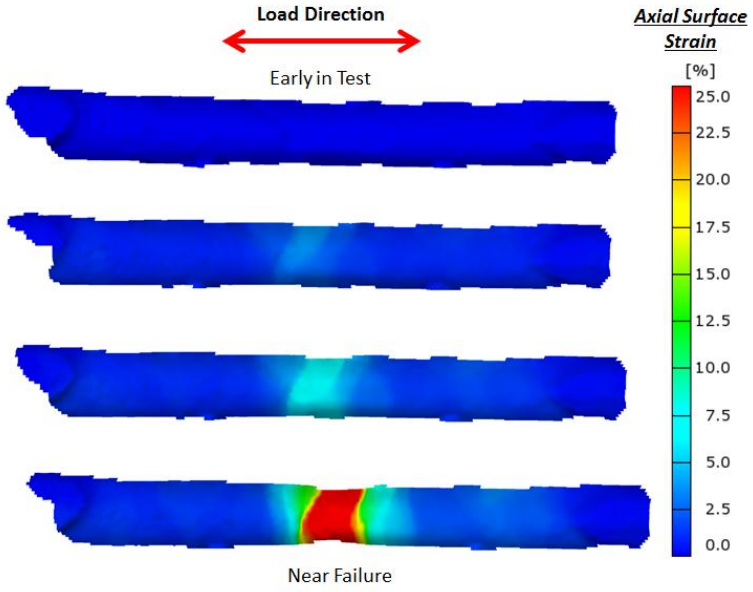

Figure 4.1: Axial Surface Strains for a Tensile Specimen Containing No Node

Figure 4.2 is a full field axial surface strain image series for a tensile test on a specimen with a centrally located node. Note that the images are again evenly distributed over the test from a temporal standpoint. The tensile test with a node begins to show high localized strain developing early in the test. In this case, the high strain develops in the near vicinity of the node, which is expected. As the test approaches failure, the localized strain increases to approximately 20% in the region

neighboring the node and the specimen fails at that location. Global strain on the rest of the specimen ranges between 3%-5% at failure. All other specimens that contained nodes failed with a similar pattern of strain distribution.

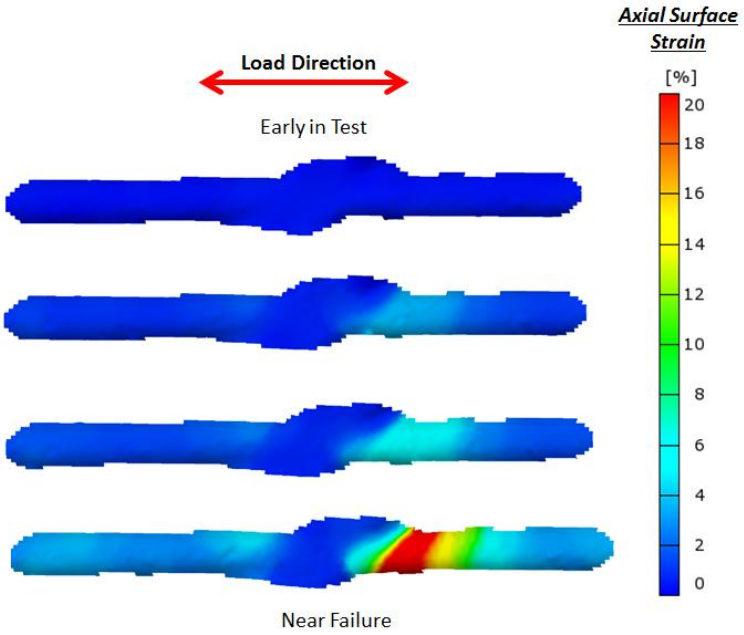

Figure 4.2: Axial Surface Strains for a Tensile Specimen with a Node

To show the correlation of test data across the different specimen types, all tensile specimen tests for a given temperature are shown on one graph. Figure 4.3, Figure 4.4, and Figure 4.5 depict the stress strain curves for room temperature, 165 °C, and 200 °C tests, respectively. Note that seventeen tensile tests were completed at room temperature, twelve tensile tests were completed at 165 °C, and twelve tensile tests were completed at 200 °C. The stress and strain scales are the same for the three graphs to help underscore changes in material response across temperatures. Although there is some scatter, a reasonable specimen-to-specimen correlation is shown in the stress-strain curves.

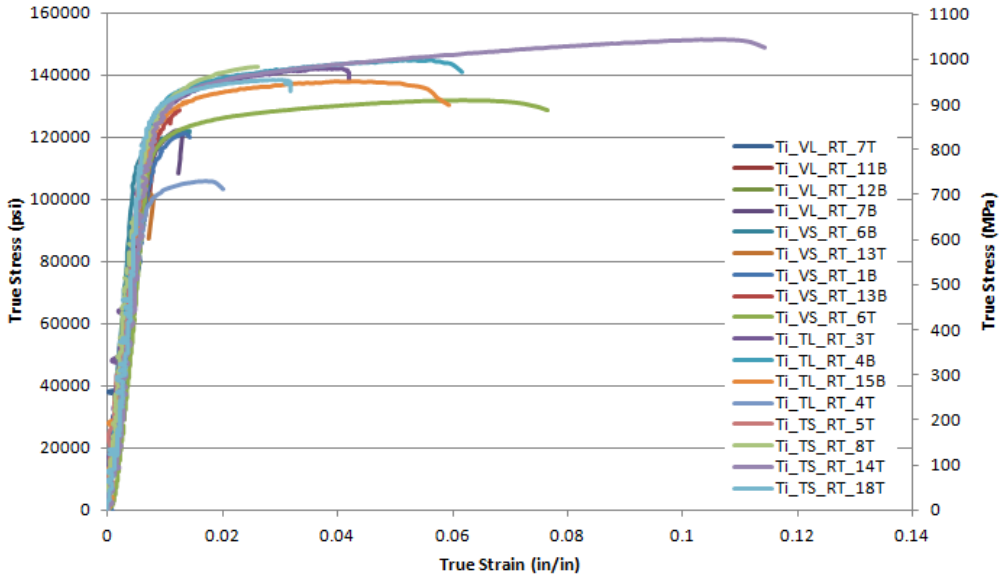

Figure 4.3: Stress-Strain Curves for Seventeen Ti-6-4 Tensile Tests at Room Temp

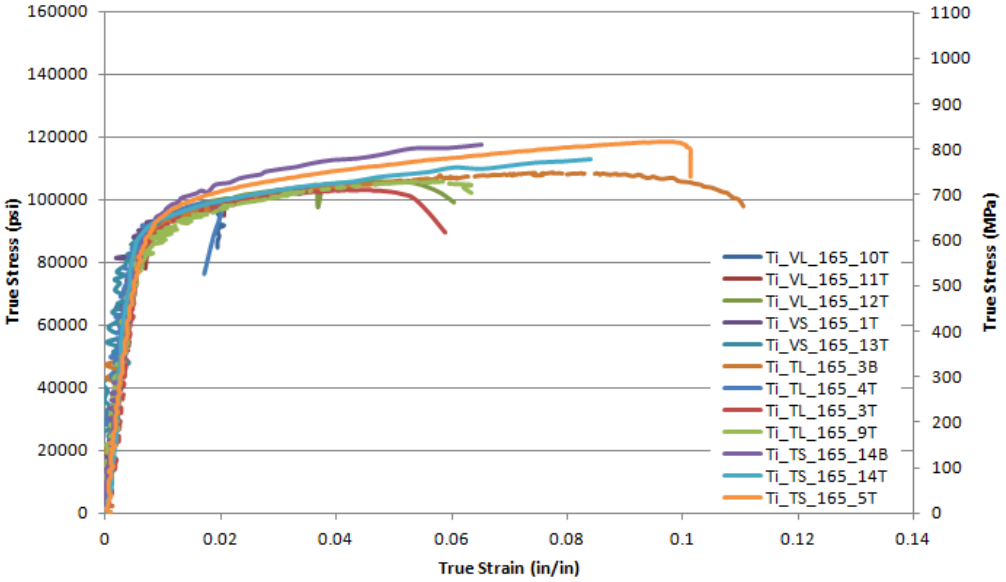

Figure 4.4: Stress-Strain Curves for Twelve Ti-6-4 Tensile Tests at 165 °C

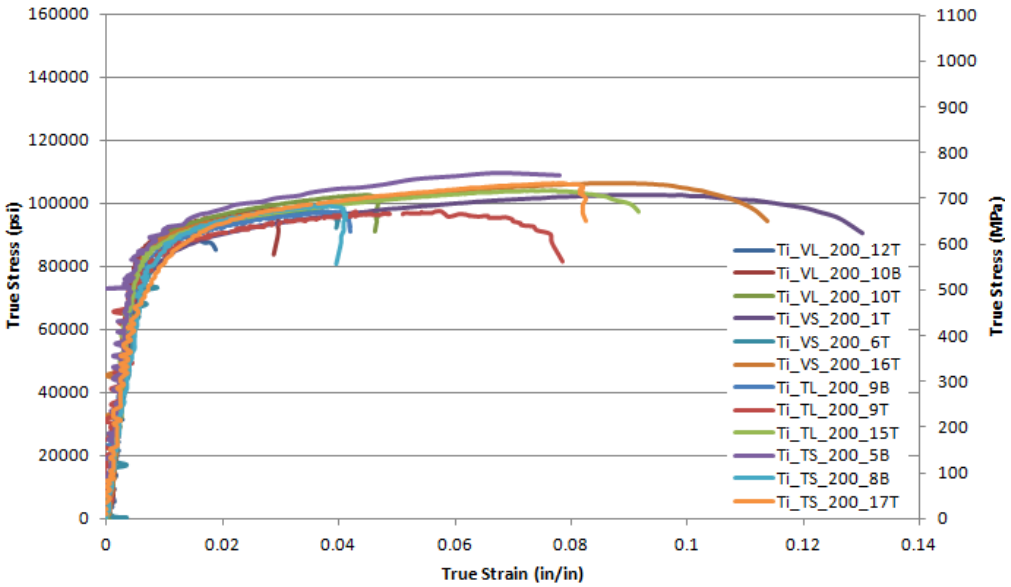

Figure 4.5: Stress-Strain Curves for Twelve Ti-6-4 Tensile Tests at 200 °C

Tensile test specimens failed in one of four modes and are shown in Figure 4.6 through Figure 4.9.

1) In the gage section where failure is intended

Figure 4.6: Tensile Failure in the Gage Section

2) Failure at a surface imperfection

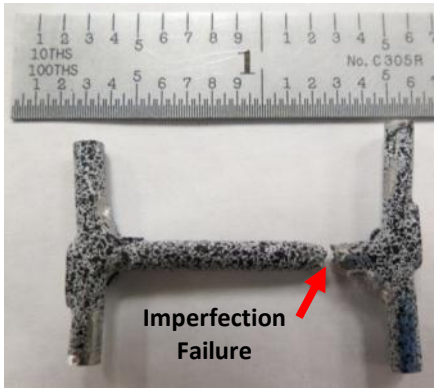

Figure 4.7: Tensile Failure at Surface Imperfection

3) A pullout failure in the grip

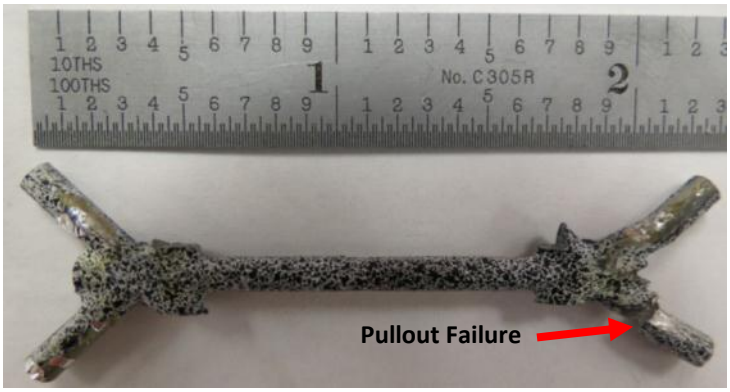

Figure 4.8: Tensile Failure by Pullout in the Grip

4) Failure at a node

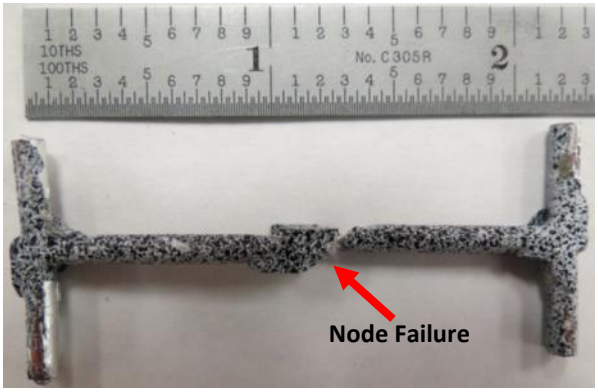

Figure 4.9: Tensile Failure at a Node

Bar charts are provided that show a comparison of the data generated in this project to data published commercially for Ti-6-4. The material properties of cast and HIPed Ti-6-4 are not readily available for elevated temperatures. Material property data at elevated temperature for annealed Ti-6-4 were utilized for comparison purposes. The annealed Ti-6-4 material properties were obtained from information provided by Allegheny Technologies, Incorporated (40). Cast and HIPed room temperature Ti-6-4 data was obtained from the Material Properties Handbook for titanium alloys (41). An assumption was made that cast and HIPed Ti-6-4 data will exhibit the same trends as annealed Ti-6-4 material data (i.e., a decrease in stiffness and strength with an increase in temperature). With commercial data available for annealed Ti-6-4 at room temperature, 165 °C, and 200 °C, a percent change was calculated for each material property listed (i.e., elastic modulus, yield strength, etc) between each temperature. These percent changes, along with the room temperature properties of cast and HIPed Ti-6-4, were used to establish cast and HIPed properties for 165 °C and 200 °C.

Figure 4.10 through Figure 4.15 show the tensile mechanical properties (i.e., elastic modulus, tensile yield strength, tensile ultimate strength, Poisson's ratio, percent elongation, and percent area reduction) for the Ti-6-4 test specimens. For each test temperature, data associated with the four test specimen orientations (TL, TS, VL, and VS) are presented first. The fifth bar in each group represents the estimated cast properties of commercially available Ti-6-4. The final bar in each group represents the averaged properties of the four specimen orientations. Note that while each bar chart ideally contains six bars of data at each test temperature, in some instances the data is

completely missing. The reason for the missing data, e.g., yield stress for test specimens designated Ti_VL at room temperature, is that the specimens failed in the grip. Failures in the grip do not produce information regarding material behavior beyond the elastic portion of the curve. The data from grip failures are not included in the yield stress, ultimate strength, elongation, or percent area reduction calculations.

The error bars in each figure visually quantify scatter present in the test data. The elastic modulus (Figure 4.10) values deviate from commercially available data by approximately 3.3% at room temperature up to approximately 7.3% at 200 °C. The panels tested for this project show lower yield stress (Figure 4.11) and ultimate strength (Figure 4.12) by as much as 15% and 10%, respectively, from the commercially available data. The expected trend of a decrease in modulus, yield stress, and ultimate strength with an increase in temperature is captured in the data. The Poisson's ratio (Figure 4.13) of the test specimens is within the expected range (red shaded region) of commercially available data. There is a great deal of scatter in the percent elongation (Figure 4.14) test data, and the data generally trends lower than the commercially available data. The percent area reduction (Figure 4.15) of the test specimens contains scatter due to the nonuniform and imperfect castings. However, the percent area reduction trends higher than the commercially available data. Note that specimen orientation does little to affect the cast material properties at any test temperature.

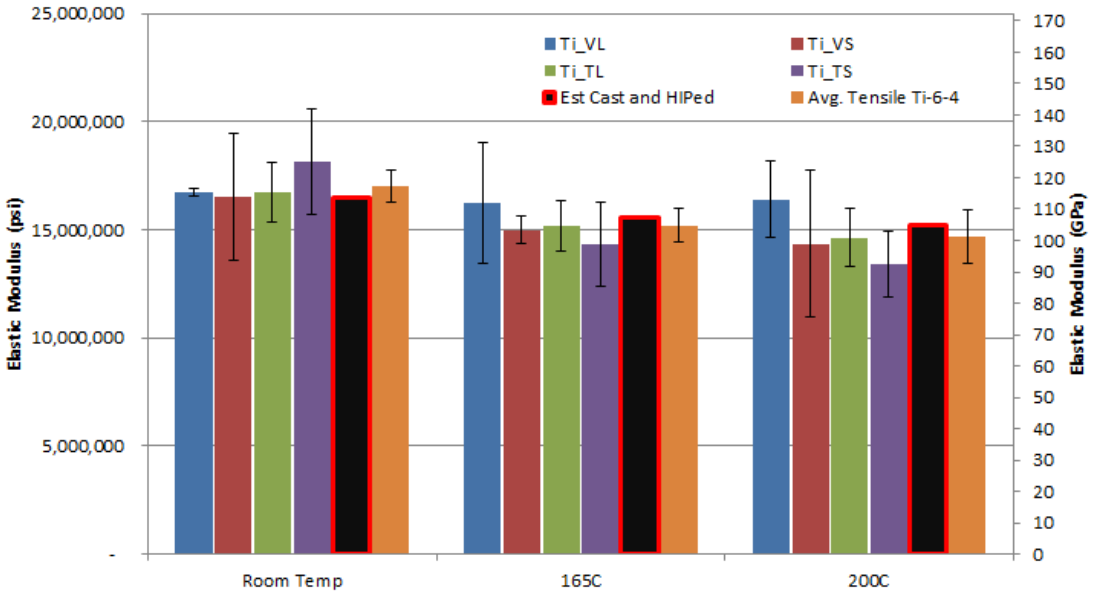

Figure 4.10: Ti-6-4 Tensile Elastic Modulus

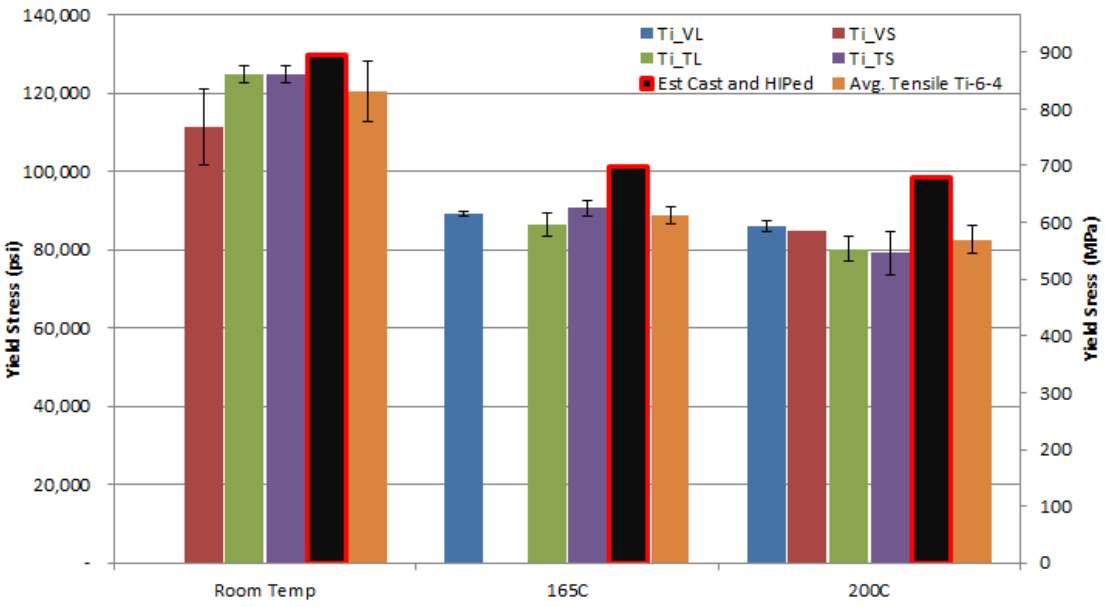

Figure 4.11: Ti-6-4 Tensile Yield Stress

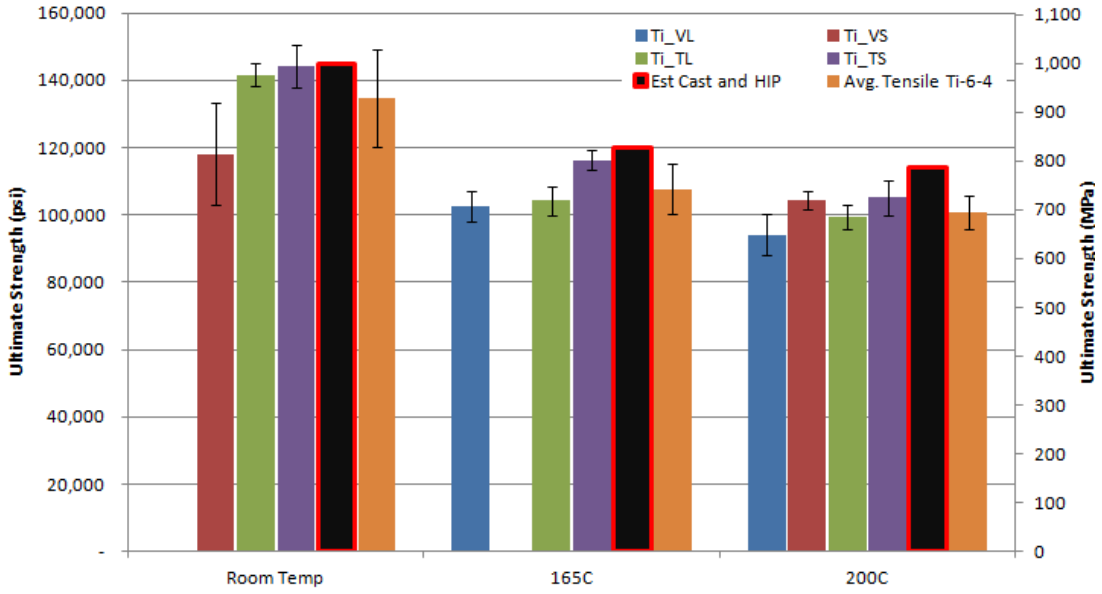

Figure 4.12: Ti-6-4 Tensile Ultimate Strength

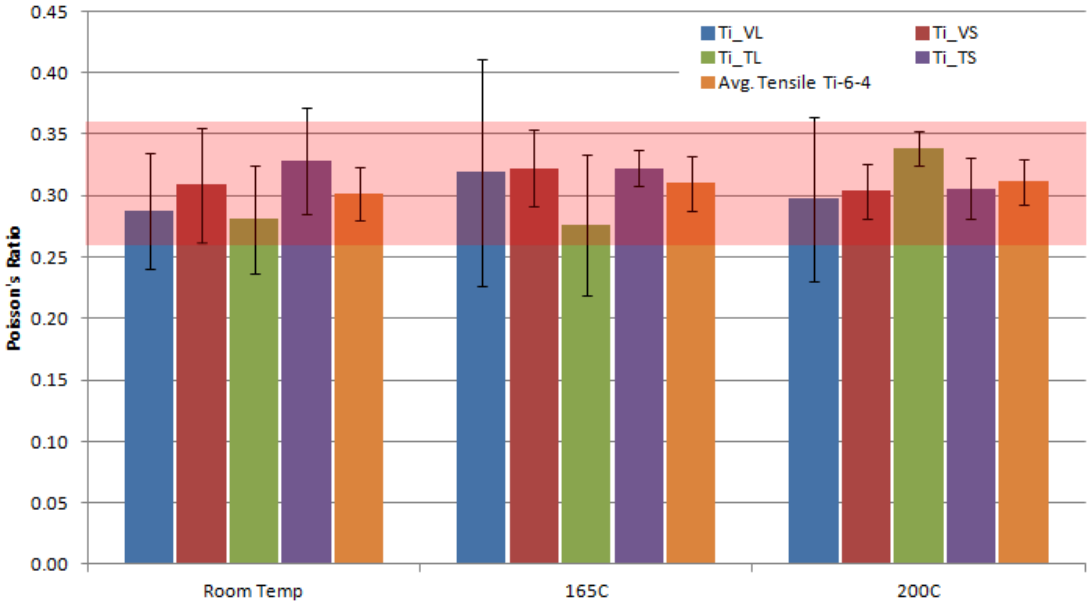

Figure 4.13: Ti-6-4 Tensile Poisson's Ratio

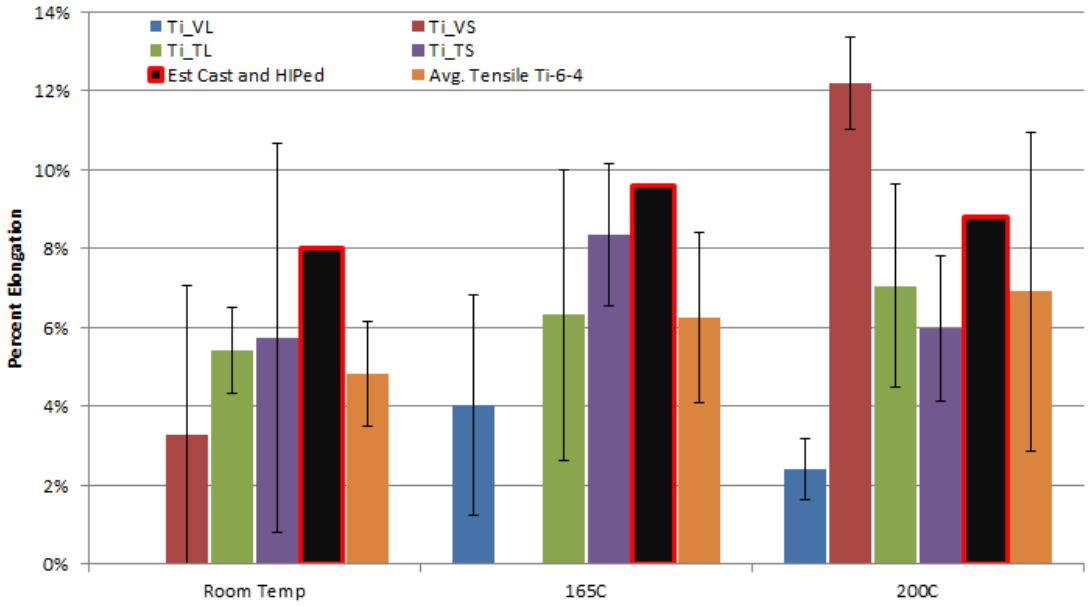

Figure 4.14: Ti-6-4 Tensile Percent Elongation

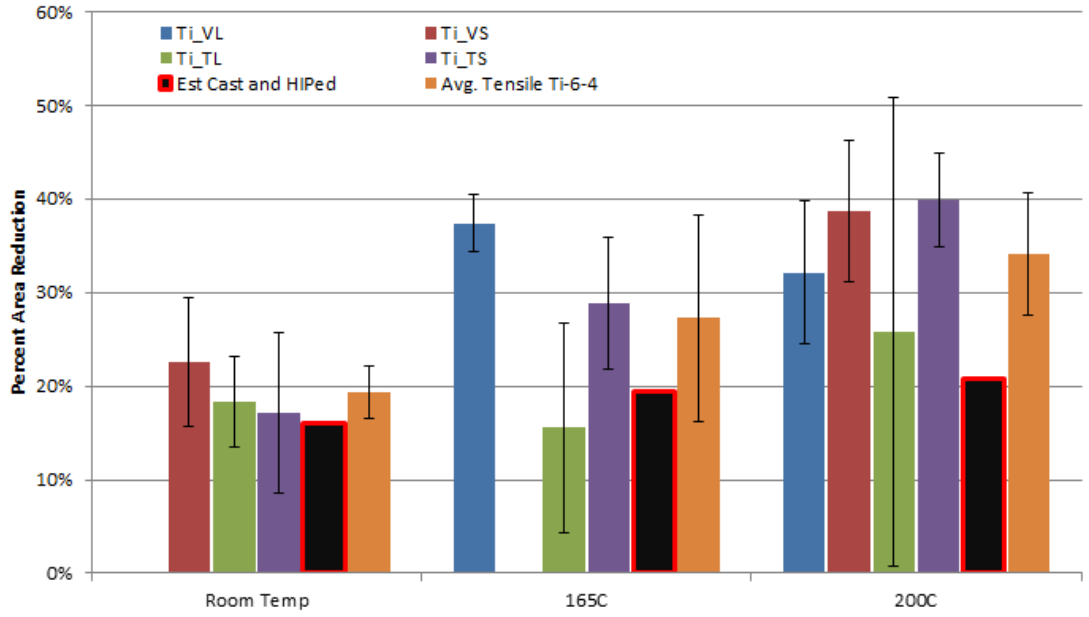

Figure 4.15: Ti-6-4 Tensile Percent Area Reduction

4.3 Ti-6-4 Compression Testing

Compression tests were conducted under displacement control at 0.0001 in/s and in load control at 20.5 lbf/s. Assuming a linear elastic response, prior knowledge of the Young's modulus of the material and the specimen geometry, these rates approximate a strain rate of 10^{-4} in/in/s. The rates for displacement and load control were used to verify that the control mode does not affect results. The crosshead displacement rate of the compression tests were an order of magnitude slower than the crosshead displacement rate of the tension tests in order to apply the same strain rate across all Ti-6-4 tests. Tests were conducted at room temperature, 165 °C, and 200 °C. The lattice block structure core contained no points of reference in order to label the locations of compression test specimens prior to machining. Having determined that there was no specimen orientation effects from tension testing, the compression specimens were randomly selected from the remaining lattice block structure inner core and tested.

Lubrication of the ends of compression specimens was an issue. Through friction, specimens become relatively fixed to the load platens during testing when no lubrication is provided. Compression tests should be conducted with pin-pin end conditions in order to use the Euler buckling formula in a straight forward manner. Without lubrication, a cylindrical test specimen is not allowed to expand radially, producing end conditions that are intermediate to pin-pin and fixed-fixed. This will invalidate the data. Compression tests were conducted with the ends of the test

specimens treated with boron nitride lubrication or alternatively with a graphite film. Tests conducted with both end conditions were monitored with optical extensometry in order to determine which lubrication procedure was superior. The test specimens treated with boron nitride showed no difference in results from a non-lubricated test. The graphite film was found to be difficult to apply to the specimens because of their small size. In addition, applying the graphite film on the specimens for high temperature tests proved more difficult because the circulating air in the furnace blew the graphite film off the specimens before a small preload could be applied to the specimens. After evaluating the comparative results it was decided that testing with no lubrication provided acceptable pin-pin end conditions.

The data from the compression tests was used to extract information relative to the elastic modulus, yield stress, and Poisson's ratio in a manner consistent with the tensile tests. Compression test data were first averaged by individual panel to determine if panel processing affects material properties. All data for a particular temperature range was then averaged.[10] The data from Table IV shows that, within acceptable scatter, there is no observable material property difference between the panels. In addition, control mode did not affect the results of the data.

[10] An expanded table of compression test data is provided in Appendix D

Table IV: Ti-6-4 Compression Average Test Results

Room Temp

	Tested Specimens	Modulus (psi)	Modulus (GPa)	Yield Stress (psi)	Yield Stress (MPa)	Poisson's Ratio
P13 Avg	5	14,615,648	100.77	-125,263.25	-863.88	0.335
P13 St. Dev		3,517,748	24.25	5,252.22	36.22	0.014
P13 CV		0.24	0.24	-0.04	-0.04	0.041
P6 Avg	3	16,444,947	113.38	-127,084.21	-876.44	0.311
P6 St. Dev		745,549	5.14	12,890.24	88.90	0.008
P6 CV		0.05	0.05	-0.10	-0.10	0.025
Average	8	16,404,047	113.10	-126,109.02	-869.72	0.331
St. Dev		606,657	4.18	7,084.04	48.86	0.018
CV		0.04	0.04	-0.06	-0.06	0.054

165 C

	Tested Specimens	Modulus (psi)	Modulus (GPa)	Yield Stress (psi)	Yield Stress (Mpa)	Poisson's Ratio
P13 Avg	3	15,630,877	107.77	-99,024.96	-682.93	0.342
P13 St. Dev		1,120,538	7.73	7,350.27	50.69	0.005
P13 CV		0.07	0.07	-0.07	-0.07	0.015
P6 Avg	2	13,160,680	90.74	-95,398.78	-657.92	0.334
P6 St. Dev		3,274,053	22.57	5,664.86	39.07	0.007
P6 CV		0.25	0.25	-0.06	-0.06	0.021
Average	5	15,850,384	109.28	-97,574.49	-672.93	0.339
St. Dev		929,718	6.41	6,243.45	43.06	0.007
CV		0.06	0.06	-0.06	-0.06	0.020

200 C

	Tested Specimens	Modulus (psi)	Modulus (GPa)	Yield Stress (psi)	Yield Stress (Mpa)	Poisson's Ratio
P13 Avg	3	12,720,292	87.70	-93,167.84	-642.54	0.350
P13 St. Dev		4,517,278	31.15	2,744.09	18.92	0.013
P13 CV		0.36	0.36	-0.03	-0.03	0.038
P6 Avg	2	12,322,981	84.96	-93,001.64	-641.39	0.324
P6 St. Dev		5,799,073	39.98	3,711.97	25.60	
P6 CV		0.47	0.47	-0.04	-0.04	
Average	5	12,561,368	86.61	-93,101.36	-642.08	0.343
St. Dev		4,319,441	29.78	2,686.63	18.53	0.017
CV		0.34	0.34	-0.03	-0.03	0.050

Compression specimens did not deform as expected. This is evident in Figure 4.16 where the axial compression surface strain is presented for a typical compression specimen. Compression specimens typically deformed with horizontal bands of localized strain. In Figure 4.16, the images are evenly spaced at different points through the test. The strain scale is the same for all images, and the load direction is vertical with the top of each image corresponding to the rigid side of the test frame. It is evident that compression strain is not uniform through the specimen at any point in the test. The top of the specimen is undergoing very little compressive strain during the test while the bottom of the specimen experiences over 25% axial strain at the end of the test. This banding of the compression strain suggests that the specimen is collapsing locally. If this occurs non uniformly around the specimen then a bending failure in the specimen at the local collapse initiates. An in-depth discussion on compression specimen bending is presented in the final chapter.

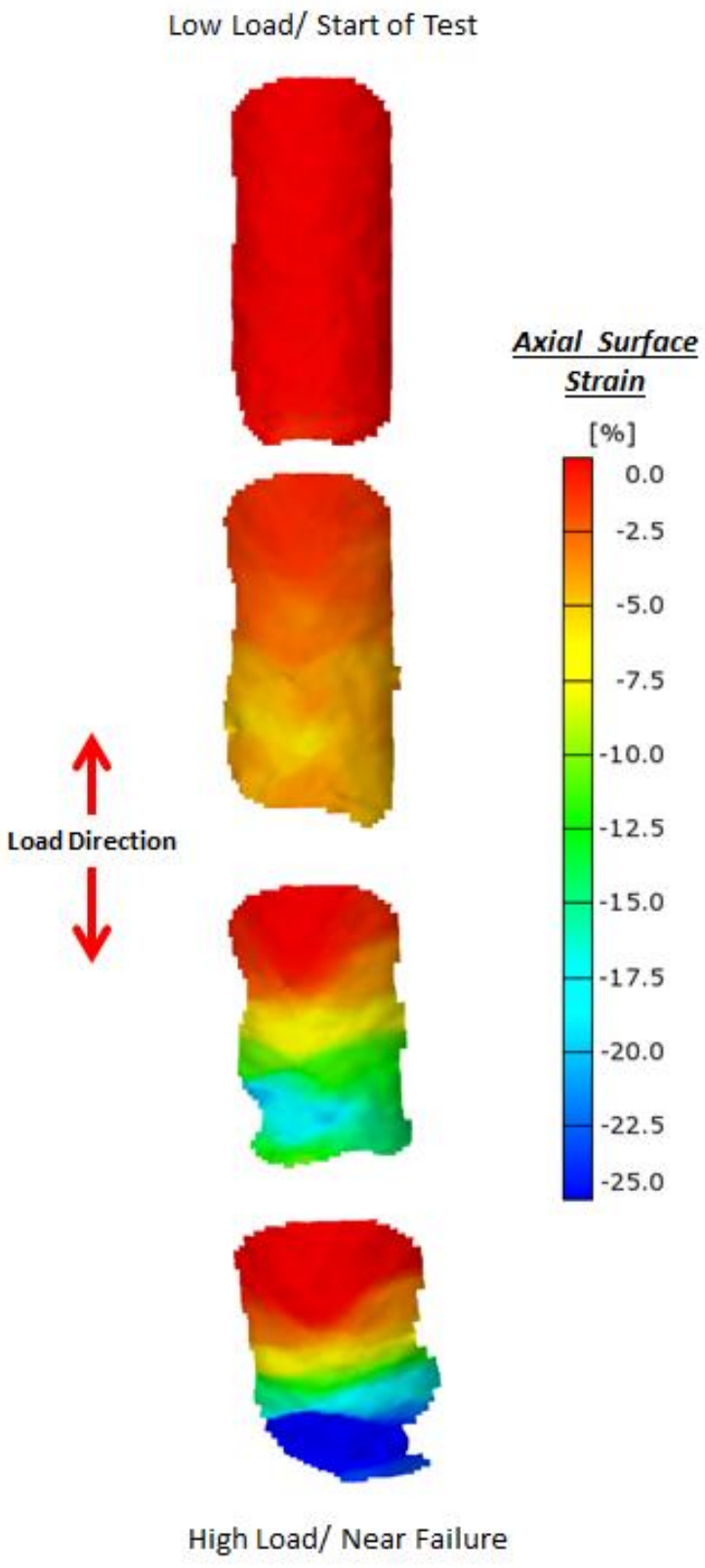

Figure 4.16: Axial Surface Strains for a Ti-6-4 Compression Specimen

Stress-strain curves for the compression tests are grouped by test temperature in Figure 4.17, Figure 4.18, and Figure 4.19. As with the tensile curves, the scales are the same across different test temperatures so material properties and their temperature dependence can be easily observed. Note that eight compression tests were completed at room temperature, five compression tests were completed at 165 °C, and five compression tests were completed at 200 °C. The curves depicted in these figures follow the general trends of commercial Ti-6-4 data. The final chapter will discuss possible causes for the scatter observed.

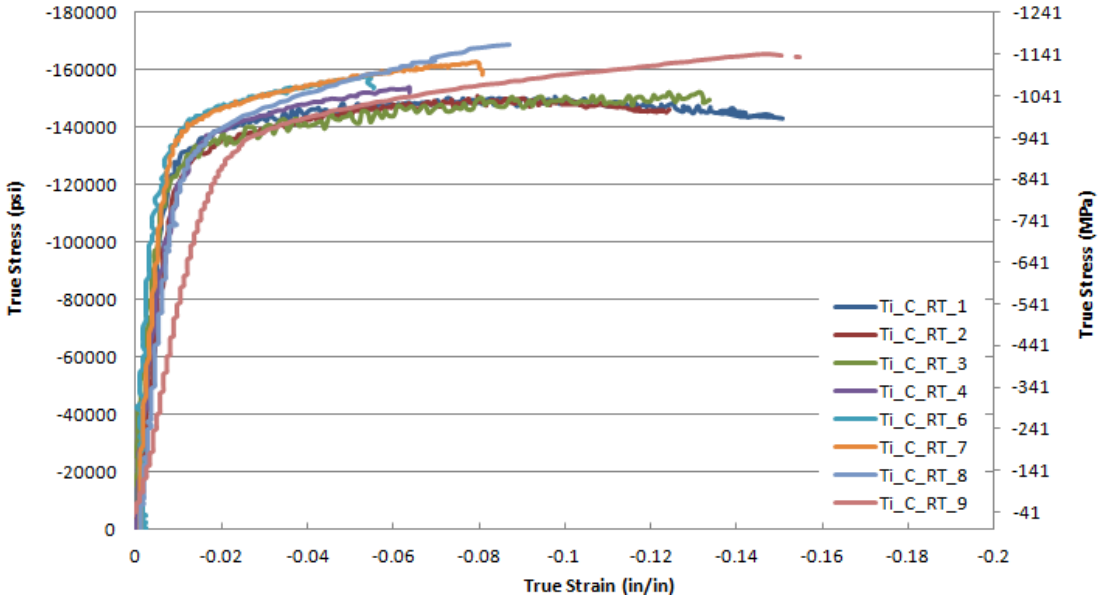

Figure 4.17: Stress-Strain Curves for Eight Ti-6-4 Compression Tests at Room Temp

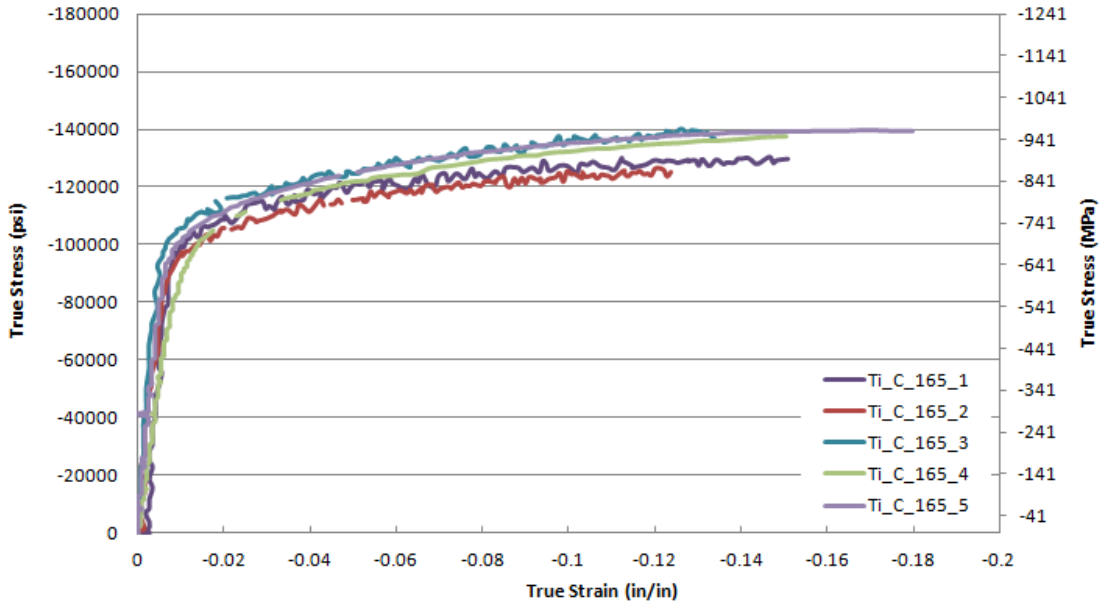

Figure 4.18: Stress-Strain Curves for Five Ti-6-4 Compression Tests at 165 °C

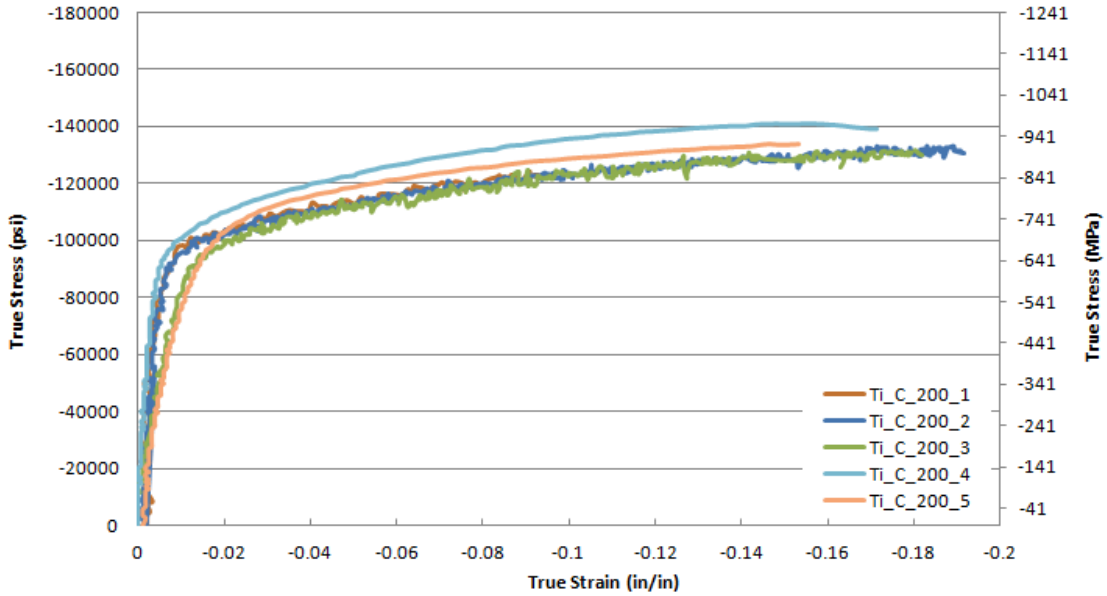

Figure 4.19: Stress-Strain Curves for Five Ti-6-4 Compression Tests at 200 °C

The Ti-6-4 specimens tested in compression deformed or failed in one of three modes: bending, shear, or displacement run-out. Specimens that bent during the test

typically bent at a stress level beyond the material yield stress. Shear failures resulted in the specimen undergoing a large displacement before splitting in half on an angle. A displacement run-out test is defined as a failure where no bending or shear occurred, but the specimen "barreled" in some instances. These tests were discontinued after a displacement level well past yield had been reached. Figure 4.20 contains four compression specimens. An untested specimen is on the far left, a bending failure second from left, a shear failure second from the right, and a displacement run-out specimen is on the right.

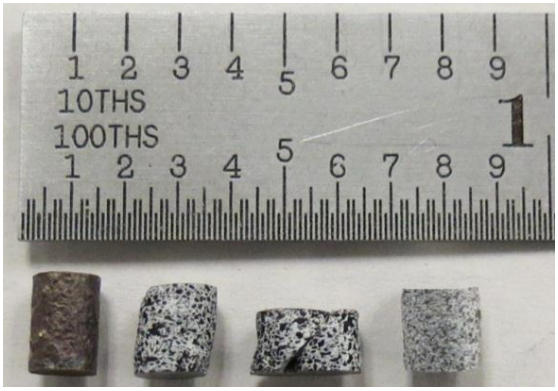

Figure 4.20: Failure Modes of Ti-6-4 Compression Specimens

Figure 4.21, Figure 4.22, and Figure 4.23 compare the compression test data with estimated cast Ti-6-4 material properties. As with the tensile comparison, compressive test data is compared against temperature interpolated test data for cast and HIPed Ti-6-4. Annealed Ti-6-4 material properties were obtained from an Allegheny Technologies, Incorporated technical data sheet (40) with cast and HIPed room temperature data provided by the Material Properties Handbook for titanium alloys (41).

The elastic modulus, shown in Figure 4.21, compares well to published data at room temperature and 165 °C with deviations from expected values of 0.58% and 1.94% respectively. The elastic modulus at 200 °C is considerably lower than published data because two specimens that skew the data (Appendix D.3). The yield stress, shown in Figure 4.22, compares reasonably well with published data. Deviations of 2.99%, 3.81%, and 5.50% for room temperature, 165 °C and 200 °C, respectively, are shown. The shaded region of Figure 4.23 indicates that the Poisson's ratio for the tested specimens falls within the expected values for Ti-6-4.

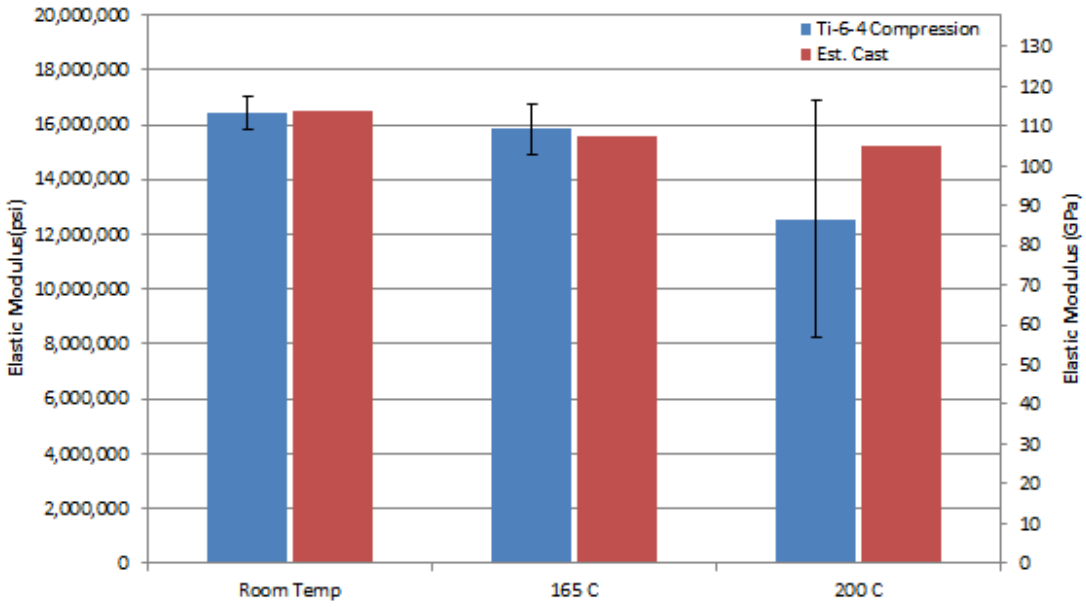

Figure 4.21: Ti-6-4 Compressive Elastic Modulus

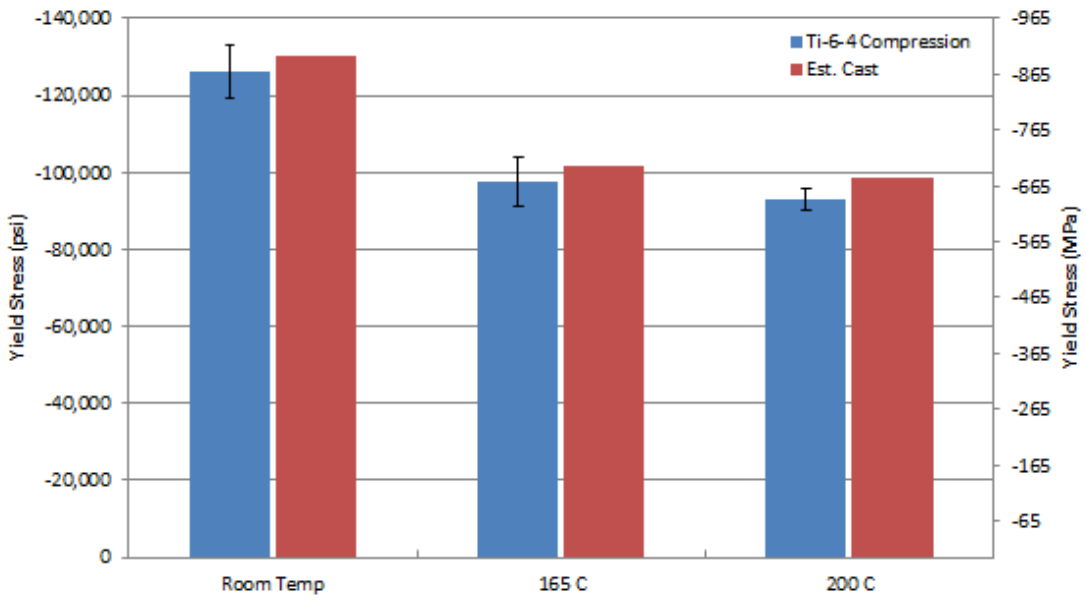

Figure 4.22: Ti-6-4 Compressive Yield Stress

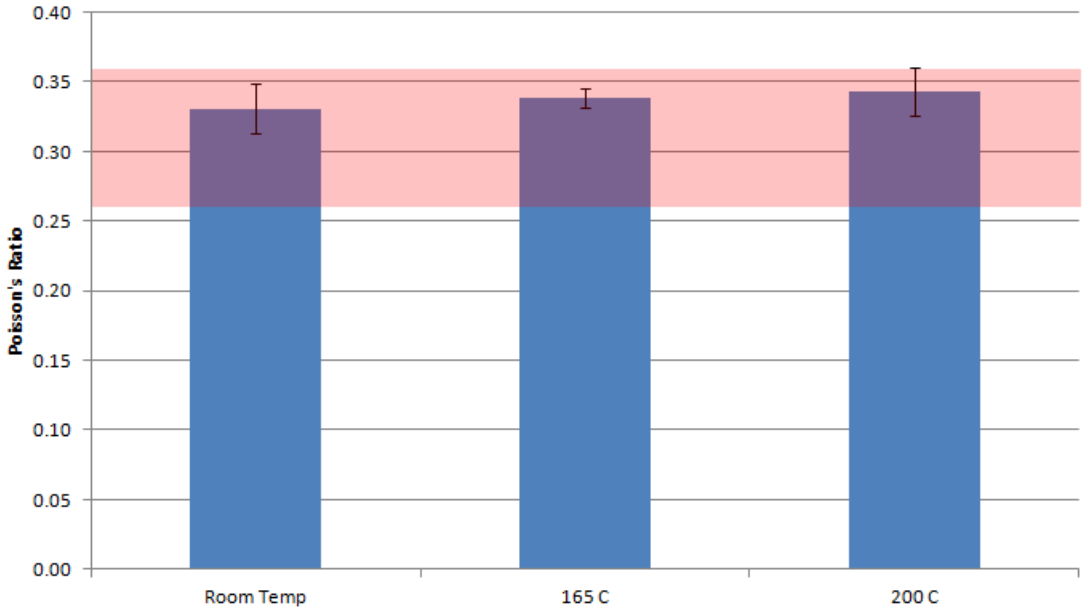

Figure 4.23: Ti-6-4 Compressive Poisson's Ratio

4.4 Comparisons of Ti-6-4 Using Tension and Compression Data

In this section, comparisons are made between the elastic modulus, yield stress, and Poisson's ratio across the tension and compression data. The expectation is that these values should be the same. Figure 4.24 through Figure 4.26 depict bar charts showing the values from tension and compression tests with error bars. The charts indicate that while the tensile properties do appear to be lower in most cases, the scatter in the data is large enough to conclude there is no difference between the information from either test regime.

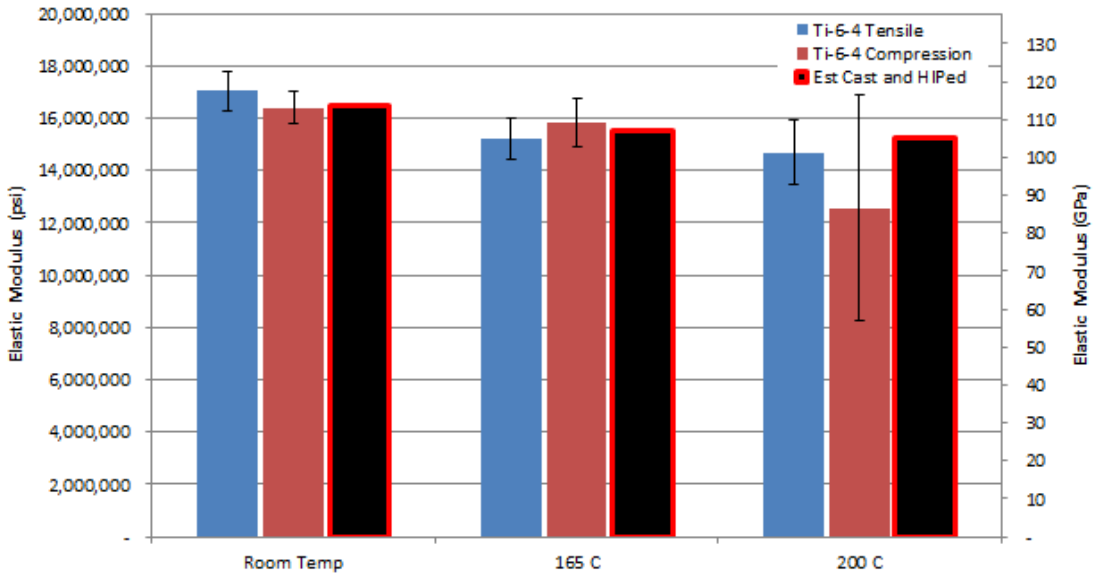

Figure 4.24: Comparison of the Elastic Modulus for Ti-6-4 Tension and Compression Tests

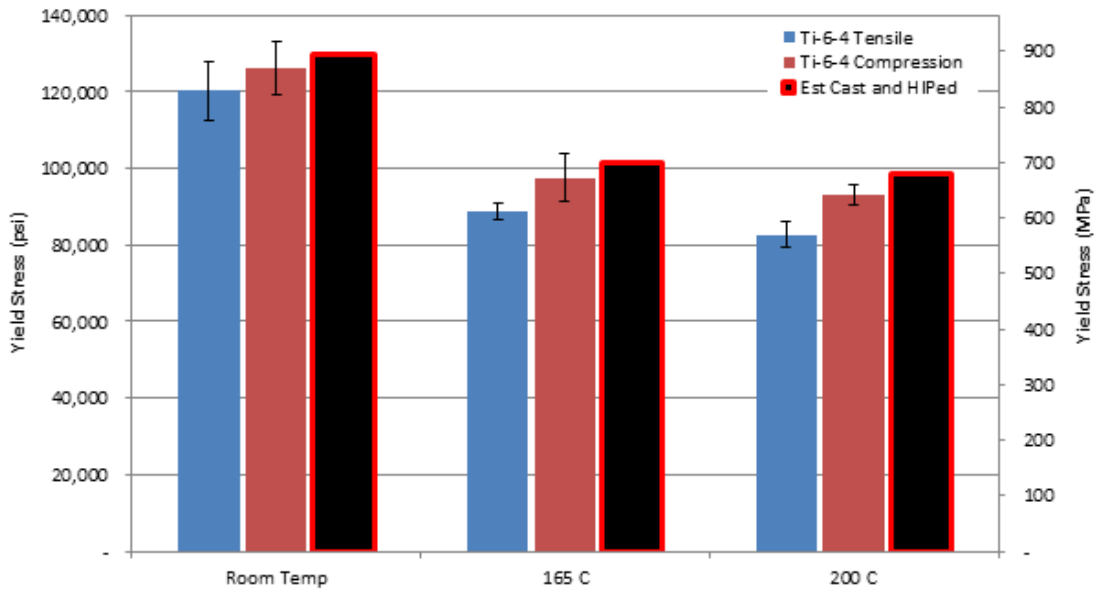

Figure 4.25: Comparison of the Yield Stress for Ti-6-4 Tension and Compression Tests

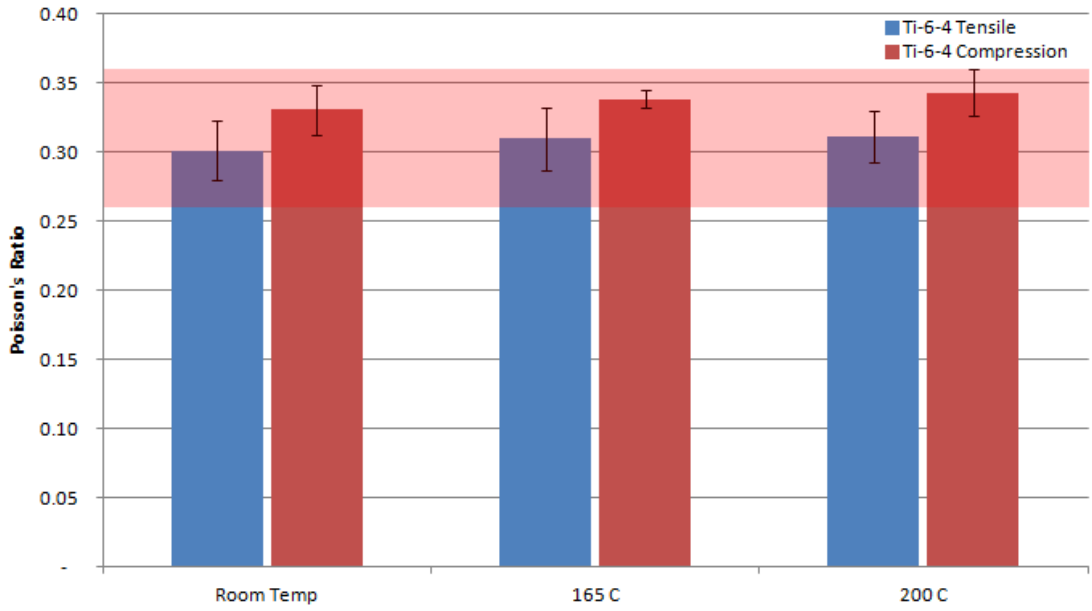

Figure 4.26: Comparison of the Poisson's Ratio for Ti-6-4 Tension and Compression Tests

4.5 Metallographic Evaluation of Ti-6-4

After mechanical testing was completed the test specimens were cut, mounted in resin, polished, and etched before being subjected to a metallographic evaluation. The specimens investigated included node specimens, end cross section views of the subelements, and horizontal cross sectional views of the subelements. These views are depicted in Figure 4.27a, b, and c, respectively. The grain size of the specimens were, on average, 0.2 inch (5.1 mm). Data published by Eylon and Newman in (42) indicates that expected grain sizes for cast and HIPed Ti-6-4 are 0.02 inch to 0.2 inch (0.51 mm to 5.1 mm). Node specimens contained 22-25 grains per cross section, subelement end cross sections contained 7-10 grains per cross section, and subelement horizontal cross sections contained 6-8 grains per cross section as viewed vertically in Figure 4.27c. With the grain sizes of specimens from this project falling into reasonable agreement with published data, the casting process used to make the Ti-6-4 lattice block structure did not produce material microstructures that adversely affected the test results. Some inclusions were present in the material that are most likely carbon deposits. Inclusions from the casting process are not considered uncommon. Figure 4.28a shows the typical microstructure of the Ti-6-4 specimens for this project and Figure 4.28b shows an example of an inclusion in the material.

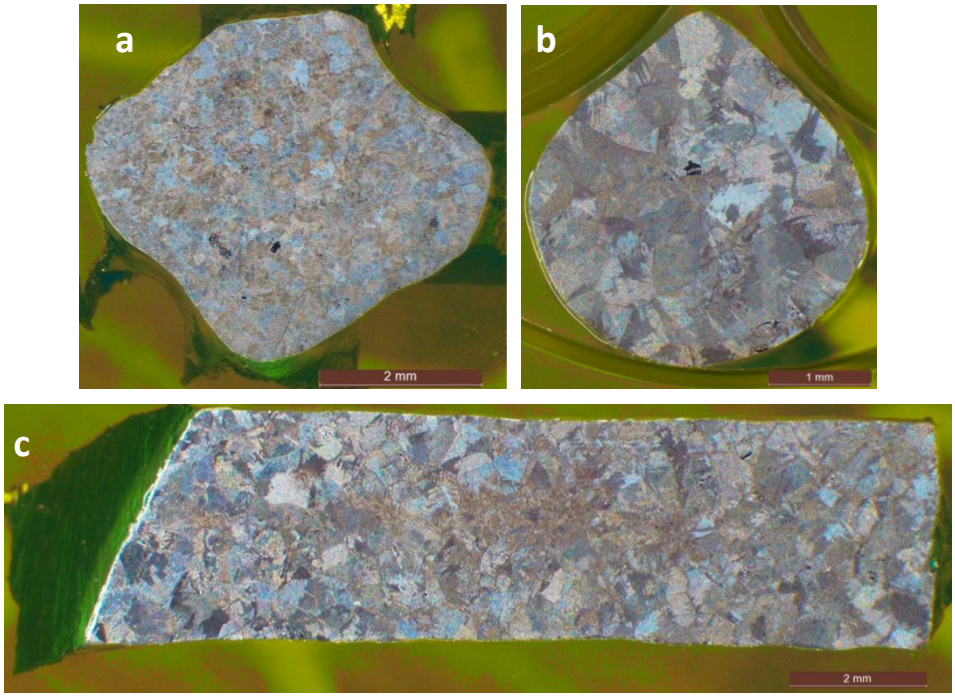

Figure 4.27: Ti-6-4 Etched Metallographic Specimens

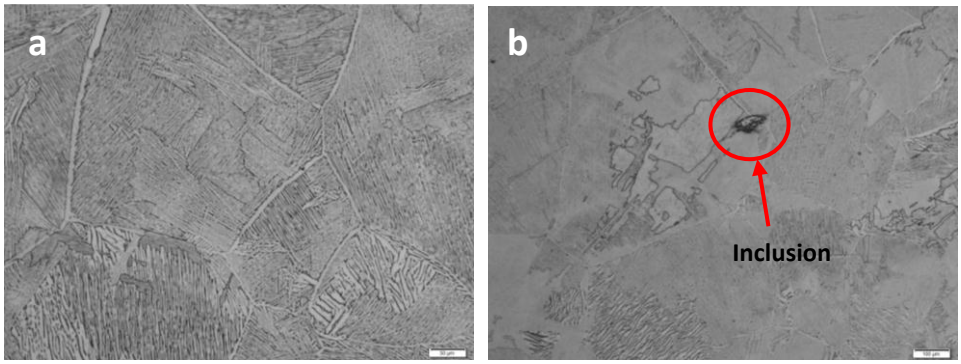

Figure 4.28: Typical Microstructure of Cast Ti-6-4 Specimens

It was first presumed that the ligaments and legs had somewhat circular cross sections. However, after preparing specimens for metallographic evaluation a number of the ligaments and legs exhibited a pronounced teardrop cross section (Figure 4.27b). All facesheet specimens exhibited a non-circular shape to a varying degree. The compression specimens removed from the inner core of the lattice block structure did

not show a teardrop shape but were commonly more elliptical than circular. Since panels from the lattice block structures tested in this effort were investment cast, the shape of the wax rapid prototype determines the shape of the casting and the result here is non-circular specimens.

Along with optical evaluation of the material, a chemical analysis[11] was performed on specimens from each test panel. The averaged values from the chemical analysis and values for annealed aerospace grade Ti-6-4 from an SAE[12] Aerospace Materials Specifications publication (43) are shown in Table V for comparison purposes. Material compositions were not found for cast and HIPed Ti-6-4 in order to make a comparison with those materials. The values from the test specimens fall within the tabulated value ranges found in the literature.

Table V: Ti-6-4 Chemical Analysis Results

Element	Average Test Specimen Weight Percent	ASM[13] Minimum Weight Percent	ASM Maximum Weight Percent
Al	6.50	5.50	6.75
V	3.92	3.50	4.50
Fe	0.085	Trace	0.3
O	0.169	Trace	0.2
C	0.008	Trace	0.08
N	0.005	Trace	0.05
Ti	Balance	Balance	Balance

[11] All chemical analysis performed by Dereck Johnson, NASA GRC
[12] Society of Automotive Engineers
[13] American Society for Metals

CHAPTER V

COMPARISION TESTING: NiTi SHAPE MEMORY ALLOY

5.1 Introduction

The results of the NiTi testing are presented in this chapter. The chapter begins with a description of the panel nomenclature followed by the nondestructive evaluation results. The problems encountered during testing are described as well as the results from mechanical testing on the NiTi specimens. The chapter concludes with results from the metallographic and chemical evaluation.

Transition 45 Incorporated cast four NiTi lattice block panels with one panel available for subelement tension and compression testing. The other three panels were utilized in full-scale compression tests that are not reported on here. The panel acquired for this subelement testing was used for validation of the test frame, tension and compression testing, chemical analysis, and for destructive metallographic analysis

after testing was complete. Table VI gives information for the panel used for this testing.

Table VI: NiTi Lattice Block Structure Panel Designation

Panel	Manufacturer Serial Number	Nominal Size (in)	Final Processing	Use
1	Heat 1131 S/N 2-2 NiTi	3x3	Abrasive Blasted	Test Frame Validation Tension/ Compression Specimens Metallographic Evaluation Chemical Evaluation

The four NiTi panels are representative of the first NiTi lattice block panels fabricated using investment casting. Investment cast Ti-6-4 panels were highly flawed when they were first introduced. The casting process has improved to where Ti-6-4 panels are now manufactured in a relatively defect free state. There is every reason to believe that a similar trend will hold for NiTi lattice block structures.

One could easily discern that the NiTi lattice block structure panel tested was in poor condition after a simple visual inspection. However, it should be noted that there were good surface fill throughout the panel with no HIP sinks or open pores on the surface. The most significant defect were multiple cracks at the nodes (Figure 5.1). There are three mechanisms that promote cracking. First, significant stress develops as the material cools and contracts in the casting. Second, voids found at the node reduce the cross sectional area of the node and lead to higher stresses. Voids at nodes located

in the lattice block structure quickly became evident when the facesheets were removed (Figure 5.2). The voids were most likely caused by an insufficient number of risers feeding melt to the casting such that the mold was not properly filled as the molten material cooled (27). Cracks emanating from the void are clearly visible in Figure 5.2. Third, the panel material was found to be very brittle. Equiatomic NiTi is known for being able to elongate several percent strain and then recover. However, specimens cut from the panel easily snapped in half by hand. A metallographic and chemical analysis (discussed later) revealed a deleterious material phase that gave rise to this the brittle behavior. The panel manufacturer was aware of these defects and were adjusting their casting technique when the panels were delivered. Because of time constraints placed on the NASA SBIR project, the flawed panels were delivered while the manufacturer continued to improve their casting process. Due to the time constraints, defect maps were not provided.

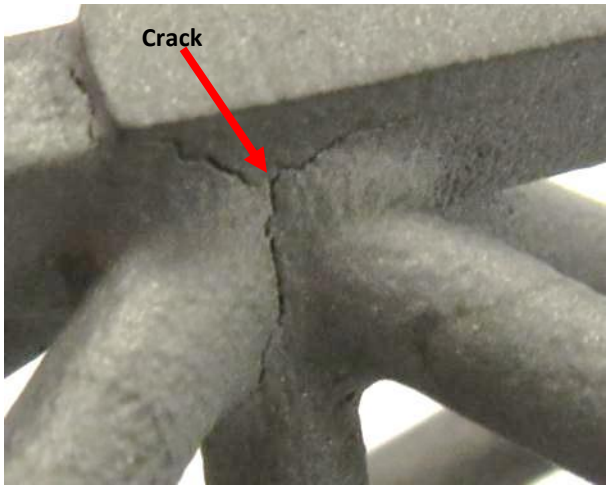

Figure 5.1: Typical NiTi Lattice Block Structure node cracks

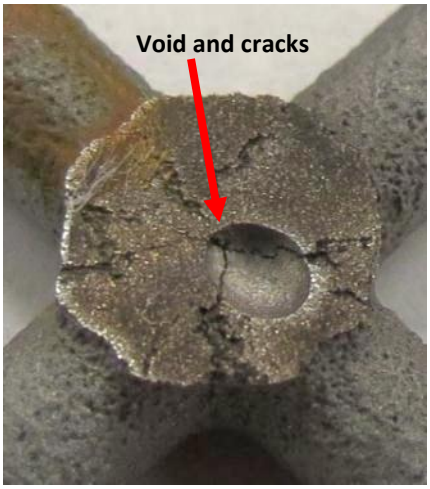

Figure 5.2: Internal void and cracks at node

5.2 NiTi Tensile Tests

Tensile testing was hampered by the brittleness of the material. Only six tensile specimens could be cut from the one available panel. As specimens were being cut from the panel using EDM one specimen broke. Another specimen snapped in half during the sample preparation process. A third sample crumbled in the test fixture at low load. For these reasons, quality tensile data associated with the NiTi panels cannot be reported on here.

5.3 NiTi Compression Tests

Compression tests were conducted on the brittle specimens. After the tensile tests failed to produce data, expectations moderated and the intent for the

compression tests was to exercise the test protocols in a proof of concept exercise for future efforts when higher quality NiTi castings are available. Several compression tests were completed at room temperature, 165 °C, and 200 °C under load control. A load rate of 7.5 lbf/s was chose to approximate a strain rate of 10^{-4} in/in/s in the elastic region of the NiTi material. All specimens were tested without end lubrication for the reasons described in the Ti-6-4 compression testing. Before conducting a compression test, all specimens were heated in an oven at 428 °F (220 °C) for 15 minutes, allowed to cool to room temperature, and heated to 428 °F for another 15 minutes to relieve internal stresses.

Figure 5.3 is a generic representation of a NiTi stress-strain curve when the material is below the austenite finish temperature. For NiTi compression testing below the austenite finish temperature, material properties of interest include what is referred to in the literature as the "apparent" elastic modulus, the stress at the onset of reorientation/ detwinning, and the stress when reorientation/ detwinning is complete. The apparent elastic modulus value is calculated by a trendline fit to the lower linear portion of the curve before the onset of the material reorientation. The stress at the onset of reorientation and detwinning (σ_{rs} in Figure 5.3) is the stress value at the intersection of the apparent elastic modulus trendline and a trendline corresponding to the portion of the stress-strain curve where the reorientation is occurring. Finally, the stress at the finish of the reorientation and detwinning (σ_{rf} in Figure 5.3) is the stress value where the aforementioned sloped line intersects a trendline corresponding to the stress-strain curve after reorientation is complete. The material region identified as

"complex" is not well understood and an explanation of the material behavior in this region is beyond the scope of this project.

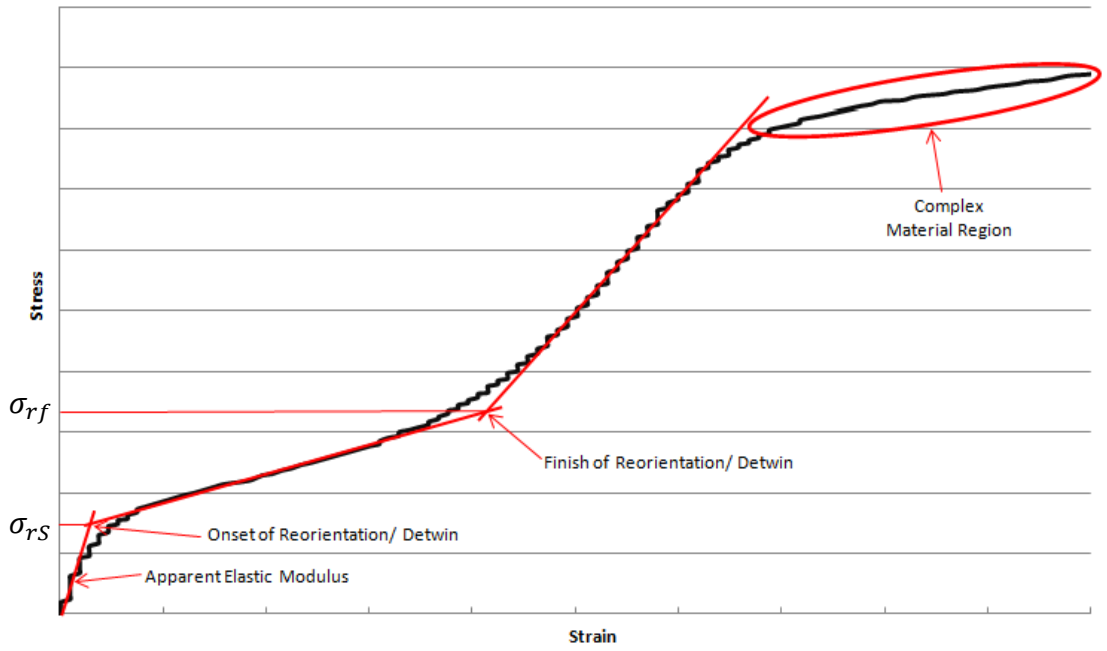

Figure 5.3: Generic NiTi Compression Stress-Strain Curve Below the Austenite Finish Temperature

Figure 5.4 is a generic representation of a compression stress-strain curve for NiTi when testing is conducted above the austenite finish temperature of the material. Properties obtained from this graph include the apparent elastic modulus and the onset of material reorientation/ detwinning stress. The apparent elastic modulus is obtained from a trendline fit to the lower linear portion of the stress-strain curve. The stress at the onset of material reorientation (σ_{rs} in Figure 5.4) is obtained as the stress value at the intersection of a 0.2% offset trendline to the apparent modulus and the test data.

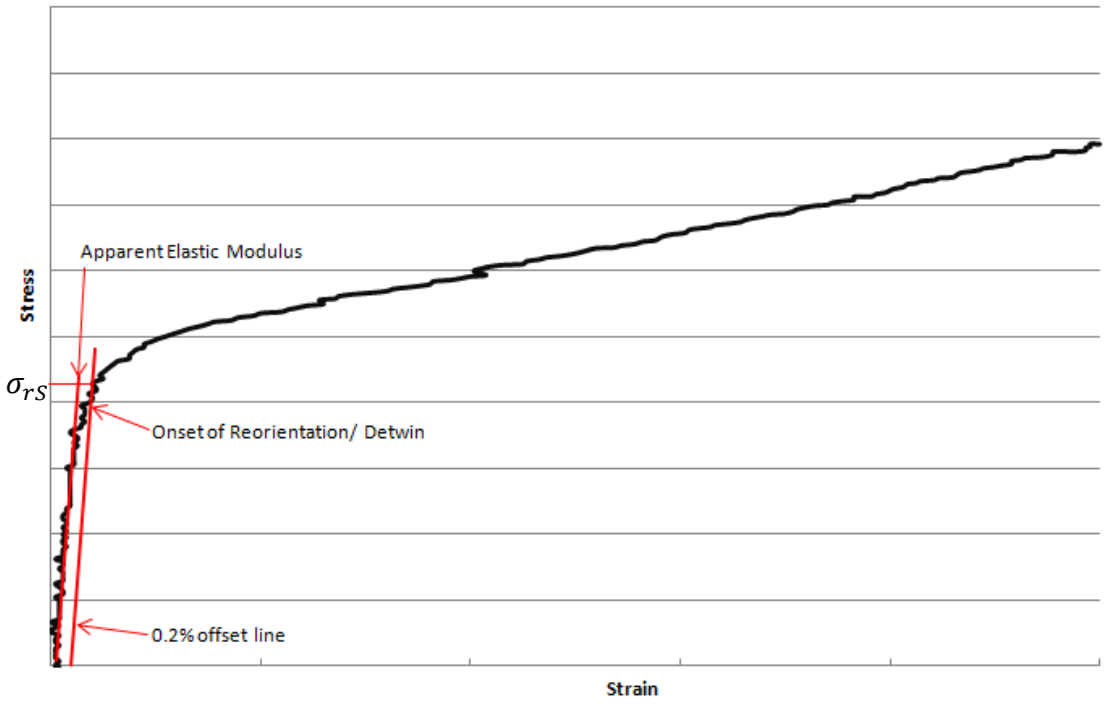

Figure 5.4: Generic NiTi Compression Stress-Strain Curve Above the Austenite Finish Temperature

Figure 5.5 represents the axial surface strain for a typical NiTi compression specimen at various stages of the test. The axial surface strain on a typical NiTi specimen at the end of the test ranges from 18%-25%. This trend is consistent with all of the NiTi specimens tested here. In comparison, the surface strain on a typical Ti-6-4 compression specimen (Figure 4.16) ranges between 0%-25% at the end of the test. NiTi compression specimens have a much smoother surface finish and a more consistently circular cross section compared to the Ti-6-4 specimens, which can explain the tighter range of surface strains for NiTi.

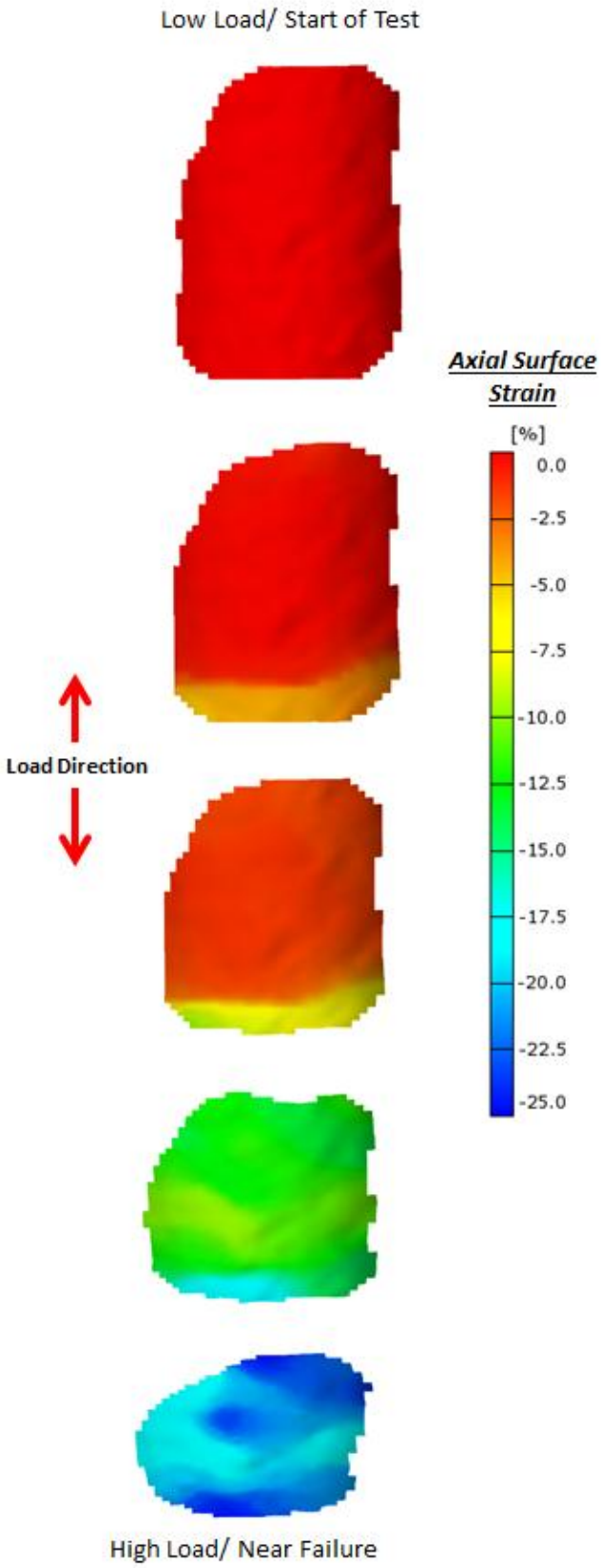

Figure 5.5: Axial Surface Strains for a Typical NiTi Compression Specimen

The data from NiTi compression tests contained scatter which is evident in the stress-strain curves depicted in Figure 5.6 through Figure 5.8. All of the data provided here are based on "true" values computed using equations 4.1 and 4.2. Note that the stress and strain scales are the same in each figure to allow for a visual comparison across the three test temperatures. Compression specimens with stress-strain curves completely to the right (i.e., a higher strain value for every stress value compared to other specimens) is an indication of the compression specimens bending early in the test. Here, five compression tests were completed at room temperature, four compression tests were completed at 165 °C, and five compression tests were completed at 200 °C.

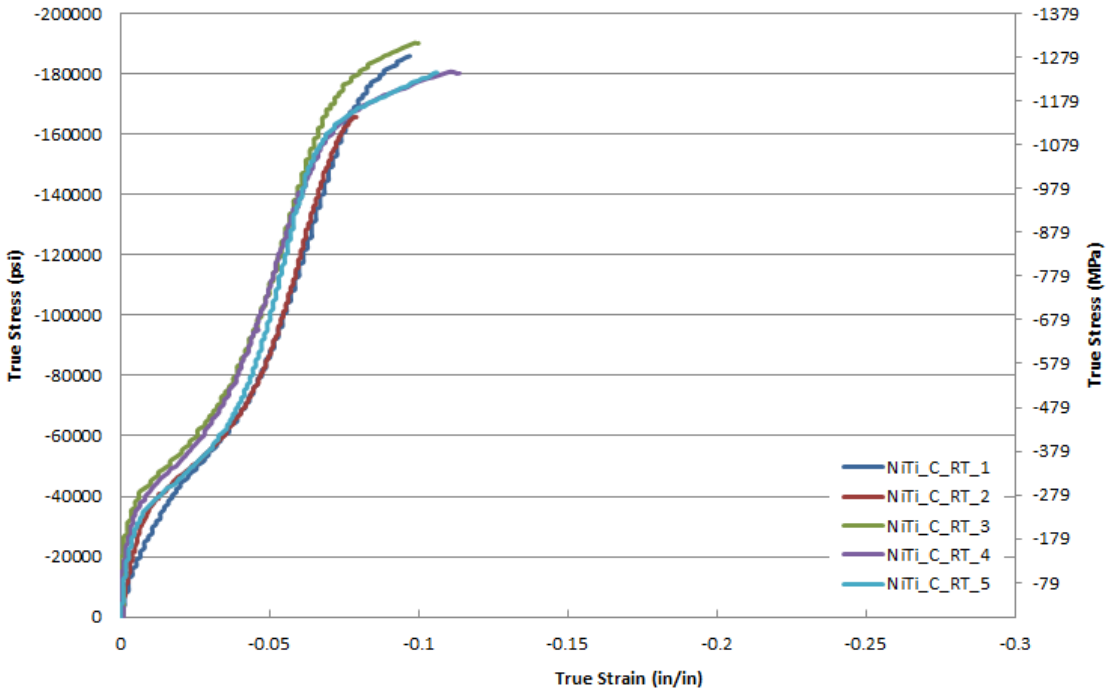

Figure 5.6: Stress-Strain Curves for Five NiTi Compression Tests at Room Temperature

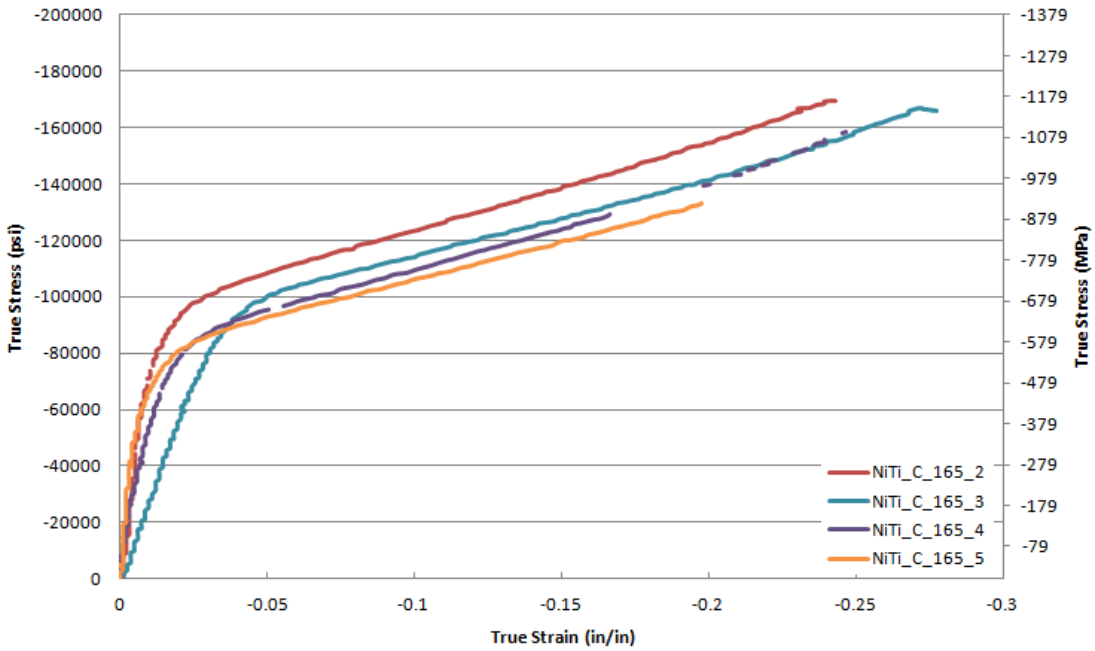

Figure 5.7: Stress-Strain Curves for Four NiTi Compression Tests at 165 °C

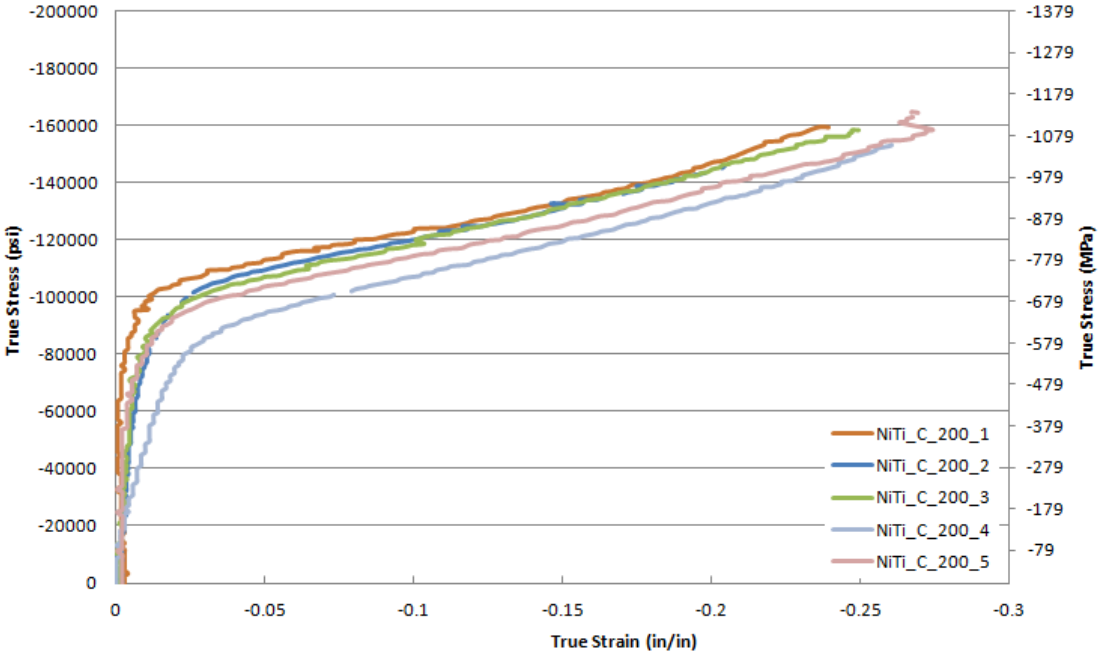

Figure 5.8: Stress-Strain Curves for Five NiTi Compression Tests at 200 °C

There is a substantial amount of tensile data available for equiatomic NiTi but very little for compression, and elevated temperature data is nearly nonexistent. NiTi does not have the same material properties in tension and compression, as a conventional material (i.e., Ti-6-4) does. Averaged mechanical properties for room temperature, 165 °C, and 200 °C were calculated and the results are tabulated in Table VII.[14] Compression test data completed previously by other researchers at NASA Glenn on extruded equiatomic NiTi at room temperature were obtained (44). This data contained complete numeric data sets at room temperature that were evaluated and compared with test data gathered during this project. The comparison is shown in Figure 5.9. The red curves (well-machined extruded specimens) from previous NASA testing show three room temperature NiTi compression tests that are virtually identical with no observable scatter. The grey curves (as-cast specimens) are room temperature NiTi compression tests from this testing effort with a large amount of scatter. This figure illustrates the repeatability of well-machined versus as-cast specimens.

[14] An expanded table of NiTi compression data is provided in Appendix D.4

Table VII: Averaged Mechanical Properties from Current NiTi Compression Tests

Room Temp

Current Test Data	Poisson's Ratio	Apparent Modulus (psi)	Apparent Modulus (Gpa)	Reorientation Start (psi)	Reorientation Start (Mpa)	Reorientation Finish (psi)	Reorientation Finish (Mpa)
Average	0.350	4,068,444	28.05	-36,127.75	-249.16	-68,900.15	-475.17
St. Dev	0.030	974,209	6.72	3,370.85	23.25	2,844.20	19.62
CV	0.085	0.24	0.24	-0.09	-0.09	-0.04	-0.04

165 C

	Poisson's Ratio	Apparent Modulus (psi)	Apparent Modulus (Gpa)	Reorientation Start (psi)	Reorientation Start (Mpa)
Average	0.351	7,398,283	51.01	-68,747.78	-474.12
St. Dev	0.099	3,700,748	25.52	10,258.76	70.75
CV	0.280	0.50	0.50	-0.15	-0.15

200 C

	Poisson's Ratio	Apparent Modulus (psi)	Apparent Modulus (Gpa)	Reorientation Start (psi)	Reorientation Start (Mpa)
Average	0.346	7,102,390	48.97	-81,787.56	-564.05
St. Dev	0.086	3,155,391	21.76	9,179.92	63.31
CV	0.248	0.44	0.44	-0.11	-0.11

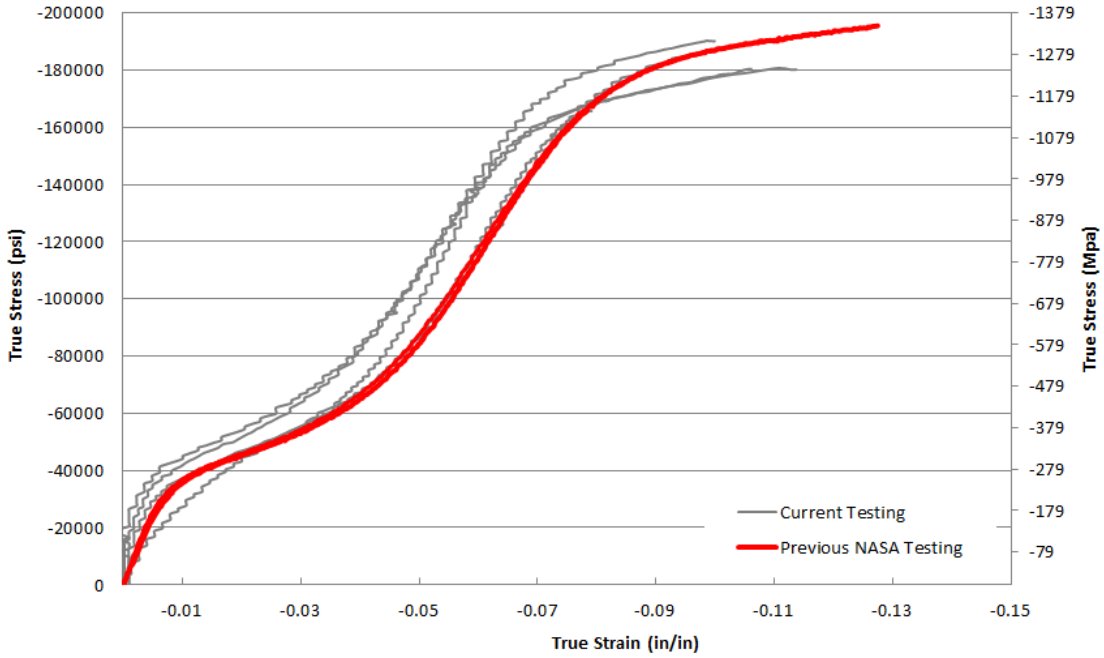

Figure 5.9: Room Temperature Stress-Strain Curves for Current and Previous NASA NiTi Compression Tests

The NiTi compression specimens failed in one of two modes, i.e., bending or barreling. Figure 5.10 illustrates an undeformed specimen on the left, a bent specimen

in the middle, and a barrel failure on the right. Bending failures were very common and as explained in the previous chapter, are most are likely because of the non-uniform material surface.

Figure 5.10: Failure Modes of NiTi Compression Specimens

Bar charts shown in Figure 5.11 through Figure 5.14 provide a comparison of current room temperature test data for the as-cast NiTi in this project with previous room temperature data for extruded equiatomic NiTi compression specimens. In addition, these figures provide error bars for mechanical properties at room temperature and elevated temperature. For room temperature, the bar charts indicate that the apparent elastic modulus from test specimens in this project is approximately 22% lower than the modulus from the extruded material. The discrepancy can be attributed to the scatter in the data as indicated by the error bars on the chart. The reorientation stresses from the project test data are consistently higher than the extruded data with start and finish stresses 3.5% and 12% higher on average, respectively. Note that the apparent reorientation finish stress chart only reports room temperature data. As a reminder, this is because the apparent reorientation finish

stress is only applicable below the material's austenite finish temperature. The Poisson's ratio is consistent between all temperature ranges of current testing with no data available from the previous NASA testing for comparison. No elevated temperature data was available for comparison to the current test data.

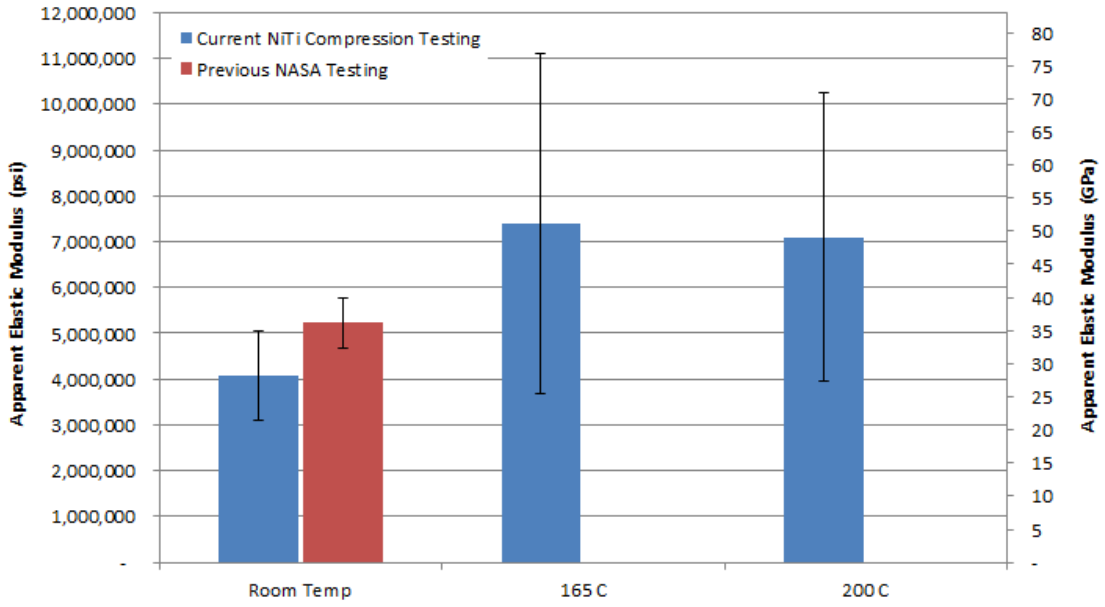

Figure 5.11: NiTi Compressive Apparent Elastic Modulus

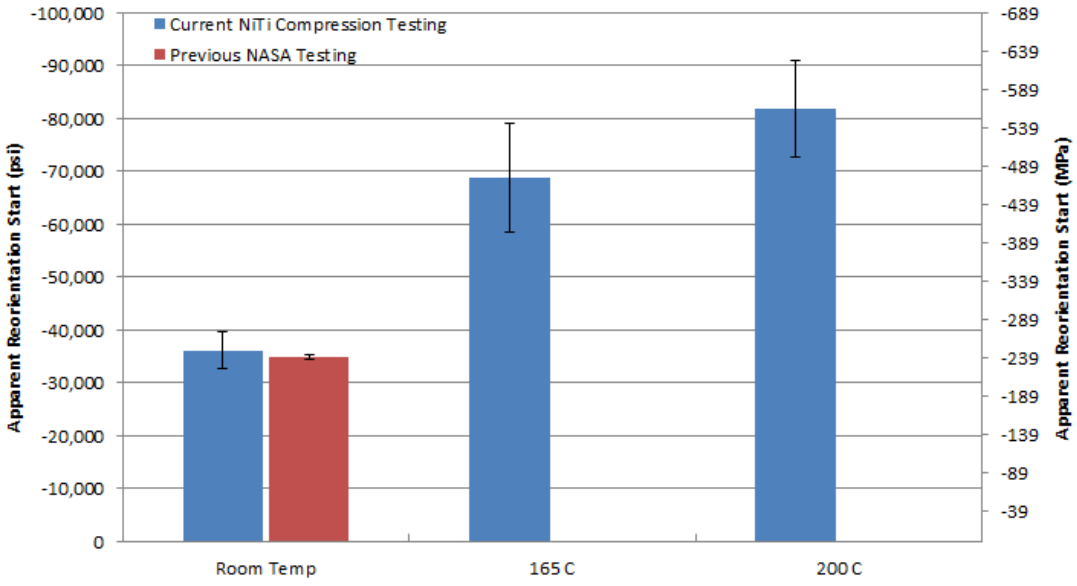

Figure 5.12: NiTi Compressive Apparent Reorientation Start Stress

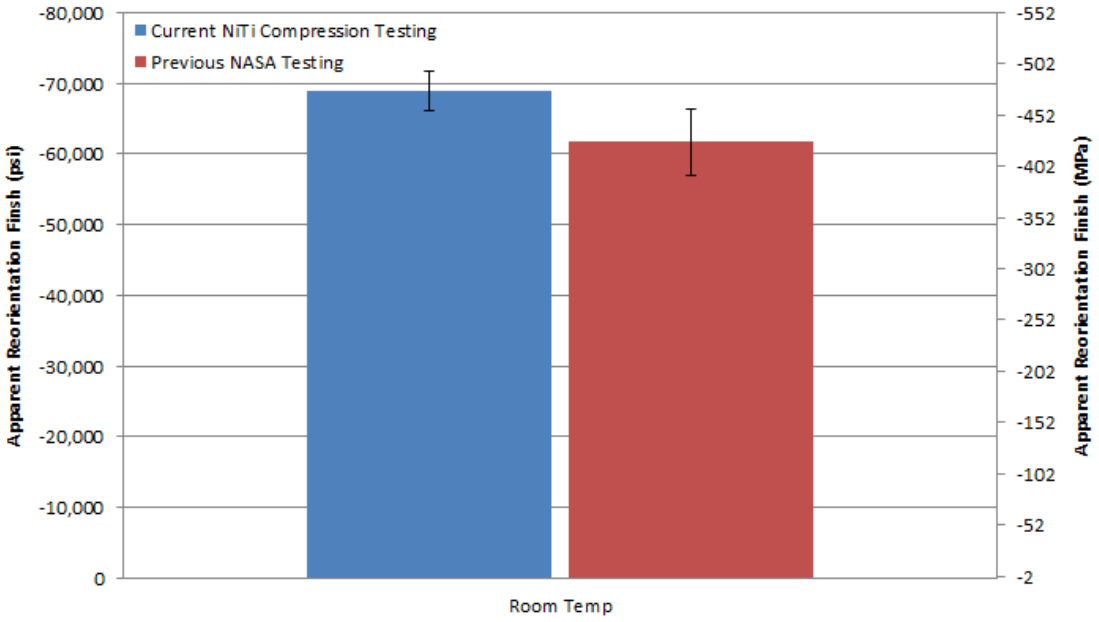

Figure 5.13: NiTi Compressive Apparent Reorientation Finish Stress

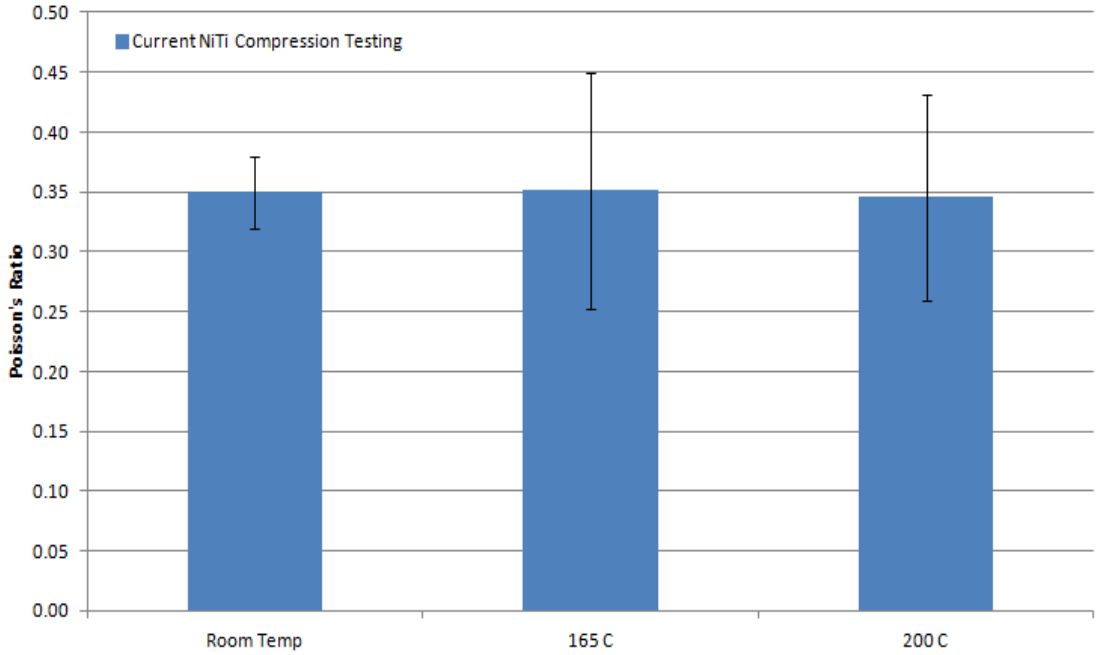

Figure 5.14: NiTi Poisson's Ratio

Finally, a test was conducted to determine whether the cast NiTi specimens retained the deformation recovery abilities of commercially available NiTi. To complete

this test, a previously compressed specimen was placed in the hot air furnace at 200 °C and the axial surface strain was measured for the next few minutes. The test revealed that the material was able to recover 3%-5% of its compressive strain, which is lower than literature suggests, but demonstrates that the poorly cast material still retained some ability to recover deformation.

5.4 Metallographic Evaluation of NiTi

To determine the cause of the specimens' brittleness NiTi specimens were mounted, polished, imaged, and etched for metallographic analyses. Nodes cut from the lattice block structure, end cross sectional views of subelements, and horizontal cross sections of subelements were randomly cut from the NiTi test panel and are shown in Figure 5.15a, b, and c respectively. It can be observed from these unetched images that the node in Figure 5.15a contains cracks and a void, which has been discussed previously. The specimen in Figure 5.15b appears to contain no macro-level defects while the specimen in Figure 5.15c contains cracks.

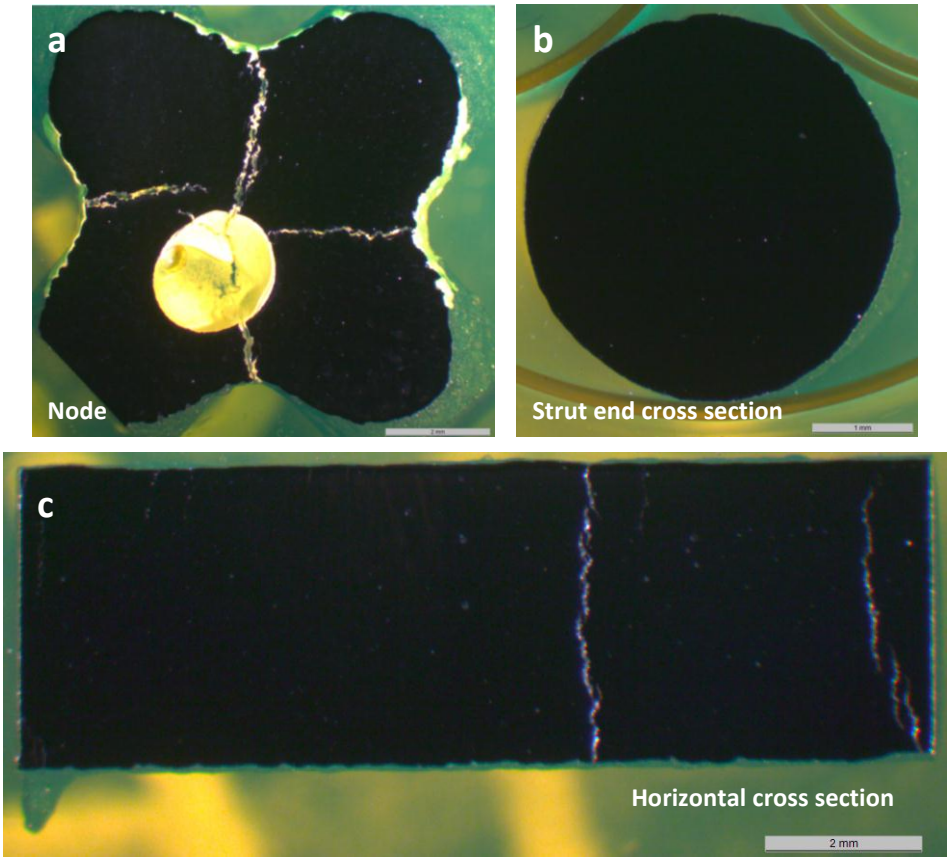

Figure 5.15: Unetched Metallographic NiTi Specimens

The results from optical imaging of the etched node (Figure 5.16) showed that the grains were distributed evenly across the specimen and appeared similar to that of an as-extruded equiatomic NiTi specimen section (Figure 5.17). The end cross section of the subelement shown in Figure 5.18 showed large grains in the center of the specimen with other grains appearing to radiate from the center towards the outside edge of the specimen. The horizontal cross section of Figure 5.19 showed smaller grains in the center, becoming larger as they approach the outside of the specimen.

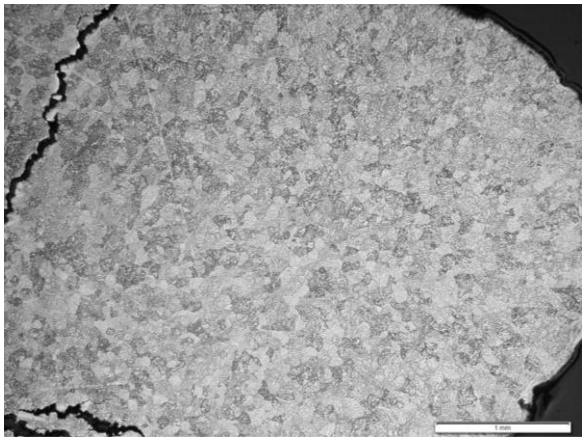

Figure 5.16: Optical Image of Etched NiTi Node Specimen

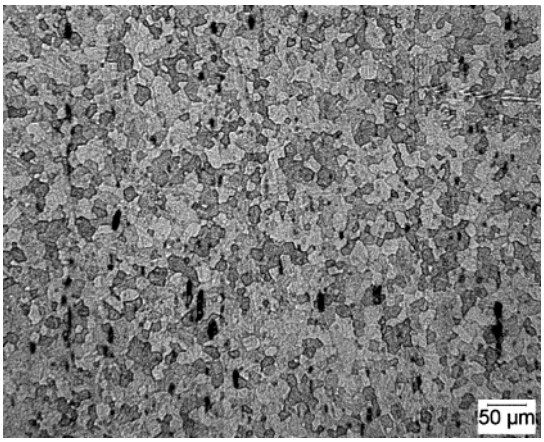

Figure 5.17: Cross Section of Etched As-Extruded NiTi[15]

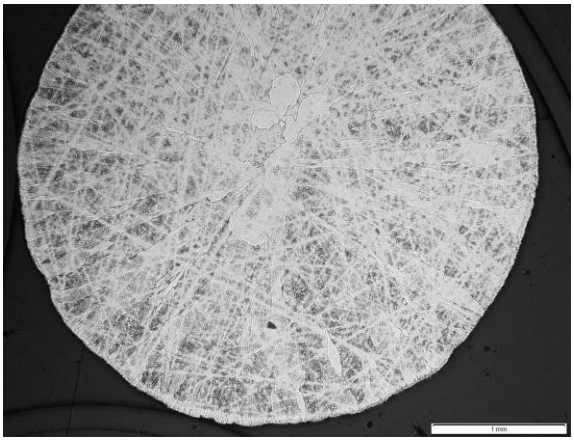

Figure 5.18: Optical Image of Etched NiTi End Cross Sectional View

[15] Image courtesy of Anita Garg, NASA GRC

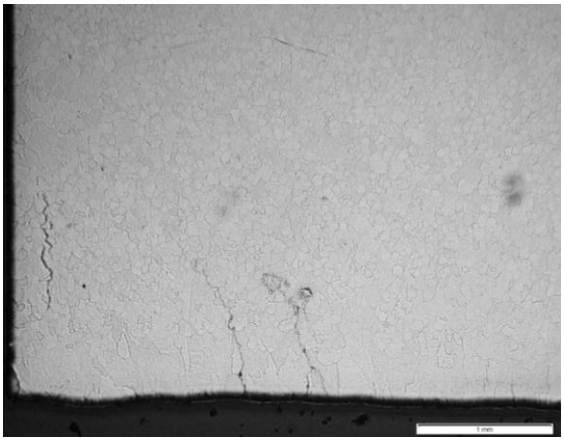

Figure 5.19: Optical Image of Etched NiTi Horizontal Cross Sectional View

While images from the optical scope afforded a macroscopic view of the NiTi grains, a scanning electron microscope[16] (SEM[17]) provided a view of the microstructure of the material at higher resolutions. With the SEM, specimens were found to contain precipitates of Ti_2Ni located mostly at the grain boundaries (Figure 5.20). Ti_2Ni precipitates are a deleterious material phase that promotes brittleness in equiatomic NiTi. As expected, the SEM also captured the room temperature martensite twin within the material grains, which is visible in Figure 5.20. As previously discussed, many of the NiTi specimens contained cracks and the SEM revealed that the cracks occurred along the grain boundaries (Figure 5.21). This is not unexpected since the precipitates that lead to brittleness were found in high concentration along the grain boundaries.

[16] All SEM images courtesy of Anita Garg, NASA GRC
[17] See Appendix A.6 for more information on Scanning Electron Microscopes

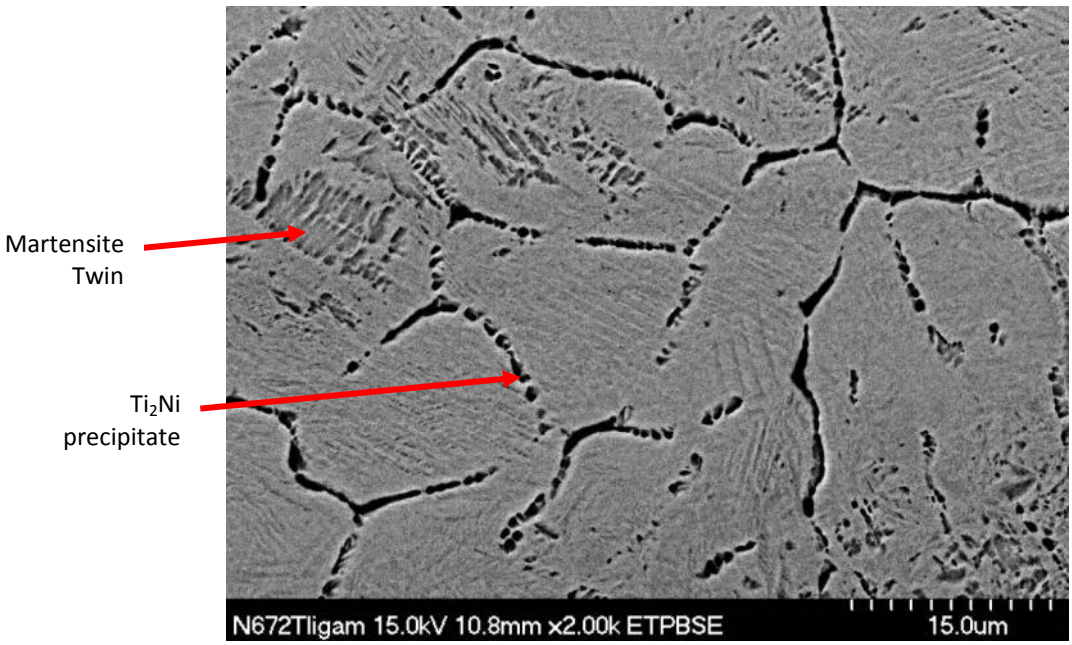

Figure 5.20: SEM Image of a Typical NiTi Test Specimen

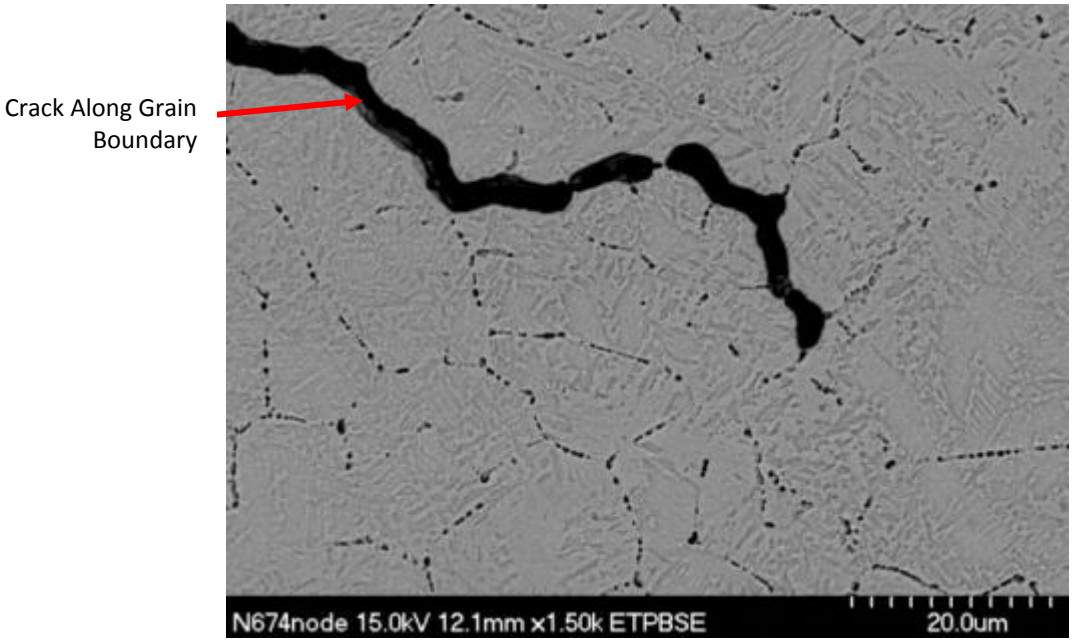

Figure 5.21: SEM Image of a Typical NiTi Test Specimen with a Crack at the Grain Boundary

A chemical analysis[18] was performed on NiTi specimens cut from the test panel used for all subelement testing. The values for the cast NiTi used in this study are compared against ASTM specifications for wrought medical grade NiTi (45) and are shown in Table VIII. Wrought NiTi as opposed to cast NiTi is used as a basis for chemical composition comparison because it was the only equiatomic NiTi with chemical properties available at the time of this writing. As a reminder, the descriptor equiatomic denotes that the chemical composition has an equal atomic percentage of nickel and titanium. This is equivalent to a weight percent of 55% nickel and 45% titanium. The values from test specimens in this project show that the material composition is slightly titanium rich, which is supported by the prevalence of the Ti_2Ni precipitate found along the grain boundaries during the SEM evaluation. The remaining element weight percents show that the test panel casting was within specification for NiTi shape memory alloys.

Table VIII: NiTi Chemical Analysis Results

Element	Average Test Specimen Weight %	ASTM maximum Weight %
Ni	54.2	54.5 to 57.0
C	0.003	0.050
N+O	0.045	0.050
Ti	45.8	balance

[18] All chemical analysis performed by Dereck Johnson, NASA GRC

CHAPTER VI

SUMMARY, DISCUSSION, AND CONCLUDING REMARKS

6.1 Summary

Lattice block structures are lightweight three-dimensional components that can be cast into numerous complex shapes with integral attachment points depending on the application at hand. Lattice block structural components can be fabricated from shape memory alloys that have an ability to change shape either automatically under ambient conditions, or passively from an induced temperature or mechanical stress. Morphing an aircraft airfoil is an example of making good use of these unique shape altering properties. In addition, shape memory alloy lattice block structures have very large energy absorption characteristics. This aspect allows consideration of shape memory alloy lattice block structures for use as a containment device in aircraft engine cases. In order for this type of structural component to reach its full potential, test protocols must be established and exercised on components fabricated with shape memory alloys. This was the primary objective of this thesis. However, tests conducted

here on shape memory alloy lattice block structures produced mixed results. Obtaining consistent shape memory alloy data is highly dependent on the quality of the fabricated material. However, this effort demonstrated how to test as-cast specimens. For comparison, Ti-6-4 lattice block structures were also tested. Testing specimens from Ti-6-4 panels demonstrated minimal panel-to-panel variation. The data obtained from the Ti-6-4 panels exhibited no in-panel orientation effects. This phenomenon will be important in designing systems that utilize lattice block structural components.

The elastic modulus values of the Ti-6-4 specimens tested in tension were found to deviate from published values by 3.3% at room temperature and up to 7.3% at test temperatures of 200 °C. The Ti-6-4 specimens also exhibited lower yield stress and ultimate strengths by 15% and 10% respectively. Data relative to the elastic modulus, yield stress, and ultimate strength properties of the Ti-6-4 specimens decrease with an increase in test temperature. This trend was expected. The Poisson's ratio of the tensile specimens fell in the broad range of expected values taken from literature. The Ti-6-4 specimens failed in different locations due to the non-uniform nature of the specimen surface. The scatter in tensile test data made it difficult to determine quality values for elongation and percent area reduction.

Surface irregularities caused premature bending in the Ti-6-4 compression tests. The non-uniform specimen surface promoted a local collapse mechanism that gave rise to specimen bending. In addition, a non-circular specimen cross section, as opposed to an expected circular one, likely contributed to a bending moment that further increased the chances of a specimen bending. Premature bending led to a relatively large amount

of scatter in the Ti-6-4 compression test data. Even with these difficulties, the elastic modulus, yield stress, and Poisson's ratio aligned, on average, reasonably well with expected values from literature.

A metallographic analysis of random Ti-6-4 specimens found that the casting process had not adversely affected the grain size or distribution within the specimens. The analysis did show that the casting process had introduced a small amount of inclusions that were most likely carbon. A chemical analysis showed that the cast material was within commercial specifications for Ti-6-4 alloy.

Because of the extreme brittleness of the NiTi material, tension tests could not be completed. A series of compression tests on specimens cut from the core of the NiTi lattice block structure were completed at room temperature, 165 °C and 200 °C. Results exhibited a large amount of scatter in the data. As with Ti-6-4, scatter from compression tests can be attributed to surface irregularities and an oval cross section that lead to premature bending during testing. Furthermore, the precipitates from the casting process lead to specimen brittleness and data scatter. A comparison of room temperature NiTi data obtained from this project was made with other NASA compression testing on extruded NiTi. NiTi test specimens obtained from the lattice block structure showed, on average, a 22% lower apparent elastic modulus compared with the extruded material. The cast NiTi material exhibited reorientation start and finish stresses that were 3.5% and 12% higher, respectively, compared to the extruded material properties. With no point of comparison for the elevated temperature data, the data can only be reported as nominal averaged values. The average apparent elastic

modulus was 7.4 Msi (51 GPa) and 7.1 Msi (49 GPa) for the 165 °C and 200 °C testing. The average reorientation start stress was 66 ksi (455 MPa) and 82 ksi (565 MPa) for the 165 °C and 200 °C compression tests.

Several specimens exhibited cracks in a macroscopic evaluation of the specimens. The cast NiTi specimens removed from node regions contained voids as well as cracks from the casting process. A microscopic metallographic analysis showed grain sizes and grain orientations consistent with as-extruded equiatomic NiTi for most specimens. The node specimens contained grains similar to as-extruded NiTi. Specimens cut longitudinally showed large grains on the outside that became smaller towards the center of the specimen. This is not unusual for cast NiTi. End cross sectional views of strut specimens showed relatively large grains that extended radially from the center of the specimen toward the outside edge. A scanning electron microscope evaluation confirmed that the material brittleness was the result of a Ti_2Ni precipitate that appeared along the material grain boundaries. A chemical analysis showed a slightly titanium rich composition, supporting the finding of Ti_2Ni precipitate under the scanning electron microscope inspection.

6.2 Remarks on Ti-6-4 Tension Testing

The primary sources contributing to scatter in the Ti-6-4 tension test data are as follows: non-uniform cross sections from the casting process, machining nicks, and the

“V” (vertically oriented) specimens slipping in the grips. Due to the non-uniform nature of the specimens resulting from the casting process, the measured cross sectional area is not uniform along the length of the specimen. A local thick or thin region on the specimen surface can cause failure to migrate to a location where the cross section was not measured. A major and minor diameter was measured for each specimen and those values were averaged and used for the cross sectional area calculations.

Nicks from grinding and the inability to polish specimens to remove the nicks was a source of scatter in the data. An example of a typical nick is shown in Figure 6.1. For the specimens to fit tightly into the grips it was necessary to cut specimens from the panels with very little extraneous material in the grip region. Figure 6.2, left image, and Figure 6.3 show a transverse specimen. Figure 6.3 is annotated to show the different leg orientations of the transverse specimen. The 45° internal leg must be removed in order to fit the specimen in the fixture. Removal of the leg without nicking the surrounding areas of the specimen posed a challenge. The internal 45° leg was removed first via electrical discharge machining to within 0.025 inch (0.64 mm) from the edge of the specimen gage section. The specimen was then carefully ground to fit in the fixture. This procedure worked well for most specimens. However, nicks from the grinding process occurred in a small number of specimens and these artificially introduced defects leading to premature failure. The external 45° leg (Figure 6.3) on transverse test specimens also required removal to fit in the fixture. The fixture was designed to allow for, at most, 0.050 inch (1.27 mm) of the external leg material to remain. Note that the pictured transverse specimen has an untrimmed node in the gage region. All specimens

tested had this extraneous material removed. The vertical specimens as shown in the right image of Figure 6.2, as well as Figure 6.4, were less troublesome to prepare for testing. Figure 6.4 is annotated to show the leg orientations of the vertical specimens. To fit in the fixture, the vertical specimens did require the removal of the extraneous axial leg which is identified in Figure 6.4. The fixture was designed to accommodate no more than 0.050 inch of the remaining axial leg. Few machining defects were generated in the preparation of vertical test specimens.

Figure 6.1: Tensile Specimen with Machining Nick

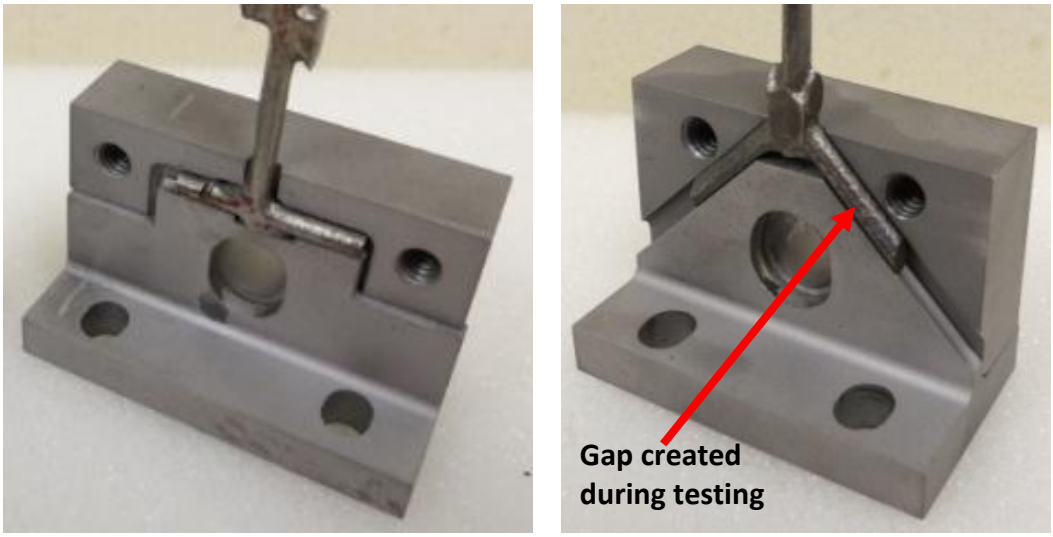

Figure 6.2: Transverse (Left) and Vertical (Right) Specimens in Fixture

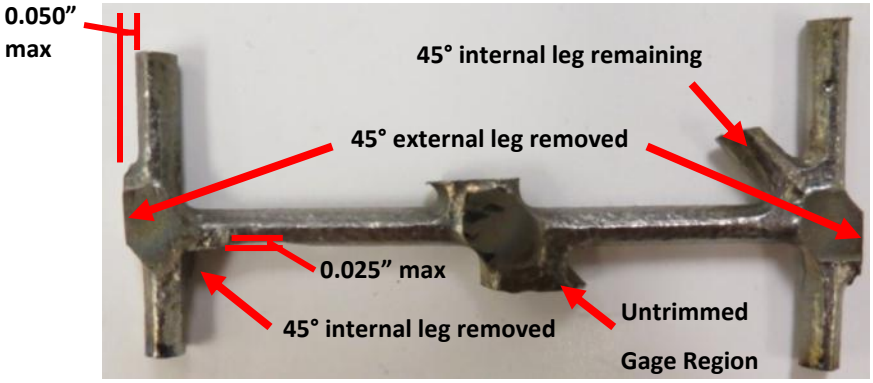

Figure 6.3: Transverse Specimen Before Final Trimming

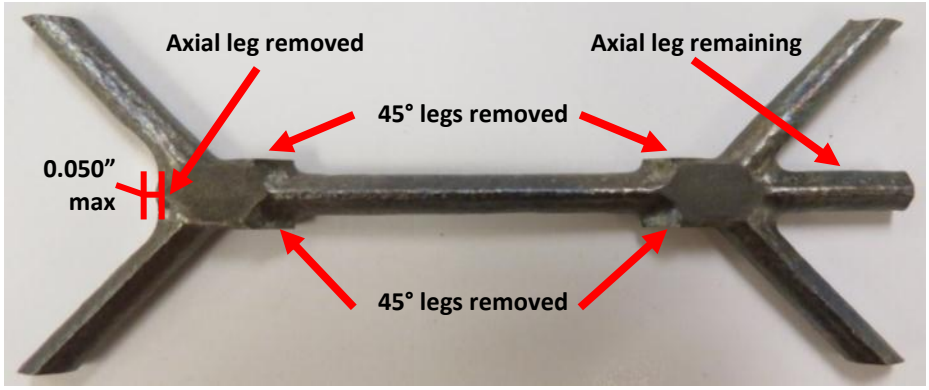

Figure 6.4: Vertical Specimen Before Final Trimming

While the preparation of vertical (V) test specimens did not give rise to machining defects, pre-test inspections indicated that all specimens did not have consistent dimensions, especially the diameter of the cross section. Because of this, the fixture was designed to accommodate varying dimensions. Even with this flexibility, several vertical specimens did not fit well within the fixture. The portion of the test specimen gripped by the test fixture was wrapped in aluminum foil with the goal of eliminating a loose fit. This did not stabilize the specimens. As vertical test specimens were loaded they failed in the grips from a gap created between the specimen and the insert (see right image of Figure 6.2). The insert was no longer in contact with the specimen legs and the legs were bent down until a stable configuration was obtained. The test fixture did not generate the distributed load shown in Figure 6.5 along the legs of the specimen in this situation. Due to the gaps between the test specimen and the test fixture, point loads depicted in Figure 6.6 were applied. When the force from the load train was transmitted to a single application point, it tended to produce a shear failure inside the grip. This type of failure is shown in Figure 6.6. These failure modes were not generated in transverse (T) specimens because their leg orientation and the fixture design sufficiently restrained the specimen. For transverse test specimens, test loads were evenly distributed along the arms as indicated in Figure 6.7.

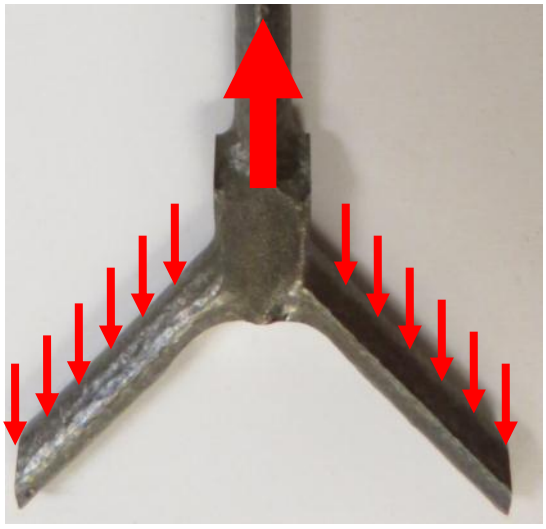

Figure 6.5: Vertical Specimen Ideal Load Condition

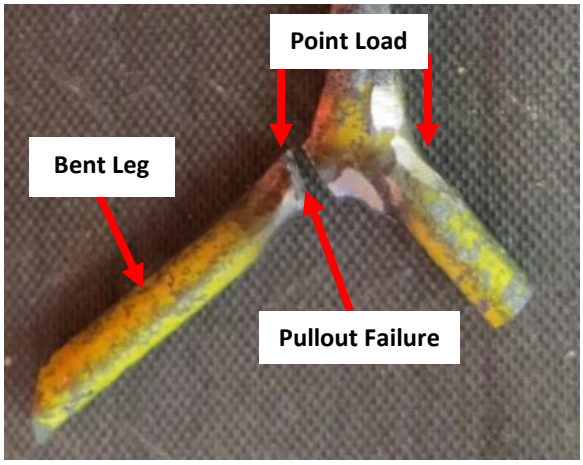

Figure 6.6: Vertical Specimen after "Pullout" Failure

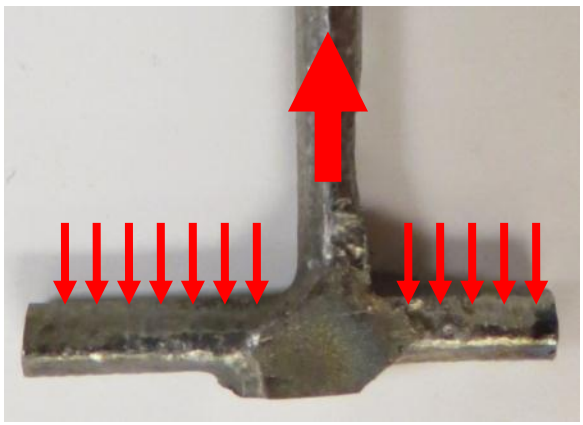

Figure 6.7: Transverse Specimen Ideal and Actual Load Condition

6.3 Ti-6-4 Compression Testing

A number of bending failures occurred in compression tests. An ideal failure in compression occurs when the specimens expand uniformly in a radial direction. The non-circular cross sections of the compression test specimens proved problematic since they create inaccuracies in the computation of the cross sectional area of the specimen. Consistent with tension testing, a major and a minor diameter was measured for all compression test specimens. These values were then averaged to obtain a representative cross sectional area.

Initially the specimens were cut to a 2:1 height to diameter ratio. This is consistent with the applicable ASTM compression testing test standard (31). All compression test specimens were inspected to verify that the ends were parallel and the machine alignment was verified to be within specifications. However, during testing some specimens bent in random directions. The random nature of the bending patterns indicates that machine misalignment did not cause these types of failures. To mitigate failures by bending, compression specimens were fabricated to successively shorter lengths until repeatable tests were obtained. Shorter specimens will have higher end effects and this was investigated. Data from long compression specimens (those with a height to diameter ratio of 2:1) that had failed in bending past the yield point were compared to the data from shorter specimens. It was determined from the data that, within data scatter, that there was no appreciable effect on the modulus, yield stress, or

Poisson's ratio with shorter test specimens. After several tests, a height to diameter ratio of 1.5:1 was selected to give acceptable results.

The full field strain measurements offered additional information on the premature bending failures. The texturing, shown in Figure 6.8, creates surface perturbations that promote regions of high stress, leading to local collapse in the specimens. Since the collapsing was not evenly distributed across the cross section, it allowed the specimen to bend locally initiating failure. A perfectly machined specimen will not produce this type of failure.

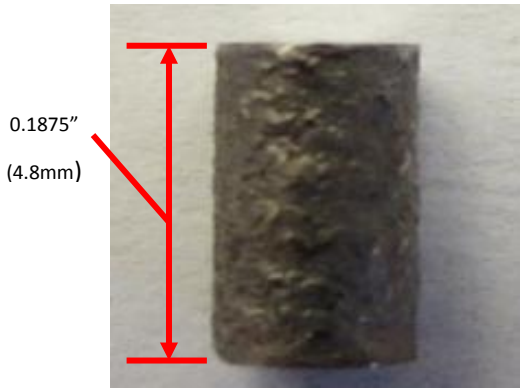

Figure 6.8: Typical Surface Texturing of As-Cast Ti-6-4 Compression Specimens

To prove that the surface irregularities were creating a perturbation that initiated bending failures, a small number of compression specimens were cut from oil-quenched tool steel round stock and the ends were ground parallel. The nominal dimensions of the specimens were 0.314 inch (7.97mm) in diameter and 0.500 inch (12.7mm) in height. The specimens were tested at an elastic strain rate of 10^{-4} in/in/s. This was consistent with the strain rate of the other compression tests conducted in this project. Figure 6.9 shows a significant difference in the surface strain variation between

the well-machined tool steel specimen (left images) and the as-cast Ti-6-4 test specimen (right images). Note that the images are evenly spaced through the respective tests and the strain scales are consistent for both image sets. The tool steel specimen at the end of the test had a maximum axial surface strain variation of approximately 2%, while the Ti-6-4 cast specimen varied by nearly the entire 10% scale. The comparison portrayed in the figure indicates that the surface irregularities of the cast specimens are leading to bending failure in the compression specimens.

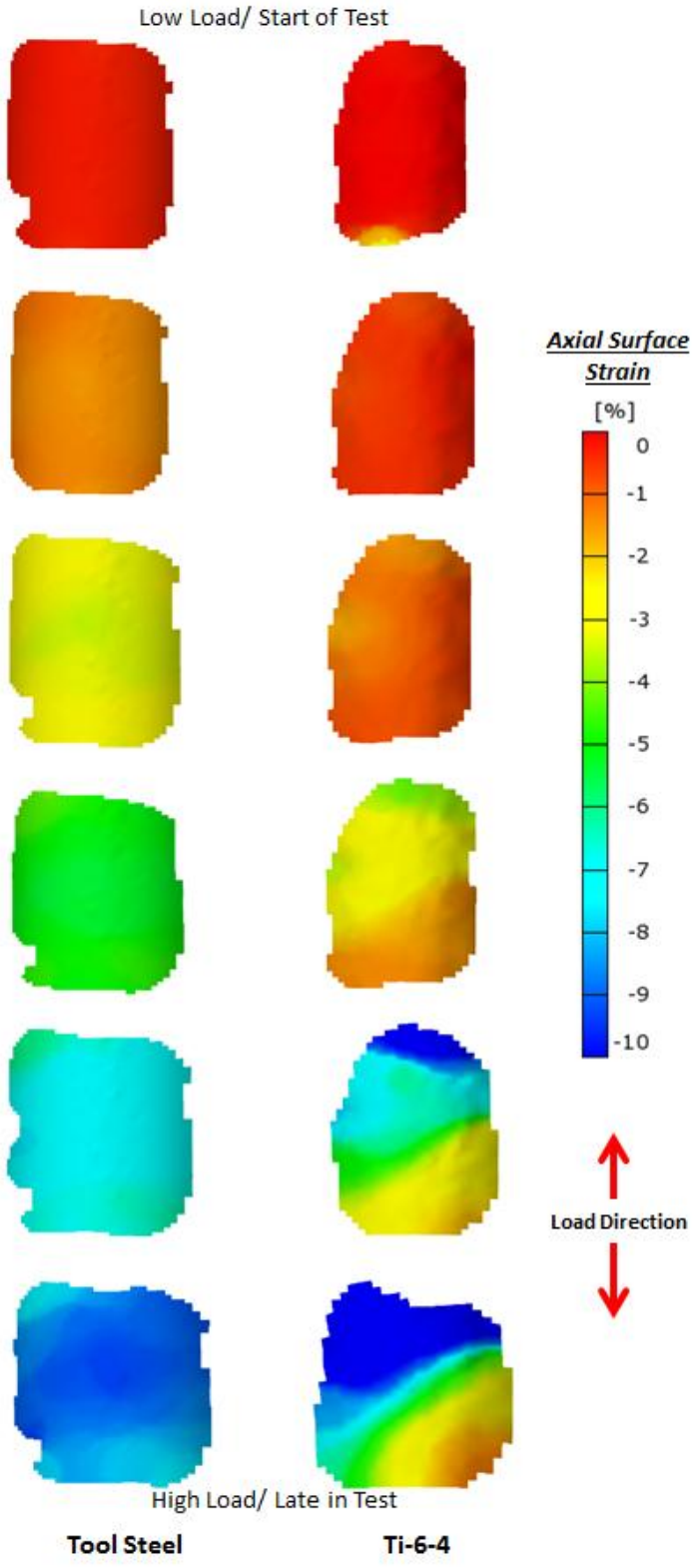

Figure 6.9: Comparison of Axial Surface Strain for Well-Machined Tool Steel and As-Cast Ti-6-4 Specimens

When bending failures occurred early in a test, these test specimens dramatically lowered the elastic modulus. At 200 °C, 40% of the specimens experienced premature bending failures. Elevated temperature promotes increased ductility by lowering yield stresses leading to more bending failures then at the other test temperatures. Ideally, all compression specimens should fail by displacement run-out. If the bending failures are ignored, the difference in the elastic modulus from the compression data and published data reduces from 17% to 3% at the 200 °C test temperature.

6.4 Remarks on NiTi Tension Test

Tension tests could not be conducted on the NiTi tensile specimens. The material was too brittle due to problems with the casting process. Most specimens either broke while being prepared for testing or failed at unrealistically low load. Voids and cracks at nodes further reduced the strength of the specimens. Future improvements to the casting process should provide specimens that are better suited for testing. The shape memory alloy test specimens used for this test program were equiatomic but were actually slightly rich in titanium. As a result, a brittle dual phase region of NiTi and Ti_2Ni was present. The dual phase region was observed with a scanning electron microscope. Figure 6.10 is a phase diagram for NiTi that shows the equiatomic phase line where the material should have been for this project and the dual phase region of NiTi and Ti_2Ni, i.e., the material that was tested in this project. A minor

deviation from the equiatomic phase line will result in precipitates forming in the material. Changing to a nickel rich material composition would allow for reheating, heat treatment, and subsequent quenching of the material to eliminate precipitates (28). This would result in a more easily cast shape memory alloy lattice block structure. However, some of the shape memory properties, as well as the transformation temperatures, will diminish in a nickel-rich composition. With the current material composition, subsequent reheating will liquefy the material, but this will not remove the precipitates once cooled.

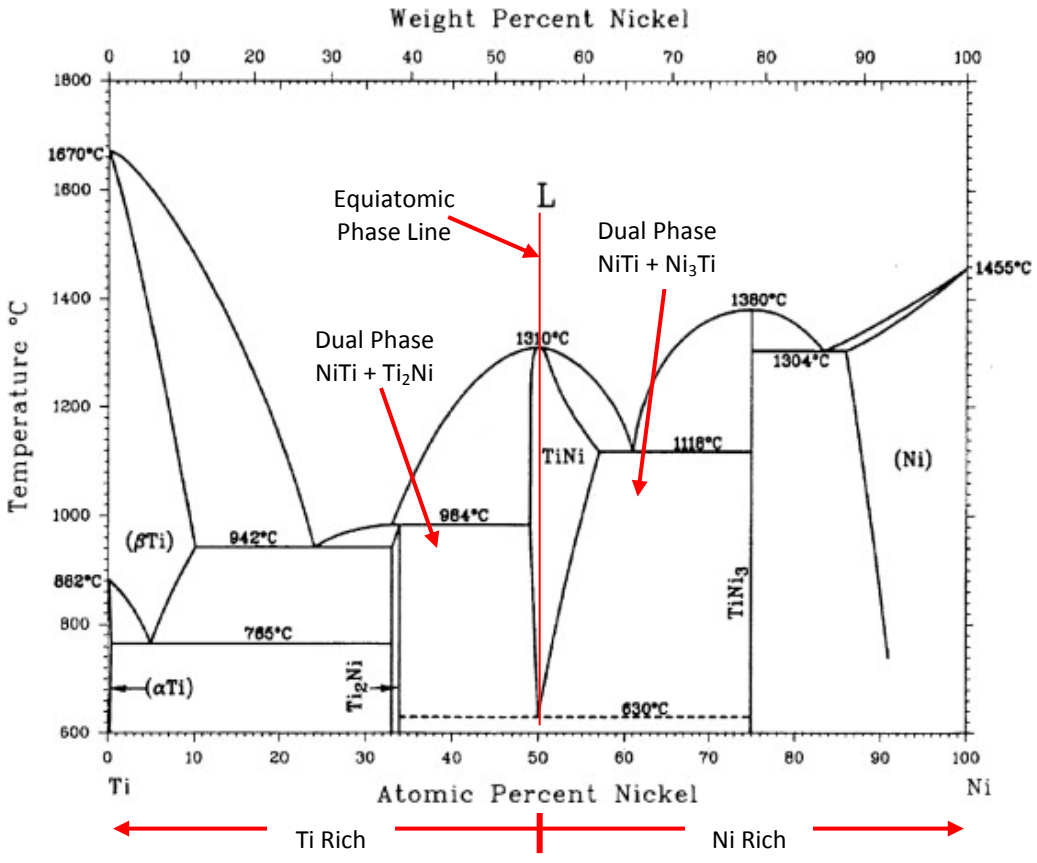

Figure 6.10: NiTi Phase Diagram (46)

6.5 NiTi Compression Testing

As with the Ti-6-4 specimens, a height to diameter ratio of 2:1 was initially adopted but was quickly reduced to eliminate bending failures at higher strain levels. The lengths of NiTi compression specimens were reduced to a length to diameter ratio of 1.15:1. This length was near the limit of the machining capabilities. Premature bending failures were still common at this ratio due to surface texturing (Figure 6.11) in addition to the non-circular cross section.

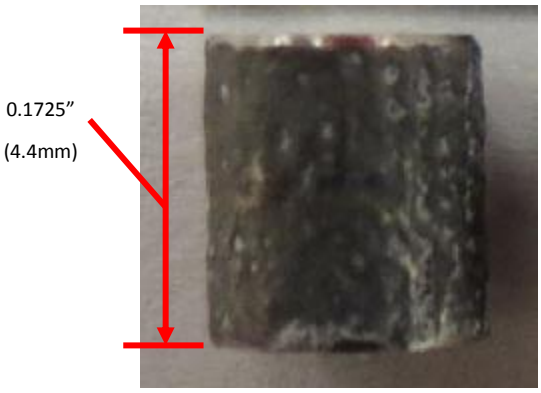

Figure 6.11: Typical Surface Texture of As-Cast NiTi Compression Specimens

6.6 Conclusions and Future Efforts

Conducting tests on specimens obtained from an as-cast small structure is not straightforward. Even with the problems encountered, baseline data was obtained at three temperatures for as-cast Ti-6-4. This data was compared with as-cast NiTi used to fabricate lattice block structures. The data obtained has shown that the manufacturing of cast equiatomic NiTi lattice block structures is not currently of the same quality as Ti-

6-4 lattice block structures. The casting process for NiTi introduced precipitates into the material that made the normally very ductile material, very brittle. It was demonstrated here that even with the precipitates present, the material can retain some of its shape memory capabilities.

Unfortunately, the funding for this project was limited at the outset. Based on results presented in this thesis, future attention should be placed on lattice block structures cast from a different composition of NiTi. The data obtained from the new compositions should be compared with the data presented here. In addition, testing efforts should also focus on auxetic structures (i.e. structures with a design that exhibit a negative Poisson's ratio)[19] cast from Ti-6-4 and the new composition of NiTi. Adding this characteristic to lattice block structures can further increase their energy absorbing ability. Thermal cycling tests on Ti-6-4 and the new composition of NiTi should be conducted to augment the publically available mechanical properties database complied for the materials. The goal should be the creation of a large enough database of material properties such that engineered components can be designed for a multitude of applications.

[19] See Appendix A.7 for more information on auxetic structures

BIBLIOGRAPHY

1. **Ott, E.A.** *Superalloy Lattice Block.* [.pdf] Cincinnati : NASA, 2003. NASA/CR-2003-212719. pp. 2-39.

2. **Beiss, P., El-Magd, E., Stuhrmann, J.** *Flow Behavior of Sandwich Structures for Cooling Thermally Highly Steam Turbine Components.* [.pdf] s.l. : Advanced Engineering Materials, 2008. Vol. 11. p.359.

3. **Nathal, M.V., Krause, D.L., Bednarcyk, B., Padula, S.** *Three Dimensional Cellular Structures Enhanced By Shape Memory Alloys.* Cleveland : NASA Glenn Research Center, 2010. p. 1.

4. **Bartolotta, P.** *Aerospace Weight Reductions by Incorporating Shape Memory Alloys.* [interv.] N. G. Wilmoth. Cleveland, December 10, 2013.

5. *Aerospace applications of shape memory alloys.* **Harlt, D.J., Lagoudas, D.C.** 535, s.l. : SAGE, 2007, Vol. 221, pp. 535-547.

6. **Chen, Q.F., et al.** *NiTi wire as a superelastic damping material in structural engineering.* [.pdf] s.l. : ELSEVIER, Materials Science and Engineering, 2006. pp. 1089-1092.

7. **Saadat, S., et. al.** *An Overview of vibration and seismic applications of NiTi shape memory alloy.* [.pdf] s.l. : IOP Publishing, LTD, 2002. Smart Materials and Structures, Vol. 11. p. 224.

8. **Oberg, E., Jones, F.D., Horton, H.L., Ryffel, H.H.** *Machinery's Handbook 28th Edition.* New York : Industrial Press, 2008. pp. 378-1326.

9. **Wallach, J.C., Gibson, L.J.** *Defect Sensitivity of a 3D truss material.* [.pdf] s.l. : Scripta Materialia, 2001. Vol. 45. pp. 639-644.

10. **Nathal, M.V. Whittenberger, J.D., Hebsur, M.G., Kantzos, P.T., Krause, D.L.** *Superalloy Lattice Block Structures.* [.pdf] Cleveland : The Minerals, Metals & Materials Society, 2004. pp. 2-438.

11. **Krause, D.L., et. al.** *Mechanical Testing of IN-718 Lattice Block Structures.* [.pdf] Cleveland : NASA, 2002. NASA/TM-2002-211325. p. 9.

12. **Krause, D.L., et.al.** *Superalloy Lattice Block Structures.* [.pdf] Cleveland : The Minerals, Metals & Materials Society, 2004. p. 434.

13. *High Strength-per-Weight Cellular Metals Fabricated of Wires.* **Lee, Byung-Kon, Kang, Ki-Ju.** 9, s.l. : Advanced Engineering Materials, 2008, Vol. 10, p. 835.

14. *Standard Specifications for Investment Castings, Steel and Alloy, Common Requirments, for General Industrial Use.* West Conshohocken, PA : ASTM, 2011. A957/A957M-11a.

15. **Horton, R.A.** Investment casting. [book auth.] ASM International Handbook Committee. *Metals Handbook.* 9. Metals Park : ASM International, 1988, Vol. 15: Casting, pp. 257-263.

16. Investment Casting from Pennsylvania Precision Cast Parts. *Pennsylvania Precision Cast Parts, Inc.* [Online] [Cited: 1 25, 2012.] http://www.ppcpinc.com/.

17. *Lightweight Structures and Materials.* **Evans, A.G.** October 2001, s.l. : MRS Bulletin, 2001, Vol. 36, p. 795.

18. **Evans, A.G., et al.** *The topological design of multifunctional cellular metals.* [.pdf] s.l. : Progress in Materials Science, 2001. Vol. 46. pp. 310-326.

19. **Hebsur, M.G.** *Processing of IN-718 Lattice Block Castings.* [.pdf] Brook Park : NASA, 2002. NASA/CR-2002-211332. pp. 3-10.

20. *Cellular Metal Truss Core Sandwich Structures.* **Sypeck, D.J., Wadley, H.N.G.** 10, s.l. : Advanced Engineering Materials, 2002, Vol. 4, pp. 759-764.

21. **Li, Q., Chen, E.Y., Bice, D.R., Dunand, D.C.** *Mechanical Properties of Cast Ti-6Al-4V Lattice Block Structures.* [.pdf] s.l. : Metallurgical and Materials Transactions, February 2008. Vol. 39A. pp. 441-449.

22. **Patoor, E., Lagoudas, D.C., Pavlin, B.E., Brinson, L.C., Gao, X.** *Shape memory alloys, Part I: General properties and modeling of single crystals.* [.pdf] s.l. : ELSEVIER, 2006. Mechanics of Materials, Vol. 38. pp. 404-406.

23. **Funakubo, H.** Shape Memory Alloys. [trans.] J.B. Kennedy. *Precision Machinery and Robotics.* New York : Gordon and Breach Science Publishers, 1984, Vol. 1, pp. 1-201.

24. Measuring Transformation Temperatures of Nitinol Alloys. *Johnson Matthey Medical Components.* [Online] [Cited: October 30, 2012.]

http://jmmedical.com/resources/211/Measuring-Transformation-Temperatures-in-Nitinol-Alloys.html.

25. **Xu, Dong, et al.** Characteristics and fabrication of NiTi/Si diaphram micropump. *Sensors and Actuators.* A, 2001, Vol. 93, pp. 87-92.

26. **Garg, Anita.** *A Discussion on Equiatomic NiTi.* [interv.] N. G. Wilmoth. November 16, 2012. Personal Communication.

27. **Padula, S.A.** *A Conversation About Mechanics and Shape Memory Alloys.* [interv.] N. G. Wilmoth. June 26, 2012.

28. **Bigelow, Glen.** *A Discussion on the NiTi Phase Diagram.* [interv.] N. G. Wilmoth. 8 31, 2012.

29. **Buehler, W.J., Wang, F.E.** *A Summary of Recent Research on the Nitinol Alloys and their Potential Applications in Ocean Engineering.* [.pdf] Great Britian : Pergamon Press, 1968. Ocean Engineering, Vol. 1. pp. 105-120.

30. **Jackson, C.M., Wagner, H.J., Wasilewski, R.J.** *55-Nitinol--The Alloy with a Memory: Its Physical Metallurgy, Properties, and Applications.* [.pdf] Washington D.C. : Technology Utilization Office, National Aeronautics and Space Administration, 1972.

31. *Standard Test Methods of Compression Testing of Metallic Materials at Room Temperature.* West Conshohocken, PA : ASTM, 2009. E9-09.

32. **Budynas, R.G., Nisbett, J.K.** *Shigley's Mechanical Engineering Design.* 8. New York : McGraw Hill, 2008. pp. 90-178.

33. **Carpenter Technology Corporation.** AerMet-for-Tooling Alloy. [Technical Data Sheet].

34. **Lerch, B.** *Work Instructions: Temperature Uniformity In Test Specimens Using Type K Thermocouples.* [.pdf] Clevleand : NASA, 2007. pp. 4-5. GLWI-RXL-8210.15.

35. ARAMIS - Optical 3D Deformation Analysis. *gom Optical Measuring Techniques.* [Online] [Cited: 10 18, 2011.] http://www.gom.com/metrology-systems/system-overview/aramis.html.

36. *Standard Test Method for Tension Testing of Metallic Materials.* West Conshohocken, PA : ASTM, 2009. E8/E8M.

37. *Standard Practice for Compression Tests of Metallic Materials at Elevated Temperatures with Conventional or Rapid Heating Rates and Strain Rates.* West Conshohocken, PA : ASTM, 2000. E209-00.

38. *Standard Test Method for Tension Testing of Nickel-Titanium Superelastic Materials.* West Conshohocken, PA : ASTM, 2007. F2516-07.

39. *Uniaxial True Stress-Strain after Necking.* **Ling, Yun.** June 1996, AMP Journal of Technology, Vol. 5, pp. 37-48.

40. **Allegheny Technologies, Incorporated.** *ATI Titanium 6Al-4V Alloy Technical Data Sheet.* [.pdf] 2010.

41. Materials Properties Handbook: Titanium Alloys. Materials Park : ASM International, 1994, pp. 492-634.

42. **Eylon, Daniel and Newman, Jeremy R.** Titanium and Titanium Alloy Castings. *Metals Handbook.* 10. s.l. : ASM International, 1990, Vol. 2, pp. 634-640.

43. *Aerospace Material Specifications: Titanium Alloy, Sheet, Strip, and Plate, 6Al-4V, Annealed.* [.pdf] s.l. : SAE Aerospace, 2003. AMS 4911J.

44. **Benafan, Othmane.** 55NiTi Compression Data. Cleveland : s.n., 2012.

45. *Standard Specification for Wrought Nickel-Titanium Shape Memory Alloys for Medical Devices and Surgical Implants.* West Conshohocken : ASTM, 2005. F 2063.

46. **Elahinia, Mohammad, et al., et al.** Manufacturing and processing of NiTi implants: A review. *Progress in Materials Science.* 2012, Vol. 57, 5.

47. *PRESENT STATE OF MODELING OF HOT ISOSTATIC PRESSING.* **Kaysser, W.A.** Gaithersburg, MD : ASM, 1989.

48. Hot Isostatic Pressing. [Online] [Cited: November 11, 2011.] http://www.hempel-metals.com/UserFiles/File/hot%20isostatic%20pressing.pdf.

49. Solidscape 3D Printers. *Solidscape, A Stratasys Company.* [Online] [Cited: 9 28, 2011.] http://www.solid-scape.com/solutions-for-investment-casting/3D-wax-printers.html.

50. What is the Plastic Injection Moulding Process? *Rutland Plastics Limited.* [Online] [Cited: 4 12, 2012.] http://www.rutlandplastics.co.uk/moulding_process.shtml.

51. Countergravity Casting. *Hitchinger.* [Online] [Cited: October 2, 2012.] http://www.hitchiner.com/countergravity-casting.html.

52. Scanning Electron Microscope. *Purdue University Radiological and Environmental Management.* [Online] August 29, 2012. [Cited: August 30, 2012.] http://www.purdue.edu/rem/rs/sem.htm.

APPENDIX A

EXTENDED DEFINITIONS

This appendix includes extended definitions for processes and terms that have been used or discussed throughout this thesis.

A.1 Hot Isostatic Pressing

Hot isostatic pressing is the process of optimizing near net shaped parts on a microstructural level (47). The process increases the density of metallic and ceramic materials by combining heat and pressure to a part in a furnace. Hot isostatic pressing will close material porosity and can be used on parts ranging from a few pounds up to several tons. The process can potentially save on material and machining costs (48).

A.2 Rapid Prototyping

Three dimensional printers allow a pattern to be “printed” in thin layers of wax or plastics. The process works by first having a designer create a 3D drawing of a part. Next, the file is sent to the printer where it begins laying down, and curing, thin layers of material, building the part from the bottom up or top down, depending on printer model. This process allows very intricate and high quality parts to be fabricated (49).

A.3 Injection Molding

Injection molding is a process for making low cost, high quality parts quickly. The part material is supplied as a granule and is melted and injected into a mold. The shape of the mold is copied and the solidified part is removed from the mold. The process is repeated if multiple parts are required (50).

A.4 Hitchiner Counter Gravity Casting Method

The Hitchiner casting process places the part tree in a vacuum chamber with the fill pipe facing downward toward the melted material. The part tree is lowered into the melt and the vacuum draws the material into the mold, completely filling it. The parts are held briefly to allow for some solidification and the vacuum is then released to allow residual material to flow out of the mold. This casting method contains much less waste and inclusions compared to ladle pour methods (51).

A.5 Alumina

Alumina is a very compressively strong ceramic material. Compressive strength can range from 315-400 ksi depending on the grade of Alumina (8). By comparison, the fixture material used in this study, Aermet-100, has ultimate tensile and compressive strength of 285 ksi (33).

A.6 Scanning Electron Microscope

A scanning electron microscope does not use light, as with traditional optical microscopes. Instead of light, it utilizes electrons to create an image. SEM's have the advantage of having a very large depth of field allowing images of specimens to be in focus even if the specimen has an irregular surface. Furthermore, SEM's have a very high resolution and allow specimens to be precisely magnified to a much higher level, compared to optical microscopes (52).

A.7 Auxetic Structure

An auxetic structure is a structure that exhibits a negative Poisson's ratio. The structure is manufactured from conventional materials with typical Poisson's ratio. The special design of the structure allows for the expansion of some of the internal structure when it is tensile loaded and conversely, the contraction of some of the internal structure when it is compressively loaded.

APPENDIX B

FIXTURE DRAWINGS

This appendix includes all part drawings for extensometry, various specimen fixtures, and load train components. All of the components presented here were fabricated specifically for the test program outlined in this thesis.

B.1 Extensometer Step-Down Adapter

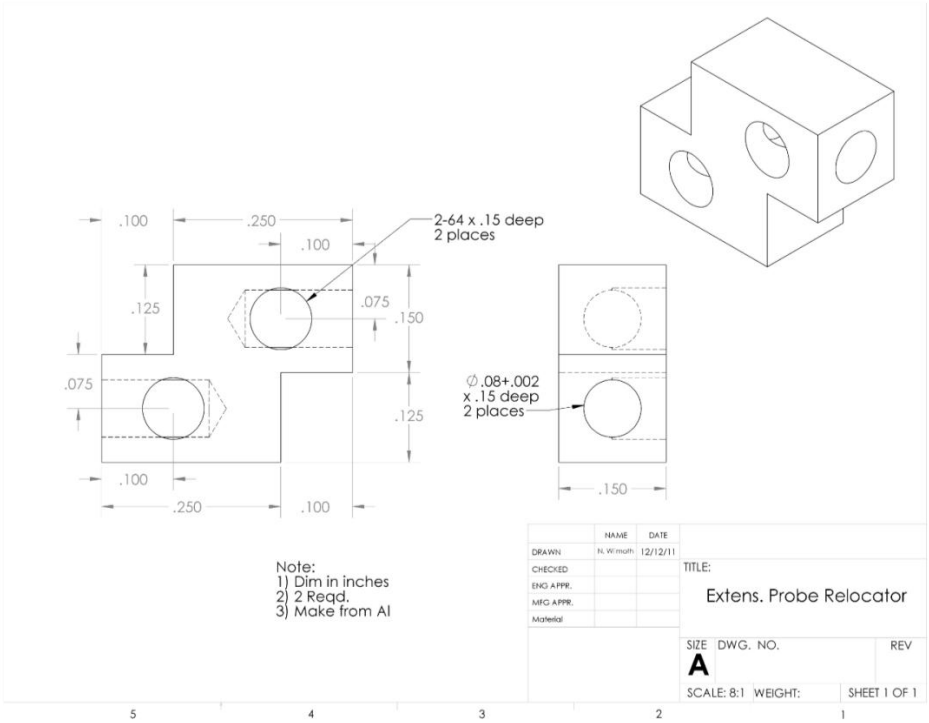

Figure B.1: Step-down Adapter to Reduce 0.5 inch Gage Length Extensometer to 0.25 inch Gage Length

B.2 One Half of Clamshell Fixture for Transverse Specimens

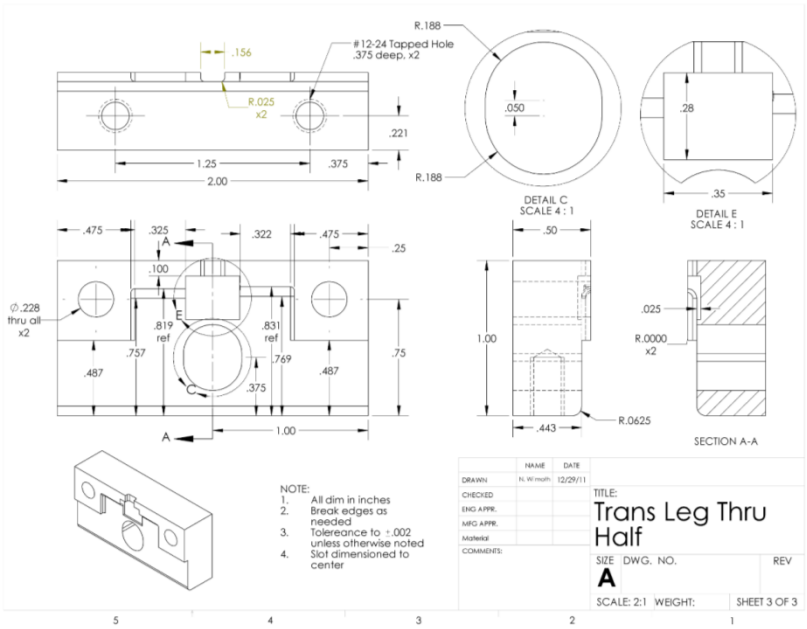

Figure B.2: Transverse Specimen Fixture Half without Upper Threaded Holes

B.3 Second Half of Clamshell Fixture for Transverse Specimens

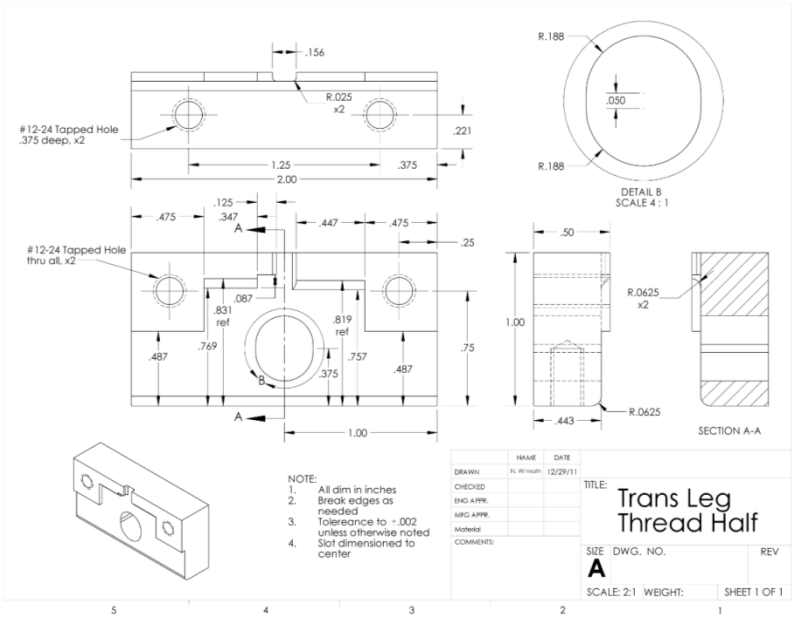

Figure B.3: Transverse Specimen Fixture Half with Upper Threaded Holes

B.4 Insert Restraint Fixture for Transverse Specimens

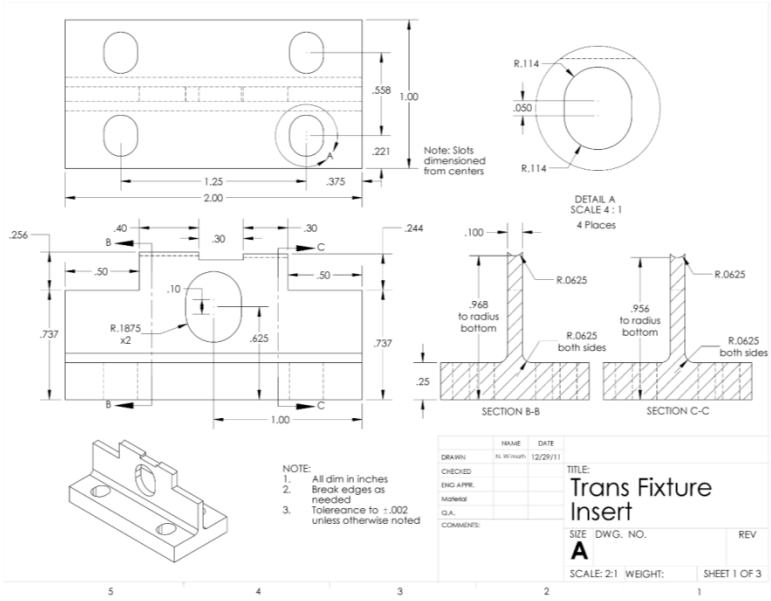

Figure B.4: Fixture Insert for Restraining "pullout" of the Transverse Specimens during Testing

B.5 One Half of Clamshell Fixture for Vertical Specimens

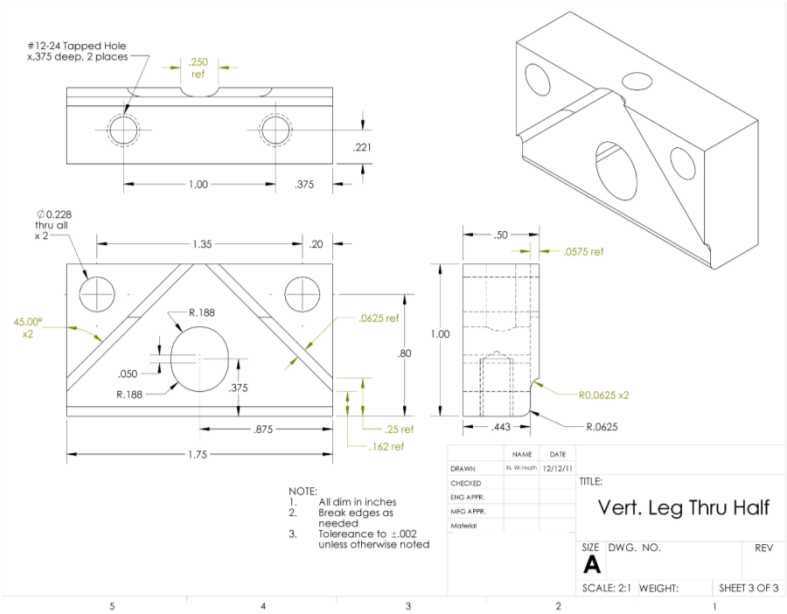

Figure B.5: Vertical Specimen Fixture Half without Upper Threaded Holes

B.6 Second Half of Clamshell Fixture for Vertical Specimens

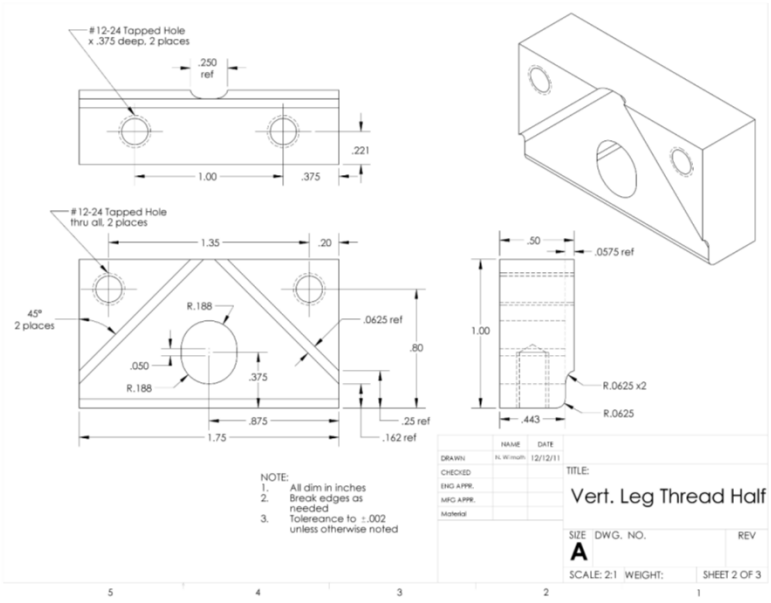

Figure B.6: Vertical Specimen Fixture Half with Upper Threaded Holes

B.7 Insert Restraint Fixture for Vertical Specimens

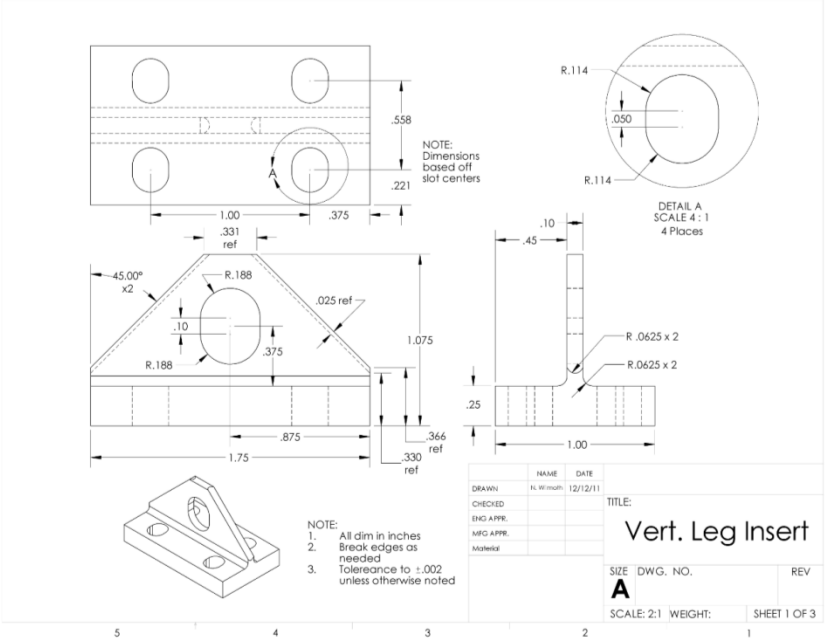

Figure B.7: Fixture Insert for Restraining "pullout" of Vertical Specimens during Testing

B.8 Clevis Fixture

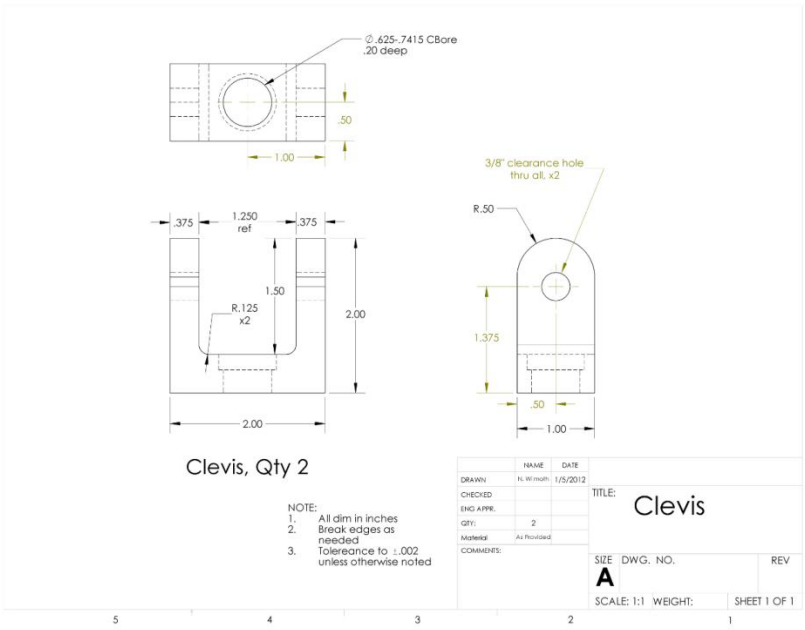

Figure B.8: Clevis for Mounting the Clamshell Fixtures into the Test Frame

B.9 Clevis Pull Rods

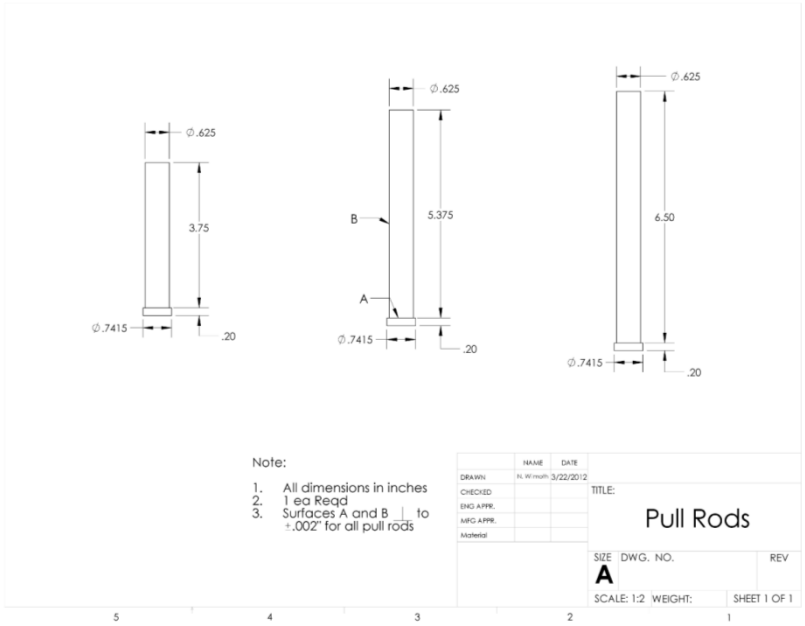

Figure B.9: Clevis Pull Rods of Differing Lengths to Accommodate All Test Specimens

B.10 Compression Rods

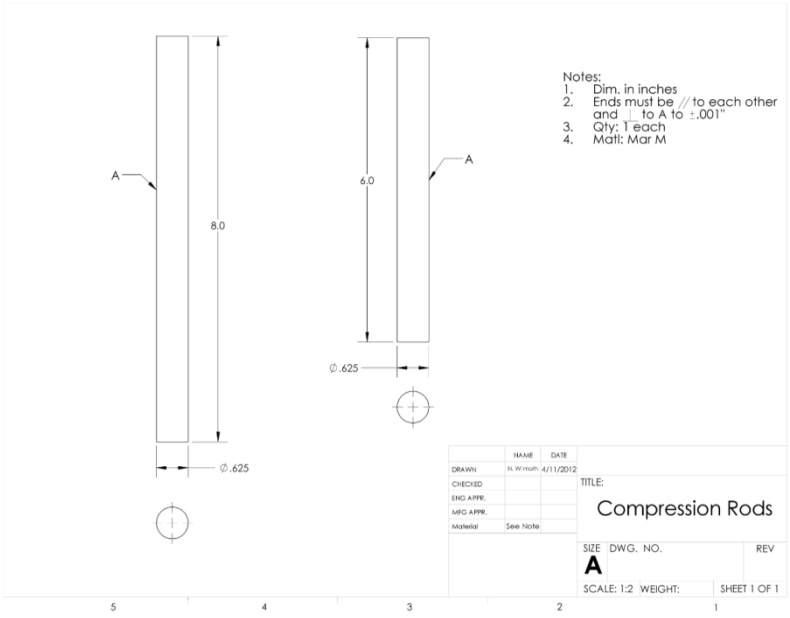

Figure B.10: Compression Rods

APPENDIX C

DEFECT MAPS

Transition 45 Incorporated, the manufacturer of the lattice block panels tested in this thesis, provided defect maps of all Ti-6-4 lattice block panels. Due to project time constraints, defect maps were not provided for the NiTi lattice block panels.

C.1 Ti-6-4 Lattice Block Panel #1 Defect Map

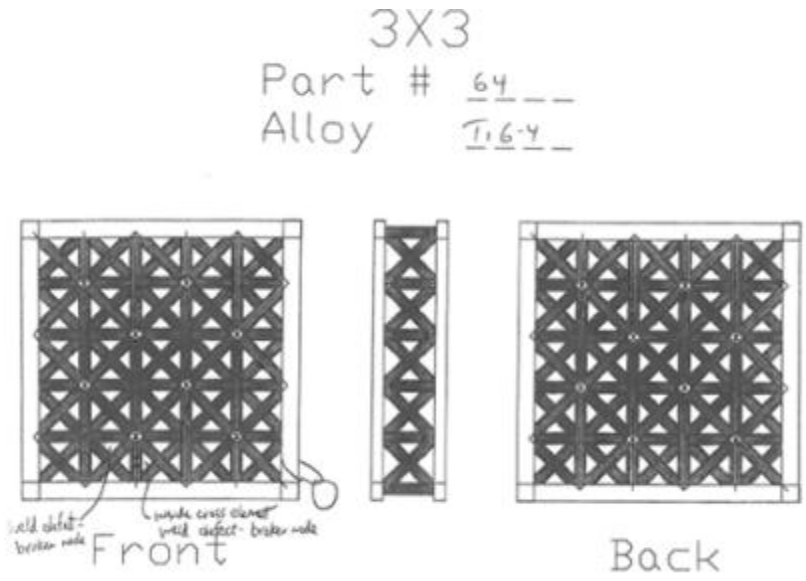

Figure C.1: Defect Map for Ti-6-4 Lattice Block Panel #1

C.2 Ti-6-4 Lattice Block Panel #2 Defect Map

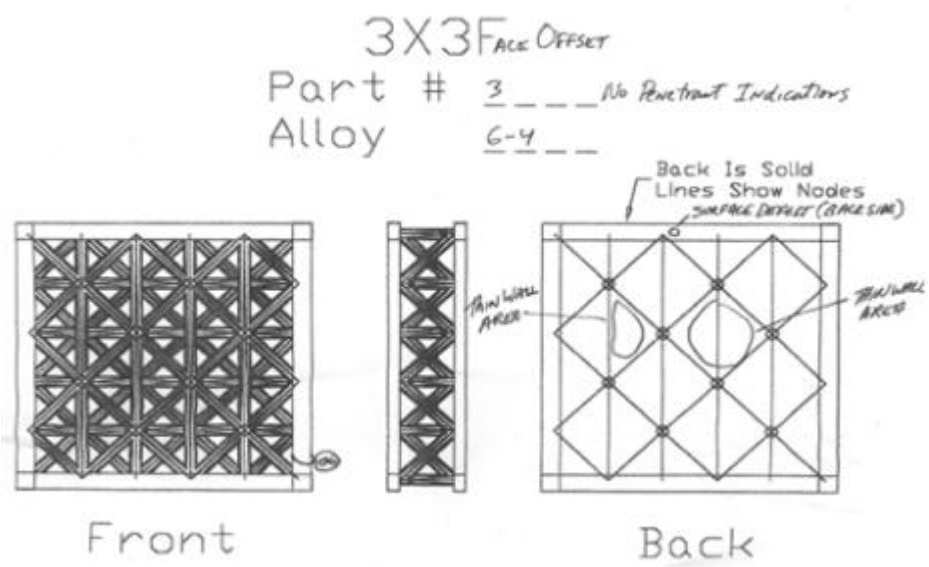

Figure C.2: Defect Map for Ti-6-4 Lattice Block Panel #2

C.3 Ti-6-4 Lattice Block Panel #3 Defect Map

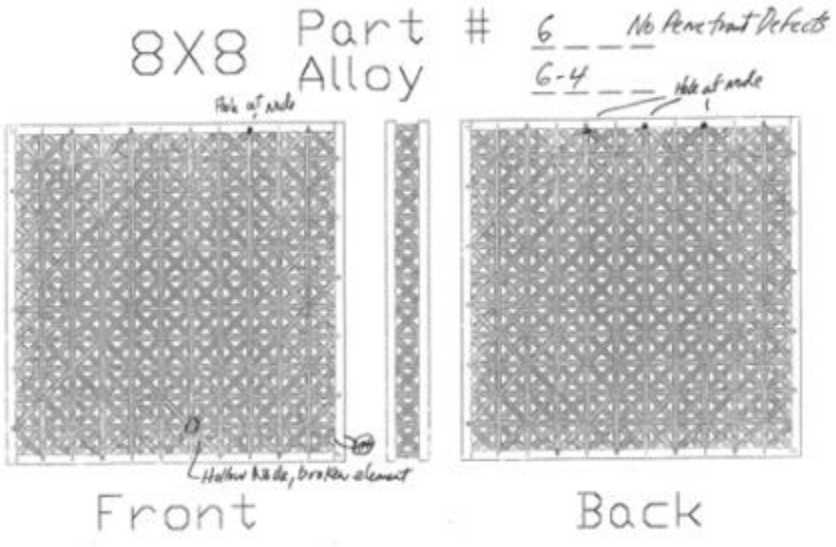

Figure C.3: Defect Map for Ti-6-4 Lattice Block Panel #3

C.4 Ti-6-4 Lattice Block Panel #4 Defect Map

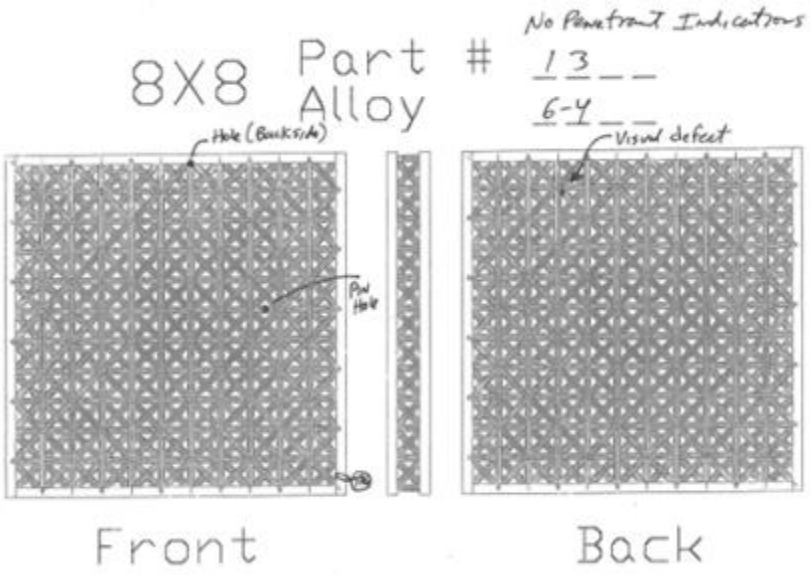

Figure C.4: Defect Map for Ti-6-4 Lattice Block Panel #4

APPENDIX D

EXTENDED DATA TABLES

This appendix provides extended data tables for all of the testing completed for this project. The term "extended" denotes that the tables provide material properties for each individual specimen tested. These tables include the average values that are consistent with the tables provided throughout this thesis.

D.1 Ti-6-4 Properties for Comparison

Table IX: Ti-6-4 Material Properties for Comparison

Estimated Properties for Cast and HIPed Ti-6-4

Room Temp							
Modulus (psi)	Modulus (GPa)	Yield Stress(psi)	Yield Stress (Mpa)	Ult Strength (psi)	Ult Strength (MPa)	% Elongation	% Area Red.
16,500,000	113.76	130,000.00	896.55	145,000.00	1,000.00	8%	16%
165C							
Modulus (psi)	Modulus (GPa)	Yield Stress (psi)	Yield Stress (Mpa)	Ult Strength (psi)	Ult Strength (MPa)	% Elongation	% Area Red.
15,548,077	107.20	101,439.39	699.58	120,000.00	827.59	10%	19.34%
200C							
Modulus (psi)	Modulus (GPa)	Yield Stress (psi)	Yield Stress (Mpa)	Ult Strength (psi)	Ult Strength (MPa)	% Elongation	% Area Red.
15,230,769	105.01	98,484.85	679.21	114,000.00	786.21	9%	20.70%

Manufacturer Provided Properties for Annealed Ti-6-4

Room Temp							
Modulus (psi)	Modulus (GPa)	Yield Stress (psi)	Yield Stress (Mpa)	Ult Strength (psi)	Ult Strength (MPa)	% Elongation	% Area Red.
15,600,000	107.56	132,000.00	910.34	145,000.00	1,000.00	18%	44%
165C							
Modulus (psi)	Modulus (GPa)	Yield Stress (psi)	Yield Stress (Mpa)	Ult Strength (psi)	Ult Strength (MPa)	%Elongation	% Area Red.
14,700,000	101.3527489	103,000.00	710.34	120,000.00	827.59	22%	53%
200C							
Modulus (psi)	Modulus (GPa)	Yield Stress (psi)	Yield Stress (Mpa)	Ult Strength (psi)	Ult Strength (MPa)	% Elongation	% Area Red.
14,400,000	99.28	100,000.00	689.66	114,000.00	786.21	20%	56%

D.2 Ti-6-4 Tension Test data

Table X: Ti-6-4 VL Test Specimen Data

Room Temp											
Run	**Panel**	**Failure**	**Modulus (psi)**	**Modulus (GPa)**	**Yield Stress (psi)**	**Yield Stress (Mpa)**	**Ult Strength (psi)**	**Ult Strength (MPa)**	**Poisson's Ratio**	**% Elongation**	**% Area Red.**
Ti_VL_RT_7T	P13	grip	16,742,652	115.44					0.356		
Ti_VL_RT_11B	P13	grip	16,944,856	116.83					0.278		
Ti_VL_RT_12B	P13	grip	16,618,300	114.58					0.263		
Ti_VL_RT_7B	P13	grip	16,588,373	114.37					0.252		
		Average	16,723,545	115.30					0.287		
		St. Dev	161,958	1.12					0.047		
		CV	0.01	0.01					0.164		
165 C											
Run	**Panel**	**Failure**	**Modulus (psi)**	**Modulus (GPa)**	**Yield Stress (psi)**	**Yield Stress (Mpa)**	**Ult Strength (psi)**	**Ult Strength (MPa)**	**Poisson's Ratio**	**% Elongation**	**% Area Red.**
Ti_VL_165_10T	P13	gage	12,992,943	89.58	88,708.53	611.78	99,408.92	685.58	0.363	2.06%	35.26%
Ti_VL_165_11T	P6	grip	17,945,189	123.73					0.213		
Ti_VL_165_12T	P6	gage	17,760,351	122.45	89,618.00	618.06	105,922.28	730.50	0.381	6.03%	39.56%
		P13 Avg	12,992,943	89.58	88,708.53	611.78	99,408.92	685.58	0.363	2.06%	35.26%
		P13 St. Dev									
		P13 CV									
		P6 Avg	17,852,770	123.09	89,618.00	618.06	105,922.28	730.50	0.297	6.03%	39.56%
		P6 St. Dev	130,700	0.90					0.119		
		P6 CV	0.01	0.01					0.400		
		Average	16,232,828	111.92	89,163.27	614.92	102,665.60	708.04	0.319	4.04%	37.41%
		St. Dev	2,807,344	19.36	643.09	4.44	4,605.64	31.76	0.092	2.81%	3.04%
		CV	0.17	0.17	0.01	0.01	0.04	0.04	0.289	69.40%	8.13%
200 C											
Run	**Panel**	**Failure**	**Modulus (psi)**	**Modulus (GPa)**	**Yield Stress (psi)**	**Yield Stress (Mpa)**	**Ult Strength (psi)**	**Ult Strength (MPa)**	**Poisson's Ratio**	**% Elongation**	**% Area Red.**
Ti_VL_200_12T	P13	gage	16,541,930	114.05	85,186.20	587.49	89,827.63	619.50	0.222	1.88%	37.52%
Ti_VL_200_10B	P13	gage	18,071,006	124.59	87,130.17	600.90	98,500.57	679.31	0.324	2.98%	26.78%
Ti_VL_200_10T	P6	grip	14,538,833	100.24					0.347		
		P13 Avg	17,306,468	119.32	86,158.18	594.19	94,164.10	649.41	0.273	2.43%	32.15%
		P13 St. Dev	1,081,220	7.45	1,374.60	9.48	6,132.69	42.29	0.072	0.78%	7.59%
		P13 CV	0.06	0.06	0.02	0.02	0.07	0.07	0.265	32.03%	23.62%
		P6 Avg	14,538,833	100.24					0.347		
		P6 St. Dev									
		P6 CV									
		Average	16,383,923	112.96	86,158.18	594.19	94,164.10	649.41	0.297	2.43%	32.15%
		St. Dev	1,771,380	12.21	1,374.60	9.48	6,132.69	42.29	0.067	0.78%	7.59%
		CV	0.11	0.11	0.02	0.02	0.07	0.07	0.224	32.03%	23.62%

Table XI: Ti-6-4 VS Test Specimen Data

Room Temp											
Run	**Panel**	**Failure**	**Modulus (psi)**	**Modulus (GPa)**	**Yield Stress (psi)**	**Yield Stress (Mpa)**	**Ult Strength (psi)**	**Ult Strength (MPa)**	**Poisson's Ratio**	**% Elongation**	**% Area Red.**
Ti_VS_RT_6B	P13	grip	21,603,489	148.95					0.374		
Ti_VS_RT_13T	P13	gage	15,035,526	103.67	100,226.83	691.22	101,693.37	701.33	0.307	0.80%	29.93%
Ti_VS_RT_1B	P13	gage	14,545,061	100.28	115,784.42	798.51	121,059.57	834.89	0.270	1.44%	16.34%
Ti_VS_RT_13B	P13	grip	14,895,057	102.70							
Ti_VS_RT_6T	P13	gage	16,647,633	114.78	118,229.68	815.38	131,697.08	908.26	0.283	7.65%	21.38%
		Average	16,545,353	114.08	111,413.64	768.37	118,150.01	814.83	0.309	3.30%	22.55%
		St. Dev	2,941,064	20.28	9,764.90	67.34	15,212.00	104.91	0.046	3.78%	6.87%
		CV	0.18	0.18	0.09	0.09	0.13	0.13	0.151	114.76%	30.46%
165 C											
Run	**Panel**	**Failure**	**Modulus (psi)**	**Modulus (GPa)**	**Yield Strength (ps**	**Yield Strength (Mp**	**Ult Strength (psi)**	**Ult Strength (MPa)**	**Poisson Ratio**	**Elongation (%**	**% Area Red.**
Ti_VS_165_1T	P6	grip	15,433,974	106.41					0.300		
Ti_VS_165_13T	P6	grip	14,543,271	100.27					0.344		
		Average	14,988,622	103.34					0.322		
		St. Dev	629,822	4.34					0.031		
		CV	0.04	0.04					0.097		
200 C											
Run	**Panel**	**Failure**	**Modulus (psi)**	**Modulus (GPa)**	**Yield Strength (ps**	**Yield Strength (Mp**	**Ult Strength (psi)**	**Ult Strength (MPa)**	**Poisson Ratio**	**:longation (%)**	**% Area Red.**
Ti_VS_200_1T	P13	gage	13,925,462	96.01	75,822.07	522.91	102,528.81	707.10	0.278	13.01%	33.27%
Ti_VS_200_6T	P6	grip	11,210,887	77.30					0.318		
Ti_VS_200_16T	P6	gage	17,944,554	123.72	84,965.53	585.97	106,441.17	734.08	0.315	11.37%	43.97%
		P13 Avg	13,925,462	96.01	75,822.07	522.91	102,528.81	707.10	0.278	13.01%	33.27%
		P13 St. Dev									
		P13 CV									
		P6 Avg	14,577,720	100.51	84,965.53	585.97	106,441.17	734.08	0.317	11.37%	43.97%
		P6 St. Dev	4,761,422	32.83					0.002		
		P6 CV	0.33	0.33					0.006		
		Average	14,360,301	99.01	80,393.80	554.44	104,484.99	720.59	0.304	12.19%	38.62%
		St. Dev	3,387,828	23.36	6,465.40	44.59	2,766.46	19.08	0.022	1.16%	7.56%
		CV	0.24	0.24	0.08	0.08	0.03	0.03	0.074	9.53%	19.58%

Table XII: Ti-6-4 TL Test Specimen Data

Room Temp

Run	Panel	Failure	Modulus (psi)	Modulus (GPa)	Yield Stress (psi)	Yield Stress (Mpa)	Ult. Strength (psi)	Ult. Strength (Mpa)	Poisson's Ratio	% Elongation	% Area Red.
Ti_TL_RT_3T	P13	gage	16,394,473	113.04	123,563.48	852.16	142,350.89	981.73	0.230	4.19%	14.62%
Ti_TL_RT_4B	P13	gage	18,230,172	125.69	127,220.29	877.38	144,763.44	998.37	0.310	6.16%	16.57%
Ti_TL_RT_15B	P13	gage	17,328,903	119.48	123,325.63	850.52	137,821.78	950.50	0.302	5.94%	23.72%
Ti_TL_RT_4T	P6	node	15,016,456	103.53					0.322		
		P13 Avg	17,317,849	119.40	124,703.13	860.02	141,645.37	976.86	0.281	5.43%	18.30%
		P13 St. Dev	917,899	6.33	2,183.16	15.06	3,524.20	24.30	0.044	1.08%	4.79%
		P13 CV	0.05	0.05	0.02	0.02	0.02	0.02	0.157	19.94%	26.18%
		P6 Avg	15,016,456	103.53					0.322		0.00%
		P6 St. Dev									
		P6 CV									
		Average	16,742,501	115.44	124,703.13	860.02	141,645.37	976.86	0.281	5.43%	18.30%
		St. Dev	1,373,243	9.47	2,183.16	15.06	3,524.20	24.30	0.044	1.08%	4.79%
		CV	0.08	0.08	0.02	0.02	0.02	0.02	0.157	19.94%	26.18%

165 C

Run	Panel	Failure	Modulus (psi)	Modulus (GPa)	Yield Stress (psi)	Yield Stress (Mpa)	Ult. Strength (psi)	Ult. Strength (Mpa)	Poisson's Ratio	% Elongation	% Area Red.
Ti_TL_165_3B	P13	gage	16,367,788	112.85	86,172.45	594.29	108,879.68	750.89	0.214	11.04%	23.40%
Ti_TL_165_4T	P13	gage	14,944,609	103.04	89,465.08	617.00	98,884.88	681.96	0.332	2.03%	7.65%
Ti_TL_165_3T	P6	gage	15,769,052	108.72	87,397.68	602.74	103,294.53	712.38	0.243	5.89%	36.00%
Ti_TL_165_9T	P6	node	13,698,139	94.45	82,570.65	569.45	105,871.72	730.15	0.316	6.33%	30.51%
		P13 Avg	15,656,199	107.95	87,818.76	605.65	103,882.28	716.43	0.273	6.54%	15.53%
		P13 St. Dev	1,006,339	6.94	2,328.24	16.06	7,067.39	48.74	0.083	6.37%	11.13%
		P13 CV	0.06	0.06	0.03	0.03	0.07	0.07	0.306	97.48%	71.72%
		P6 Avg	14,733,596	101.58	84,984.16	586.10	104,583.12	721.26	0.279	6.11%	33.25%
		P6 St. Dev	582,969	4.02	1,461.87	10.08	3,118.09	21.50	0.063	2.73%	20.04%
		P6 CV	0.04	0.04	0.02	0.02	0.03	0.03	0.227	44.70%	60.28%
		Average	15,194,897	104.76	86,401.46	595.87	104,232.70	718.85	0.276	6.32%	15.53%
		St. Dev	1,155,891	7.97	2,892.85	19.95	4,233.21	29.19	0.057	3.69%	11.13%
		CV	0.08	0.08	0.03	0.03	0.04	0.04	0.206	58.37%	71.72%

200 C

Run	Panel	Failure	Modulus (psi)	Modulus (GPa)	Yield Stress (psi)	Yield Stress (Mpa)	Ult. Strength (psi)	Ult. Strength (Mpa)	Poisson's Ratio	% Elongation	% Area Red.
Ti_TL_200_9B	P13	gage	13,195,765	90.98	78,712.34	542.84	97,585.53	673.00	0.324	4.18%	43.44%
Ti_TL_200_9T	P13	gage	15,905,050	109.66	77,953.45	537.61	97,405.17	671.76	0.338	7.84%	8.07%
Ti_TL_200_15T	P6	gage	14,805,014	102.08	83,807.08	577.98	103,804.70	715.89	0.353	9.15%	34.74%
		P13 Avg	14,550,408	100.32	78,332.90	540.23	97,495.35	672.38	0.331	6.01%	25.76%
		P13 St. Dev	1,915,754	13.21	536.62	3.70	127.54	0.88	0.010	2.59%	25.01%
		P13 CV	0.13	0.13	0.01	0.01	0.00	0.00	0.029	43.04%	97.10%
		P6 Avg	14,805,014	102.08	83,807.08	577.98	103,804.70	715.89	0.353	9.15%	34.74%
		P6 St. Dev									
		P6 CV									
		Average	14,635,276	100.91	80,157.62	552.81	99,598.47	686.89	0.338	7.06%	25.76%
		St. Dev	1,362,595	9.39	3,183.22	21.95	3,643.82	25.13	0.014	2.58%	25.01%
		CV	0.09	0.09	0.04	0.04	0.04	0.04	0.042	36.49%	97.10%

Table XIII: Ti-6-4 TS Test Specimen Data

Room Temp

Run	Panel	Failure	Modulus (psi)	Modulus (GPa)	Yield Stress (psi)	Yield Stress (Mpa)	Ult. Strength (psi)	Ult. Strength (MPa)	Poisson's Ratio	% Elongation	% Area Red.
Ti_TS_RT_2B	P13	while load									
Ti_TS_RT_5T	P13	grip	15,708,941	108.31							
Ti_TS_RT_8T	P6	gage	20,909,436	144.17	121,010.81	834.56	142,655.34	983.83	0.285	2.62%	13.68%
Ti_TS_RT_14T	P6	gage	16,527,905	113.96	126,625.08	873.28	151,343.41	1,043.75	0.371	11.43%	10.88%
Ti_TS_RT_18T	P6	gage	19,462,165	134.19	127,097.90	876.54	138,650.94	956.21	0.331	3.18%	26.92%
		P13 Avg	15,708,941	108.31							
		P13 St. Dev									
		P13 CV									
		P6 Avg	18,966,502	130.77	124,911.27	861.46	144,216.56	994.60	0.329	5.74%	17.16%
		P6 St. Dev	2,232,424	15.39	3,386.16	23.35	6,488.67	44.75	0.043	4.94%	8.56%
		P6 CV	0.12	0.12	0.03	0.03	0.04	0.04	0.131	85.93%	49.91%
		Average	18,152,112	125.15	124,911.27	861.46	144,216.56	994.60	0.329	5.74%	17.16%
		St. Dev	2,444,464	16.85	3,386.16	23.35	6,488.67	44.75	0.043	4.94%	8.56%
		CV	0.13	0.13	0.03	0.03	0.04	0.04	0.131	85.93%	49.91%

165 C

Run	Panel	Failure	Modulus (psi)	Modulus (GPa)	Yield Stress (psi)	Yield Stress (Mpa)	Ult. Strength (psi)	Ult. Strength (MPa)	Poisson's Ratio	% Elongation	% Area Red.
Ti_TS_165_14B	P13	gage	12,461,435	85.92	92,712.62	639.40	117,726.04	811.90	0.318	6.51%	29.38%
Ti_TS_165_14T	P13	gage	16,362,753	112.82	89,849.54	619.65	112,809.40	778.00	0.339	8.41%	35.50%
Ti_TS_165_5T	P6	gage	14,218,637	98.03	89,326.06	616.04	118,281.98	815.74	0.311	10.14%	21.53%
		P13 Avg	14,412,094	99.37	91,281.08	629.52	115,267.72	794.95	0.328	7.46%	32.44%
		P13 St. Dev	2,758,649	19.02	2,024.50	13.96	3,476.59	23.98	0.015	1.34%	4.33%
		P13 CV	0.19	0.19	0.02	0.02	0.03	0.03	0.045	17.97%	13.34%
		P6 Avg	14,218,637	98.03	89,326.06	616.04	118,281.98	815.74	0.311	10.14%	21.53%
		P6 St. Dev									
		P6 CV									
		Average	14,347,608	98.92	90,629.41	625.03	116,272.47	801.88	0.322	8.36%	28.81%
		St. Dev	1,953,854	13.47	1,823.00	12.57	3,011.96	20.77	0.014	1.82%	7.00%
		CV	0.14	0.14	0.02	0.02	0.03	0.03	0.044	21.73%	24.32%

200 C

Run	Panel	Failure	Yield Stress (Mp	Modulus (GPa)	Yield Strength (ps	Yield Stress (psi)	Ult. Strength (psi)	Ult. Strength (MPa)	Poisson's Ratio	% Elongation	% Area Red.
Ti_TS_200_5B	P13	gage	15,072,440	103.92	84,691.59	584.08	109,805.06	757.28	0.311	7.81%	44.74%
Ti_TS_200_8B	P13	gage	13,051,644	89.99	79,496.02	548.25	99,238.04	684.40	0.280	4.13%	40.13%
Ti_TS_200_17T	P6	gage	12,129,579	83.63	73,426.42	506.39	106,135.74	731.97	0.328	6.02%	34.75%
		P13 Avg	14,062,042	96.95	82,093.81	566.16	104,521.55	720.84	0.295	5.97%	42.43%
		P13 St. Dev	1,428,918	9.85	3,673.82	25.34	7,472.01	51.53	0.022	2.60%	3.26%
		P13 CV	0.10	0.10	0.04	0.04	0.07	0.07	0.075	43.55%	7.69%
		P6 Avg	12,129,579	83.63	73,426.42	506.39	106,135.74	731.97	0.328	6.02%	34.75%
		P6 St. Dev									
		P6 CV									
		Average	13,417,888	92.51	79,204.68	546.24	105,059.61	724.55	0.306	5.99%	39.87%
		St. Dev	1,505,227	10.38	5,638.24	38.88	5,365.08	37.00	0.024	1.84%	5.00%
		CV	0.11	0.11	0.07	0.07	0.05	0.05	0.080	30.71%	12.54%

D.3 Ti-6-4 Compression Test Data

Table XIV: Ti-6-4 Compression Test Specimen Data

Room Temp

Run	Panel	Failure	Modulus (psi)	Modulus (GPa)	Yield Stress (psi)	Yield Stress (MPa)	Poisson's Ratio
Ti_C_RT_1	SN 13	shear	16,657,771	114.85	-130,795.51	-902.04	0.330
Ti_C_RT_2	SN 13	shear	15,981,671	110.19	-121,379.52	-837.10	0.331
Ti_C_RT_3	SN 13	bend	16,684,985	115.04	-124,389.50	-857.86	0.359
Ti_C_RT_4	SN 6	bend	15,592,356	107.51	-112,502.76	-775.88	0.320
Ti_C_RT_6	SN 6	bend	16,974,493	117.03	-131,787.64	-908.88	0.307
Ti_C_RT_7	SN 6	Disp R.O.	16,767,992	115.61	-136,962.24	-944.57	0.307
Ti_C_RT_8	SN 13	shear	15,353,856	105.86	-130,514.58	-900.10	0.323
Ti_C_RT_9	SN 13	Disp R.O.	8,399,958	57.92	-119,237.14	-822.33	0.332
		P13 Avg	14,615,648	100.77	-125,263.25	-863.88	0.335
		P13 St. Dev	3,517,748	24.25	5,252.22	36.22	0.014
		P13 CV	0.24	0.24	-0.04	-0.04	0.041
		P6 Avg	16,444,947	113.38	-127,084.21	-876.44	0.311
		P6 St. Dev	745,549	5.14	12,890.24	88.90	0.008
		P6 CV	0.05	0.05	-0.10	-0.10	0.025
		Average	16,404,047	113.10	-126,109.02	-869.72	0.331
		St. Dev	606,657	4.18	7,084.04	48.86	0.018
		CV	0.04	0.04	-0.06	-0.06	0.054

165 C

Run	Panel	Failure	Modulus (psi)	Modulus (GPa)	Yield Stress (psi)	Yield Stress (MPa)	Poisson's Ratio
Ti_C_165_1	SN 13	bend	15,166,401	104.57	-102,973.01	-710.16	0.338
Ti_C_165_2	SN 13	bend	14,817,266	102.16	-90,544.31	-624.44	0.348
Ti_C_165_3	SN 13	bend	16,908,965	116.58	-103,557.58	-714.19	0.340
Ti_C_165_4	SN 6	shear	10,845,576	74.78	-91,393.12	-630.30	0.329
Ti_C_165_5	SN 6	shear	15,475,785	106.70	-99,404.44	-685.55	0.339
		P13 Avg	15,630,877	107.77	-99,024.96	-682.93	0.342
		P13 St. Dev	1,120,538	7.73	7,350.27	50.69	0.005
		P13 CV	0.07	0.07	-0.07	-0.07	0.015
		P6 Avg	13,160,680	90.74	-95,398.78	-657.92	0.334
		P6 St. Dev	3,274,053	22.57	5,664.86	39.07	0.007
		P6 CV	0.25	0.25	-0.06	-0.06	0.021
		Average	15,850,384	109.28	-97,574.49	-672.93	0.339
		St. Dev	929,718	6.41	6,243.45	43.06	0.007
		CV	0.06	0.06	-0.06	-0.06	0.020

200 C

Run	Panel	Failure	Modulus (psi)	Modulus (GPa)	Yield Stress (psi)	Yield Stress (MPa)	Poisson's Ratio
Ti_C_200_1	SN 13	bend	15,099,969	104.11	-92,004.09	-634.51	0.335
Ti_C_200_2	SN 13	bend	15,550,236	107.21	-96,302.02	-664.15	0.360
Ti_C_200_3	SN 13	bend	7,510,671	51.78	-91,197.41	-628.95	0.355
Ti_C_200_4	SN 6	bend	16,423,545	113.24	-95,626.40	-659.49	0.324
Ti_C_200_5	SN 6	bend	8,222,417	56.69	-90,376.88	-623.29	
		P13 Avg	12,720,292	87.70	-93,167.84	-642.54	0.350
		P13 St. Dev	4517277.73	31.15	2,744.09	18.92	0.013
		P13 CV	0.36	0.36	-0.03	-0.03	0.038
		P6 Avg	12,322,981	84.96	-93,001.64	-641.39	0.324
		P6 St. Dev	5,799,073	39.98	3,711.97	25.60	
		P6 CV	0.47	0.47	-0.04	-0.04	
		Average	12,561,368	86.61	-93,101.36	-642.08	0.343
		St. Dev	4,319,441	29.78	2,686.63	18.53	0.017
		CV	0.34	0.34	-0.03	-0.03	0.050

D.4 NiTi Compression Test Data

Table XV: NiTi Compression Test Specimen Data

Room Temp

Current Testing			Apparent	Apparent	Reorientation	Reorientation	Reorientation	Reorientation
Run	Failure	Poisson's Ratio	Modulus (psi)	Modulus (GPa)	Start (psi)	Start (MPa)	Finish (psi)	Finish (MPa)
NiTi_C_RT_1	bend	0.344	3,005,373	20.72	-33,731.92	-232.63	-70,595.41	-486.86
NiTi_C_RT_2	barrel	0.382	4,903,382	33.81	-35,948.32	-247.92	-67,490.28	-465.45
NiTi_C_RT_3	bend		3,003,839	20.71	-41,355.98	-285.21	-73,056.29	-503.84
NiTi_C_RT_4	barrel	0.324	4,722,603	32.56	-36,901.84	-254.50	-67,103.23	-462.78
NiTi_C_RT_5	barrel		4,707,021	32.45	-32,700.70	-225.52	-66,255.56	-456.93
	Average	0.350	4,068,444	28.05	-36,127.75	-249.16	-68,900.15	-475.17
	St. Dev	0.030	974,209	6.72	3,370.85	23.25	2,844.20	19.62
	CV	0.085	0.24	0.24	-0.09	-0.09	-0.04	-0.04

Room Temp

Previous NASA Testing		Apparent	Apparent	Reorientation	Reorientation	Reorientation	Reorientation
Run		Modulus (psi)	Modulus (GPa)	Start (psi)	Start (MPa)	Finish (psi)	Finish (MPa)
Prev_RT_1		4,604,781	31.75	-35041.18	-241.60	-58380.70	-402.52
Prev_RT_2		5,547,242	38.25	-35230.37	-242.90	-64934.42	-447.71
Prev_RT_3		5,551,175	38.27	-34375.33	-237.01		
	Average	5,234,399	36.09	-34,882.29	-240.50	-61,657.56	-425.11
	St. Dev	545,269	3.76	449.12	3.10	4,634.18	31.95
	CV	0.10	0.10	-0.01	-0.01	-0.08	-0.08

165 C

Current Testing			Apparent	Apparent	Reorientation	Reorientation
Run	Failure	Poisson's Ratio	Modulus (psi)	Modulus (GPa)	Start (psi)	Start (MPa)
NiTi_C_165_2	load smash	0.363	9,720,490	67.02	-75,203.64	-518.65
NiTi_C_165_3	barrel	0.407	3,009,201	20.75	-79,726.50	-549.84
NiTi_C_165_4	bend	0.209	5,758,340	39.70	-59,154.91	-407.96
NiTi_C_165_5	barrel	0.427	11,105,102	76.57	-60,906.04	-420.04
	Average	0.351	7,398,283	51.01	-68,747.78	-474.12
	St. Dev	0.099	3,700,748	25.52	10,258.76	70.75
	CV	0.280	0.50	0.50	-0.15	-0.15

200 C

Current Testing			Apparent	Apparent	Reorientation	Reorientation
Run	Failure	Poisson's Ratio	Modulus (psi)	Modulus (GPa)	Start (psi)	Start (MPa)
NiTi_C_200_1	barrel		6,648,247	45.84	-95,614.87	-659.41
NiTi_C_200_2	barrel		11,347,668	78.24	-73,906.46	-509.70
NiTi_C_200_3	barrel	0.285	9,125,323	62.92	-83,082.47	-572.98
NiTi_C_200_4	bend		3,646,082	25.14	-72,880.99	-502.63
NiTi_C_200_5	barrel	0.406	4,744,631	32.71	-83,453.02	-575.54
	Average	0.346	7,102,390	48.97	-81,787.56	-564.05
	St. Dev	0.086	3,155,391	21.76	9,179.92	63.31
	CV	0.248	0.44	0.44	-0.11	-0.11